

Diss. ETH No 14004

**AN INVESTIGATION OF MOLTEN MICRODROPLET
SURFACE DEPOSITION:
TRANSIENT BEHAVIOR, WETTING ANGLE DYNAMICS
AND SUBSTRATE MELTING PHENOMENON**

Dissertation

submitted to the
Swiss Federal Institute of Technology
Zurich

for the degree of
Doctor of Technical Sciences

presented by

Daniel Attinger

Ing. Mech. EPFL
Born December 11th, 1971
Citizen of Ardon VS, Switzerland

accepted on the recommendation of

Prof. Dr. Dimos Poulikakos, examiner
Prof. Dr. George Yadigaroglu, co-examiner

Zurich, 2001

Seite Leer /
Blank leaf

*Que tu la secoues, que tu l'agites,
la dernière goutte est pour le slip.*

Anonymous biologist, Swiss Federal Institute of Technology, Lausanne - 1995

Seite Leer /
Blank leaf

Acknowledgements

I would like to thank all those who have contributed to make my years at ETH Zurich such an enjoyable and exciting experience. In particular, I am very grateful to

Prof. Dr. Dimos Poulidakos, my advisor, for his friendly and very knowledgeable guidance, as well as for the great personal interaction we have had together.

Prof. Dr. George Yadigaroglu, my co-examiner, for providing me with his vast scientific expertise.

Dr. Ziqun Zhao, who taught me the trial and error process and whose wide scientific knowledge were a valuable help for realizing the experimental part of the thesis.

Dr. Yiannis Ventikos, whose tremendous curiosity led to lots of fruitful scientific and not only discussions.

Vincent Butty for his help concerning the numerical part of the thesis.

Stefan Haferl for inspiring discussions and several scientific contributions to my thesis.

My graduate colleagues, for the very good time spent together enjoying the benefits of youth and internationality, specially Christian del Taglia, Andreas Obieglo, Andrea Prospero and Steve Glod.

Martin Meuli and Max Hard, whose technical expertise and valuable suggestions have contributed to the experimental part of the thesis.

Marianne Ulrich, for her kind and friendly help with administrative tasks.

Warm thanks also go to my close friends, who have contributed, in their own way but always with love, in making my stay in Zurich a beautiful human experience. Special thanks to Agnès Jullin, Agnès Bürli and André Simon, Eric and Jennifer Weiss, Etienne and Sabine Gianadda, Christophe Michaud, Jean-Jacques Pitteloud, Raphaël von Roten and Jürgen von Sachs.

Last but by no means least, the warmest thanks go to my family members, specially to my parents who have given me, besides a unbelievable amount of love, the interest of knowing new things and the encouragement to think by myself.

Zurich, January 2001

Daniel Attinger

Seite Leer /
Blank leaf

Seite Leer /
Blank leaf

Contents

List of Figures	10
Nomenclature	14
Greek Symbols	15
Subscripts	15
Résumé.....	17
Summary	19
Chapter 1: Introduction	21
1.1. Precursor Studies of Droplet Deposition by Worthington.....	21
1.2. Industrial Applications of Molten Droplet Deposition: Microelectronics Packaging and Thermal Spray Deposition.....	24
1.3. Current Knowledge Base concerning Molten Droplet Deposition.....	28
1.3.1. Problem Definition, Relevant Parameters and Dimensionless Numbers.....	28
1.3.2. Analytical Modelings as a First Insight.....	31
1.3.3. Numerical Treatments.....	36
1.3.4. Experimental Studies	38
1.4. Structure of the Thesis	39
Chapter 2: Transient Behavior and Wetting Angle Dynamics during Molten Droplet Deposition	40
2.1. Review of the Literature	40
2.2. Experimental Setup	43
2.2.1. Molten Solder Microdroplet Deposition System.....	43
2.2.2. Visualization of Solder Droplet Deposition using Strobe Microscopy.....	45
2.2.3. Image Analysis and Discussion of the Experimental Uncertainties	47
2.3. Results.....	51
2.3.1. Experimental Conditions	51
2.3.2. Qualitative Investigation of the Spreading and Solidification Process.....	53
2.3.3. Quantitative Investigation of the Spreading and Solidification Process	56
2.3.4. Wetting Angle Dynamics	62
Chapter 3: Melting and Resolidification of a Substrate caused by Molten Microdroplet Impact	71
3.1. Review of the Literature	71
3.2. Numerical Model.....	73
3.2.1. Fluid dynamics	73
3.2.2. Heat transfer and Phase change	76
3.2.3. Contact Resistance.....	77
3.2.4. Mixing	77
3.3. Numerical Simulation Procedure.....	78
3.4. Results and Discussion.....	80

3.4.1. Baseline Case and Parametric Variations.....	80
3.4.2. Mesh Size and Time Step Independence.....	81
3.4.3. General Description of the Substrate melting Process	83
3.4.4. Quantitative Characterization of Substrate Melting.....	87
3.4.5. Considerations of the Mixing between Droplet and Substrate.....	95
3.4.6. Comparison with Experiments for Larger Droplets	97
Chapter 4: Comparison between Microdroplet Impact Experiments and Calculations	102
4.1. Review of the Literature	102
4.2. Experimental Case.....	102
4.3 Theoretical and Numerical Modeling	103
4.3. Numerical Simulation Procedure.....	104
4.4. Results and Discussion	104
4.4.1. Baseline Case and Parametric Variations.....	104
4.4.2. General Description of the Droplet Oscillation Process.....	105
4.4.3. Parametric Variations: Surface Energy and Biot number.....	107
Conclusions.....	111
References.....	113
Appendix A: Analytical Estimation of the Maximum Spreading Diameter during Impact of a Drop on a Colder Surface Including Thermocapillary and Gravitational Effects .	120
A.1. Review of the Literature	120
A.2. Analytical Model	121
A.3. Results	124
Curriculum Vitae of Daniel Attinger	127

List of Figures

Figure 1: Worthington's electrical spark generation device for visualization of droplet impact and deformation (Worthington 1877a).

Figure 2: Various forms assumed by an impinging drop as observed by Worthington (1877a, 1877b) with the aid of an electrical spark generation device: (a) Milk drop on glass plate, (b) Mercury drop impact on glass plate.

Figure 3: Temporal evolution of the weight of a cellular phone exemplifying the evolution of microelectronics packaging (Lee and Chen 1998).

Figure 4: Technological evolution in microelectronics packaging (IBM Website).

Figure 5: Droplet ejection and formation (a). Solidified droplet shapes under different operating conditions (b).

Figure 6: Metallic objects manufactured with thermal spray deposition.

Figure 7: Definition of the problem to be studied.

Figure 8: Non-intuitive Pb-Sn droplet shapes due to the coupling between fluid dynamics, heat transfer and solidification. The figure right shows a pile-up of several microdroplets impacted on top of each other, a first step towards on-demand manufacturing of conductive microstructures. Both Scanning Electron Micrographs (SEM) have been performed by Peter Wägli, Laboratory for Solid State Physics, ETH Zurich.

Figure 9: The four limits in the (Ohnesorge (here Z), Weber) plane characterizing the impact of a molten droplet. Drawn based on (Schiaffino and Sonin 1997a).

Figure 10: Maximum splat radius β_{\max} (here ξ_m) as a function of the Weber number, Reynolds number and a solidification parameter λ , dependent on the Reynolds and Prandtl number (Madejski 1976).

Figure 11: Schematic of the picoliter size solder droplet deposition apparatus.

Figure 12: Strobe Microscopy technique used for recording the solder droplet deposition process.

Figure 13: Measured points on the droplet surface. Points A and G determine the droplet wetting area diameter. D is the highest visible point of the surface, when viewing from the side, not always at the axis of symmetry. The distance from D to segment AG determines the visible droplet height H_t above the surface (identified by the segment AG). The shadow below the surface and the light spot 'inside' the droplet are optical effects. The accuracy in determining the vertical and horizontal position of A and G decreases for wetting angle values near 90° , and larger than 110° , respectively.

Figure 14: Spreading, oscillations and freezing of a solder droplet on a flat substrate. Initial conditions: $v_0 = 1.54$ m/s, $d_0 = 80$ μm , $T_{1,0} = 210^\circ\text{C}$, $T_{2,0} = 48^\circ\text{C}$.

Figure 15: Spreading, oscillations and freezing of a solder droplet on a flat substrate. Initial conditions: $v_0 = 1.49$ m/s, $d_0 = 84$ μm , $T_{1,0} = 210^\circ\text{C}$, $T_{2,0} = 135^\circ\text{C}$.

Figure 16: Time evolution of the spread factor β , with the substrate temperature $T_{2,0}$ as a parameter. The error is estimated in section 2.2.3.

Figure 17: Time evolution of the dimensionless visible droplet height over the substrate H_t , with the substrate temperature $T_{2,0}$ as a parameter. The error is estimated in section 2.2.3.

Figure 18: Final, maximum and minimum droplet dimensionless visible height H_t as a function of $T_{2,0}$. The error is estimated in section 2.2.3.

Figure 19: Solidification time t_s as a function of $T_{2,0}$. The experimental values refer to the apparent solidification time, and the order of magnitude values refer to Eqs. (20) to (23).

Figure 20: Determination of the apparent dynamic wetting angles. Angle α_L is determined by points (I,G,A), and angle α_R by (H,A,G). The measurement incertitude $\delta\alpha_R$ comes primarily from the positioning of A and H, its value is estimated $\pm 12^\circ$.

Figure 21: Evolution of the wetting angle α as a function of the spread factor β for the specified initial substrate temperatures $T_{2,0}$ and impact velocities v_0 . The angular error is estimated in Figure 20.

Figure 22: Time evolution of the spread factor β , the contact angle α , the first ripple angle γ and the first ripple nondimensional height H_{t1} in the case ($v_0=2.31\text{m/s}$, $T_{2,0}=59^\circ\text{C}$). The error is estimated in section 2.2.3 and in Figure 20.

Figure 23: Contact angle measurement with Atomic Force Microscopy. The two vertical lines determine the position of the angle measurement on the splat profile. Frames (a) and (b) show the top view of the same (previously solidified) drop before (a) and after 2 minutes heating (b) above its melting temperature (183°C).

Figure 24: Schematic of the problem of interest showing axisymmetric droplet coordinate definition and melted domain (dashed line).

Figure 25: Details of a typical mesh used. The first layer of the substrate has a dimensionless thickness of 0.01 and its conductivity can be tuned for simulating interfacial resistance to heat transfer.

Figure 26: (a) Temporal evolution of the Z-axis contact point for the baseline case, for different temporal and spatial discretizations. (b) Temporal evolution of the melted volume V_M for the baseline case, for different temporal and spatial discretizations.

Figure 27: Droplet shape and phase change location as a function of the dimensionless time for the baseline case.

Figure 28: Temporal evolution of the melted volume V_M for different values of the superheat parameter SHP, corresponding to initial substrate temperatures of 180, 181 and 182°C .

Figure 29: Time from impact to complete solidification and melted volume for different values of superheat parameter SHP in case of $\text{Bi}=0.32$.

Figure 30: Temporal evolution of the melted volume V_M for different impact velocities. The velocities ranging from 1 to 2 ms^{-1} correspond to Reynolds and Weber numbers in the interval (250.6; 501.3), respectively (1.903; 7.61).

Figure 31: Temporal evolution of the melted volume V_M for different values of the Biot number. The case with an infinite Biot number is the case without thermal contact resistance between the splat and the substrate, and the four subsequent cases correspond to interfacial heat transfer coefficient values of 10^7 , 10^6 , 10^5 and $10^4 \text{ Wm}^{-2}\text{K}^{-1}$.

Figure 32: Maximum melted volume V_M as a function of the impact velocity for five different superheat parameter SHP in case of an infinite Biot number.

Figure 33: Droplet shape and interface between the drop and substrate material as a function of the dimensionless time for the baseline case. Details (a) and (b) show the instantaneous flow pathlines corresponding to $\tau=0.4$ and 1.0.

Figure 34: Experimental cross-section of a solidified 3.5 mm steel droplet on a steel substrate (Zarzalejo, et al. 1999) compared with two numerical models, (b, conduction model of Zarzalejo et al., (1999)) and (c,d present study). The horizontal line crossing figures (a, b and c) denotes the substrate surface. The maximum substrate melting location visible as a darker line in (a) is approximated by a heat-diffusion based model (b, (Zarzalejo, et al. 1999)), with a heat conductivity artificially increased for convection, and by the numerical model developed in the present study (c,d). Oscillations of the phase change front around approximately $R=0.2$ could explain the formation of the shoulders circled in the cross-section (a), since the envelope of the instantaneous phase change fronts defines the maximum substrate melting location (c).

Figure 35: Droplet shape, instantaneous velocity distribution and flow pathlines corresponding to the simulation in Figure 34 (c,d). The dimensionless time is indicated, and the length of the horizontal arrow in the first frame corresponds to a dimensionless velocity of 1.

Figure 36: Comparison between measurement and simulations of the droplet height as a function of time, with a substrate initial temperature of 48°C .

Figure 37: Comparison between measurement and simulations of the droplet height as a function of time, for three values of the Weber number. The substrate initial temperature is 48°C .

Figure 38: Comparison between measurement and simulations of the droplet height as a function of time, for three values of the interfacial Biot number B_{iS} , characterizing the thermal exchange between the substrate and the solidifying splat above it. The substrate initial temperature is 48°C .

Figure 39. Droplet spreading on a flat and colder surface. It is assumed that the droplet is spherical before impact (0) and cylindrical at the maximum spreading extension (max).

Figure 40: A liquid drop on a solid. Surface tensions at the three-phase line and wetting angle.

Figure 41: Maximum spread factor in the Re-We plane, with (solid) and without (dotted) consideration of thermocapillary or gravity effects. Calculations are based on Eq. (65) with $\zeta=0.547$ and $\alpha_a=135^\circ$. Plots (a-c) show the effect of an increasing Marangoni number, plots (d-f) show the effect of a decreasing Froude number.

Nomenclature

a	temperature coefficient of surface tension [$\text{Jm}^{-2}\text{K}^{-1}$]
Bi	Biot number [$h_3k_L^{-1}d_0$]
Ca	Capillary number [$\mu v_c \sigma^{-1}$]
c	specific heat [$\text{J kg}^{-1} \text{K}^{-1}$]
C_i	dimensionless specific heat [$c_i \rho_i \rho_L^{-1} c_L^{-1}$]
d	diameter [m]
E	energy [J]
f	frequency [s^{-1}]
Fr	Froude number [$v_0^2 d_0^{-1} g^{-1}$]
g	gravity constant [9.81 ms^{-2}]
h_t	height [m]
h	heat transfer coefficient [$\text{Wm}^{-2}\text{K}^{-1}$]
h_3	interfacial heat transfer coefficient [$\text{Wm}^{-2}\text{K}^{-1}$]
H_t	nondimensional height [(visible height)/ d_0]
\overline{H}	dimensionless free surface curvature [Hd_0]
k	thermal conductivity [$\text{Wm}^{-1}\text{K}^{-1}$]
K_i	dimensionless thermal conductivity [$k_i k_L^{-1}$]
l_3	thickness of the interface layer [m]
L_3	dimensionless thickness of the interface layer [$l_3 d_0^{-1}$]
L	latent heat [J kg^{-1}]
M	Mach number [$v_0 c^{-1}$]
Ma	Marangoni number [$-a \Delta T v_0^{-1} \mu^{-1}$]
n	outward unit normal vector [-]
Oh	Ohnesorge number [$(We)^{1/2}/Re$]
Pr	Prandtl number [$\mu c_L k_L^{-1}$]
p	pressure [Nm^{-2}]
\overline{P}	dimensionless pressure [$p \rho_L^{-1} v_0^{-2}$]
\dot{q}	heat transfer rate [W]
r	radial coordinate [m]
R	dimensionless radial coordinate [$r d_0^{-1}$]
Re	Reynolds number [$\rho v_0 d_0 \mu^{-1}$]
S	surface [m^2]
SHP	Superheat parameter [$(T_{1,0} - T_M) (T_{1,0} - T_{2,0})^{-1}$]
Ste	Stefan number [$c_L (T_M - T_{2,0}) L^{-1}$]
t	time [s]
T	temperature [K]

u	radial velocity [m s^{-1}]
\bar{U}	dimensionless radial velocity [$u \text{ t } d_0^{-1}$]
v	axial velocity [m s^{-1}]
\bar{V}	dimensionless axial velocity [$v \text{ t } d_0^{-1}$]
V	volume [m^3]
We	Weber number [$\rho v_0^2 d_0 \sigma^{-1}$]

Greek Symbols

α	apparent wetting angle [-]
β	spread factor [dd_0^{-1}]
γ	first ripple angle [-]
δ	boundary layer thickness [m]
Δ	difference [-]
μ	dynamic viscosity [Pa s]
λ, λ'	parameters
ρ	density [kg m^{-3}]
σ	surface energy [Jm^{-2}]
ϕ	dimensionless mixing indicator [-]
Φ	dissipation function [$\text{Jm}^{-3}\text{s}^{-1}$]
Θ_i	dimensionless temperature [$(T_i - T_{2,0})(T_{1,0} - T_{2,0})^{-1}$]
$\bar{\sigma}$	dimensionless stress tensor term [-]
τ	dimensionless time [$tv_0 d_0^{-1}$]
ζ	viscous dissipation factor [-]

Subscripts

0	initial
1	droplet
2	substrate
3	interface
t1	first ripple
C	contact

damp	damping
E	effective
eq	equilibrium
L	liquid
M	melting point, melted
max	maximum
R	radial
S	surface, solid
spr	spreading
∞	final, arrested
A	advancing
G	gas
K	kinetic
P	potential
ζ	viscous

Résumé

Cette thèse examine sous divers aspects le phénomène physique complexe que représente l'impact d'une microgoutte de métal liquide sur une surface solide plus froide. Ce problème d'impact de goutte avec solidification joue un rôle important pour plusieurs nouvelles technologies, par exemple la microélectronique et la micromanufacture. L'étude de ce problème présente de nombreux défis dus à la compétition simultanée entre la dynamique des fluides, le transfert de chaleur et le changement de phase, compétition qui est étudiée ici par des méthodes expérimentales, analytiques et numériques.

L'étude expérimentale concerne les aspects instationnaires de l'impact et de la solidification d'une microgoutte, aspects examinés récemment par des études numériques. Une méthode de visualisation stroboscopique a été utilisée. Une première série d'expériences a montré l'effet de la température de la surface d'impact, le substrat, sur la déposition et la solidification de la goutte. Les oscillations de la région liquide de la goutte et la rapide avance du front de solidification à l'intérieur de la goutte ont été filmées, puis quantifiées. Des mesures instationnaires de la hauteur de la goutte au-dessus du substrat ont montré un caractère analogue à une oscillation amortie. Les résultats obtenus suggèrent que le temps de solidification dépend d'une façon non-monotone de la température initiale du substrat. La formation de vagues à la surface de la goutte solidifiée a été expliquée : ces vagues proviennent du couplage entre les oscillations de la goutte et la solidification, ainsi que le suggéraient de récentes études numériques. Une seconde série d'expériences a permis de mesurer et d'analyser l'évolution de l'angle de mouillage entre la goutte et la surface d'impact. L'influence de la vitesse d'impact et de la température du substrat sur la dynamique de l'angle de mouillage a été décrite. Deux régimes ont été identifiés, et aucune correspondance avec une corrélation utilisée habituellement pour le mouillage n'a été obtenue. Il a par contre été établi que l'évolution de l'angle de mouillage est couplée avec celle de la surface libre de la goutte.

L'étude numérique concerne la simulation d'une microgoutte de métal fondu déposée sur un substrat du même métal, plus froide, qui fond sous l'effet de la chaleur transportée par la microgoutte. Le modèle physique repose sur la formulation lagrangienne des équations de Navier-Stokes, de transfert de chaleur et de masse. Le modèle résultant de ces équations rend compte de nombreux phénomènes couplant la dynamique des fluides et le transfert de chaleur et de masse, par exemple le transfert de chaleur avec changement de phase dans un domaine se déformant rapidement. La dépendance temporelle du volume de substrat qui fond sous l'influence de la microgoutte est déterminée et discutée. L'influence des conditions initiales thermiques et hydrodynamiques sur la quantité de métal fondu est déterminée. Il a été établi que le transfert de chaleur est multidimensionnel, et que le matériel de la goutte se mélange à celui du substrat. Une correspondance intéressante entre les simulations numériques et des expériences

publiées par d'autres auteurs a été obtenue. Un mécanisme complexe a été identifié, qui montre l'influence de la dynamique des fluides et particulièrement du mouvement de la surface libre sur la fonte du substrat ainsi que sa resolidification.

Une comparaison entre les résultats expérimentaux obtenus lors de cette thèse et les résultats du modèle numérique développé ici (sans fonte du substrat) a montré une bonne correspondance. De telles comparaisons sont prometteuses, car elles permettent de quantifier des paramètres physiques comme l'énergie surfacique, ainsi que des phénomènes mésoscopiques tels que le transfert de chaleur en présence d'une interface.

Summary

This thesis investigates key aspects of the fluid dynamics, heat transfer and phase change occurring during the deposition of a molten metal droplet on a colder substrate. These aspects, important to novel technologies like microelectronics packaging and micromanufacturing, have been examined experimentally, theoretically and numerically. The experimental study in Chapter 2 focused on the complex transient aspects of the droplet impact, spreading and solidification process, which have been examined through recent numerical studies. A strobe microscopy technique was developed and used. In a first series of experiments, the value of the initial substrate temperature was varied in order to study its influence on the spreading and solidification process. The dynamic interaction between the oscillation in the liquid region and the rapid advance of the solidification front was visualized and quantified. Transient measurements of the droplet height above the substrate have shown a damped oscillation. These results suggest that the solidification time depends nonmonotonically on the substrate temperature. It was also shown that the ripples on the frozen drop surface are due to a strong coupling between solidification and flow oscillations, as suggested by recent numerical results. In a second series of experiments, the evolution of the wetting angle between the spreading drop and the substrate was recorded and analyzed. The influence of the initial impact velocity and substrate temperature on the dynamics of the measured wetting angle was described. Two regimes were identified and no quantitative agreement with the widely used Hoffman's correlation for wetting was found. It was established that the wetting angle dynamics is strongly coupled with the evolution of the droplet free surface.

Chapter 3 presents a numerical investigation of molten microdroplet impact, spreading and solidification on a colder flat substrate which can melt due to the energy input from the impacting molten material. The numerical model is based on the axisymmetric Lagrangian Finite-Element formulation of the Navier-Stokes, energy and material transport equations. The model accounts for a host of complex thermofluidic phenomena, exemplified by surface tension effects and heat transfer with phase change in a severely deforming domain. The dependence of the molten substrate volume on time was determined and discussed. The influence of the thermal and hydrodynamic initial conditions on the amount of substrate melting is discussed for a range of superheat, Biot and Reynolds numbers. Multidimensional heat transfer effects, as well as material mixing between the droplet and the substrate are found and quantified. The underlying physics is discussed. Good agreement in the main features of the maximum melting depth boundary between the present numerical results and published experiments of other investigators for larger (mm-size) droplets was obtained. A complex mechanism was identified, showing the influence of the droplet fluid dynamics, particularly the free surface motion and convection heat transfer, on the substrate melt-

ing and resolidification.

In Chapter 4, a good agreement has been obtained between experimental results obtained in Chapter 2 and results of the numerical modeling presented in Chapter 3 (without substrate melting). Such matching technique shows promise to quantify physical parameters like surface tension, and mesoscopic phenomena like heat transfer through interfaces.

Chapter 1: Introduction¹

The fundamental problem of a liquid droplet impacting on a surface appears in a plethora of phenomena in nature and technology. It offers a multiplicity of scientific challenges that cover the entire area of transport phenomena. In fluid dynamics, it is a problem involving a severely deforming free liquid surface interacting with a gaseous environment on the one hand, and with a solid surface on the other hand. Complex wetting, breakup and re-coalescence may take place. The thermodynamic and heat transfer complexities can be exemplified if one considers the case where the impacting droplet is molten and solidifies upon impact. In addition to the interplay of the three heat transfer modes and thermocapillarity, substrate melting and rapid solidification need to be considered in the molten droplet impact problem. Material transport between the molten droplet and the substrate can also occur.

1.1. Precursor Studies of Droplet Deposition by Worthington

The complexities of droplet impact physics was first shown and discussed more than one hundred years ago by Worthington (1877a, 1877b). Puzzled by the patterns of the watermarks made on smoked glass plates by the impact of droplets of water and mercury falling from various heights, he decided to visualize the instantaneous shape of an impacting droplet. Worthington built an ingenious electric circuit breaker device, as shown in Figure 1 that generates an electric spark at a preset delay after a droplet impacts on a glass surface. The electric spark was short enough to “freeze” the motion and strong enough to actually observe the shapes assumed by the droplet at different stages of the impact. Using this homemade electric spark generation device, whose principle constitutes the core of the electronic timing device and short-pulse stroboscope used in the present thesis, Worthington drew by hand the multiplicity of shapes of a droplet during its impact and spreading on a dry surface, as shown in Figure 2. The phenomena discovered by means of Worthington’s pictures include axisymmetric fluid spreading on the surface, radial wave propagation from the droplet center, thinning and breakup of the spreading droplet at its center, droplet rebound from the surface, breakup into smaller droplets that shoot away from the top of the initial droplet, and development of liquid fingers at the droplet spreading front. The role of surface conditions, especially surface wetting conditions, on the spreading and flow patterns was also noticed by Worthington. Quantitative studies of droplet impact on a surface were reported much later

¹ Some of the material of this chapter is part of a review paper in press:

Attinger, D., S. Haferl, Z. Zhao, and D. Poulikakos. 2000a. Transport Phenomena in the Impact of a Molten Droplet on a Surface: Macroscopic Phenomenology and Microscopic Considerations. Part II: Heat Transfer and Solidification. C. L. Tien (ed.), *Annual Review of Heat Transfer*, Vol. 10

(1960 until present), driven by technological needs in the areas of thermal spray deposition and solder droplet jetting for microelectronics packaging.

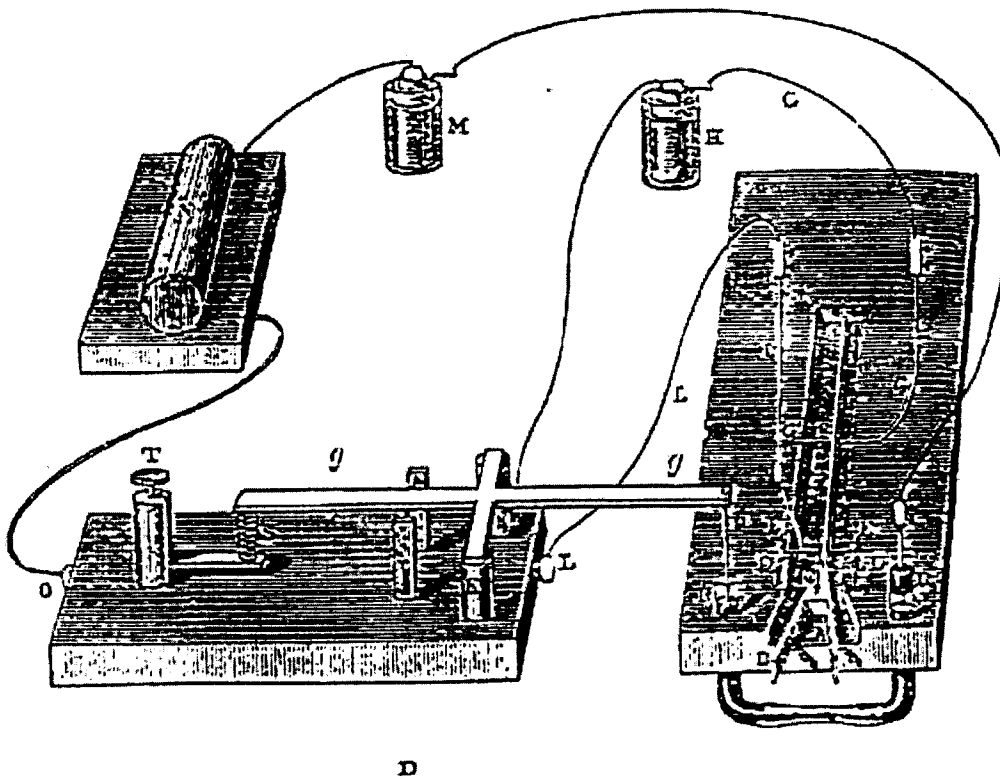


Figure 1: Worthington's electrical spark generation device for visualization of droplet impact and deformation (Worthington 1877a).

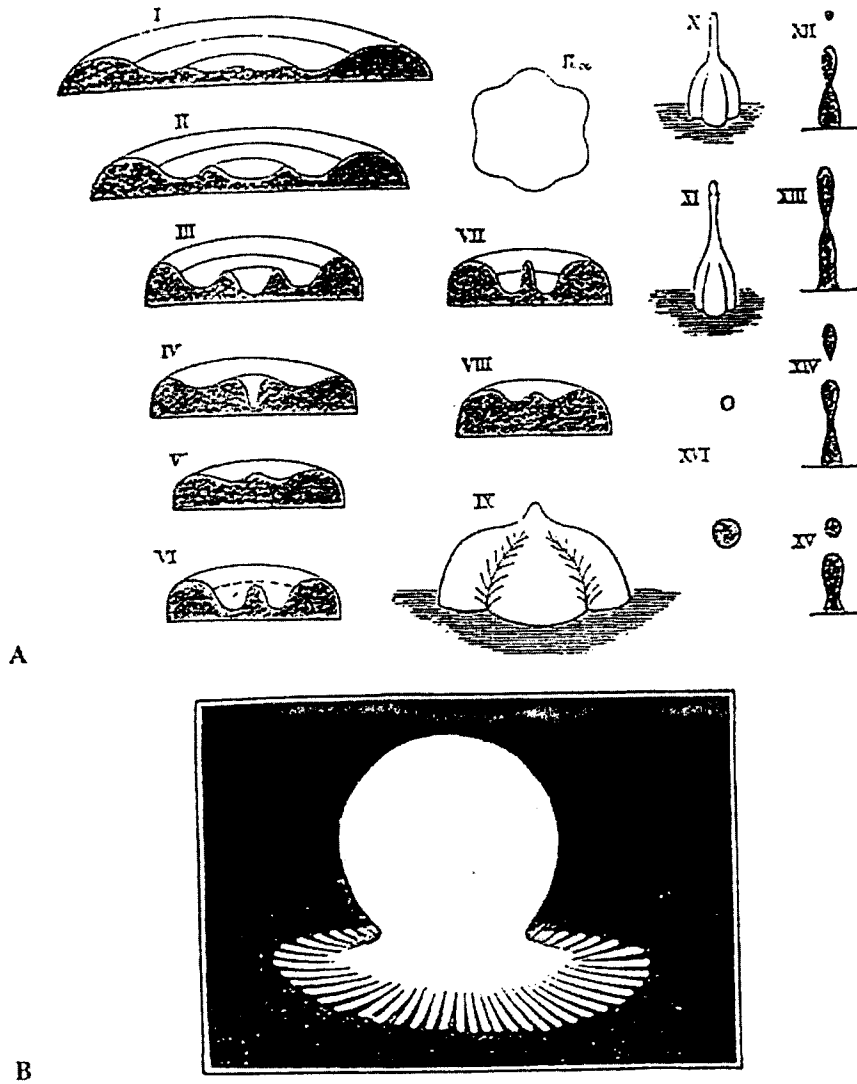


Figure 2: Various forms assumed by an impinging drop as observed by Worthington (1877a, 1877b) with the aid of an electrical spark generation device: (a) Milk drop on glass plate, (b) Mercury drop impact on glass plate.

1.2. Industrial Applications of Molten Droplet Deposition: Microelectronics Packaging and Thermal Spray Deposition

Microelectronics packaging is the technology that aims at connecting electrically microelectronic chips together or to a printed circuit board, maintaining acceptable operating temperatures and protecting the package from external damages. A drastic evolution of the size and weight of microelectronic devices occurred over the last fifteen years. Figure 3 (Lee and Chen 1998) illustrates this trend by drawing the temporal evolution of the weight of a cellular phone: from more than 800 grams in 1984, this weight has been reduced to less than 100 grams today. Considering that the functionalities of electronic devices have increased at the same pace, one can imagine how fast the packaging technologies have evolved. Figure 4 shows some steps of the evolution that occurred in packaging technologies. Basically, the package size has been reduced by replacing the standard wirebonding and pin-to-hole connections (both visible in Figure 4 (a)) with connections through an array of solder bumps featuring a smaller pitch, allowing smaller size and higher Input/Output (IO's) density. Solder droplet jetting is a versatile, fast and economic candidate for bump production (one impacted and solidified drop forms one bump), since neither masks nor screens are required (Hayes and Wallace 1998, Waldvogel, et al. 1998). Figure 5 (a) shows how a solder jetting device operates: picoliter volumes of molten metal are ejected from an orifice at demand by applying an electric pulse to a piezoelectric material not in direct contact with the fluid (like in ink-jet printing). Such a device has been set up in our laboratories at ETH Zurich. The very different shapes (Figure 5, b) of two solidified solder droplets deposited on a substrate under different initial conditions illustrate the need for a better understanding of the droplet deposition physics and for improved control of the process parameters. In high-precision applications such as microelectronics packaging, bump height deviations of a few percent can be detrimental to the successful implementation of the solder droplet jetting technique (Xiong, et al. 1998).

Another technological application of molten droplet deposition is thermal spray deposition, also named Microcasting (Zarzalejo, et al. 1999) or Solid Freeform (Orme, et al. 1996). This technology aims at manufacturing rapidly, with a high flexibility and without conventional cast, metallic objects that have near net shape, by applying precisely a controlled jet of microdrops. Some objects built with this method (Orme, et al. 1996, Zarzalejo, et al. 1999) are shown in Figure 6. The droplet sizes range from 4 μm to 100 μm . Object (a) exhibits a bimetallic Copper-Steel structure (Zarzalejo, et al. 1999) which combines high electrical conductivity and strength, while objects (b) have been shown to exhibit higher tensile strength (Orme and Smith 2000) and a lower porosity (c, right) (Orme, et al. 1996) than aluminium objects built with conventional

casting (c, left). A key parameter for the success of thermal spray deposition is the accurate control and predictive capability of the substrate remelting phenomenon: on the one hand, in case of insufficient remelting, the quality of the material can suffer from a poor adhesion between the drops; on the other hand, in case of excessive remelting, the shape of the material can be inaccurate (Figure 6, b right), because a thin liquid layer is formed and remains on top of the substrate (Orme, et al. 2000).

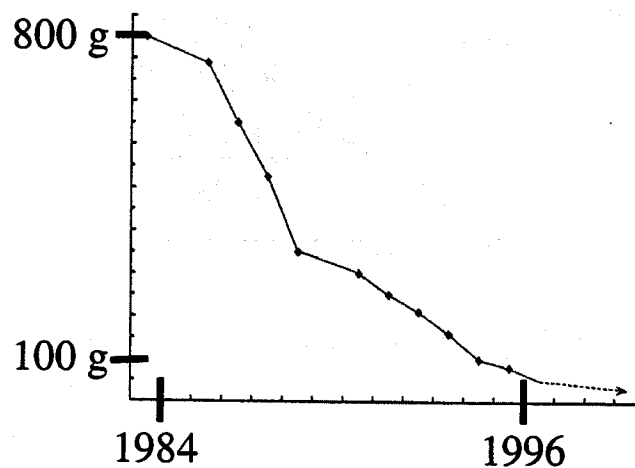


Figure 3: Temporal evolution of the weight of a cellular phone exemplifying the evolution of electronic packaging (Lee & Chen 1998).

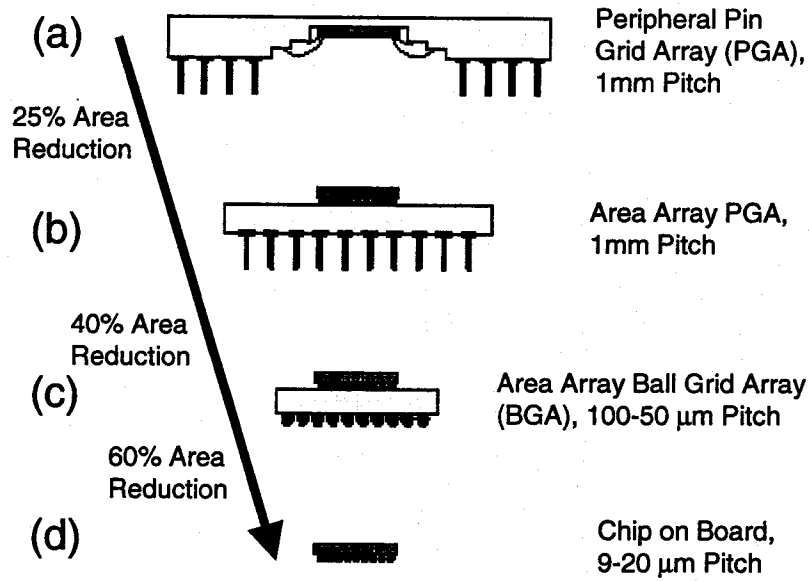


Figure 4: Technological evolution in microelectronics packaging (IBM Website).

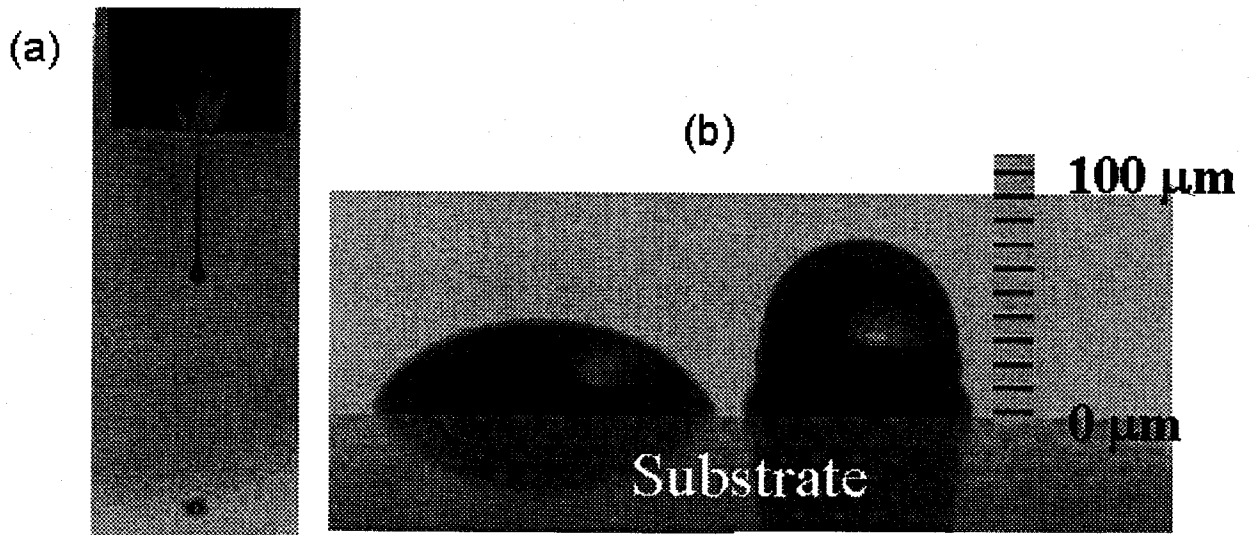


Figure 5: Droplet ejection and formation (a). Solidified droplet shapes under different operating conditions (b).

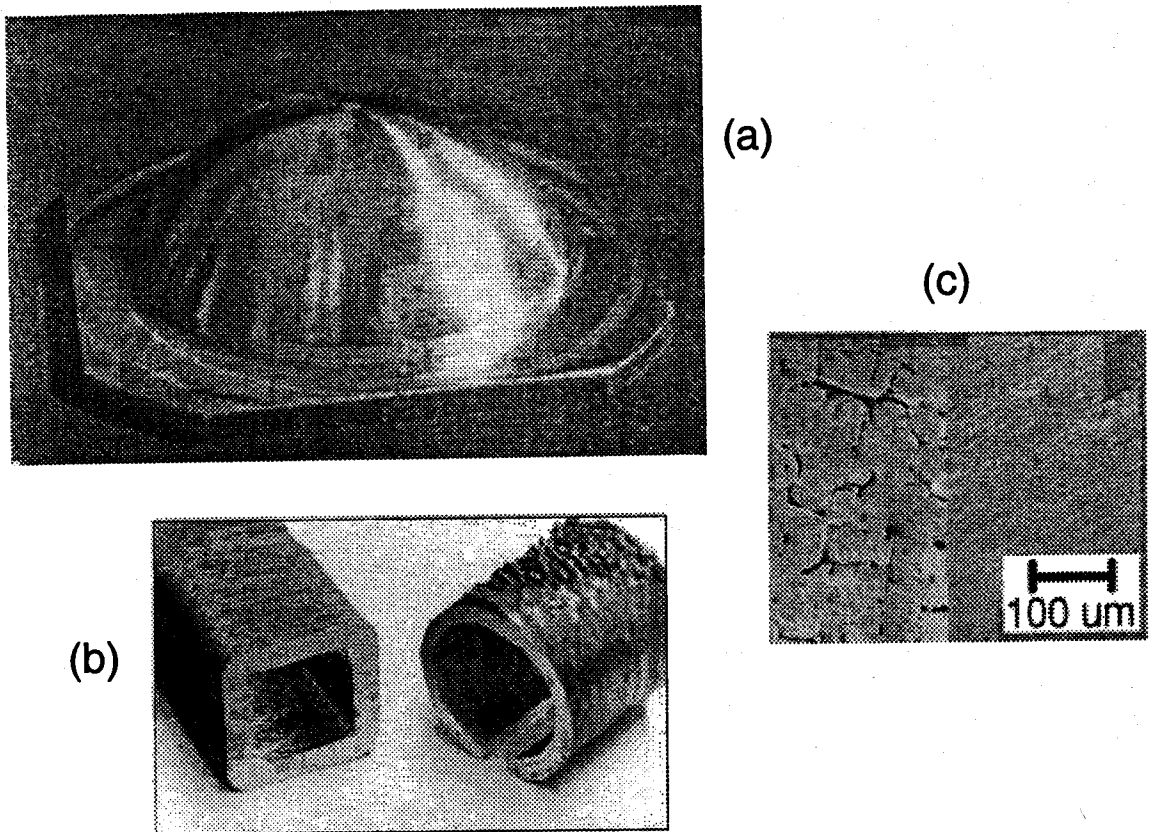


Figure 6: Metallic objects manufactured with thermal spray deposition.

1.3. Current Knowledge Base concerning Molten Droplet Deposition

1.3.1. Problem Definition, Relevant Parameters and Dimensionless Numbers

The problem definition for a molten droplet deposition case is schematically shown in Figure 7. A molten droplet originally in spherical shape moves downward in the gravitational field towards a horizontal, colder flat substrate. The thermophysical properties of the droplet, like viscosity μ , surface tension σ and density ρ , the impact conditions, including droplet velocity v_0 and diameter d_0 prior to impact and body forces such as gravity g , the substrate conditions such as temperature and wettability (including equilibrium and dynamic contact angles), all play, to various degrees, a role in defining droplet deformation and solidification after impact. After the droplet impacts the surface, it spreads out. In the meantime, heat transfer takes place, substrate melting occurs eventually and the droplet finally solidifies. The present thesis studies some key aspects of this problem, like the coupling between freezing and fluid dynamics, wetting, thermocapillary effects and substrate melting.

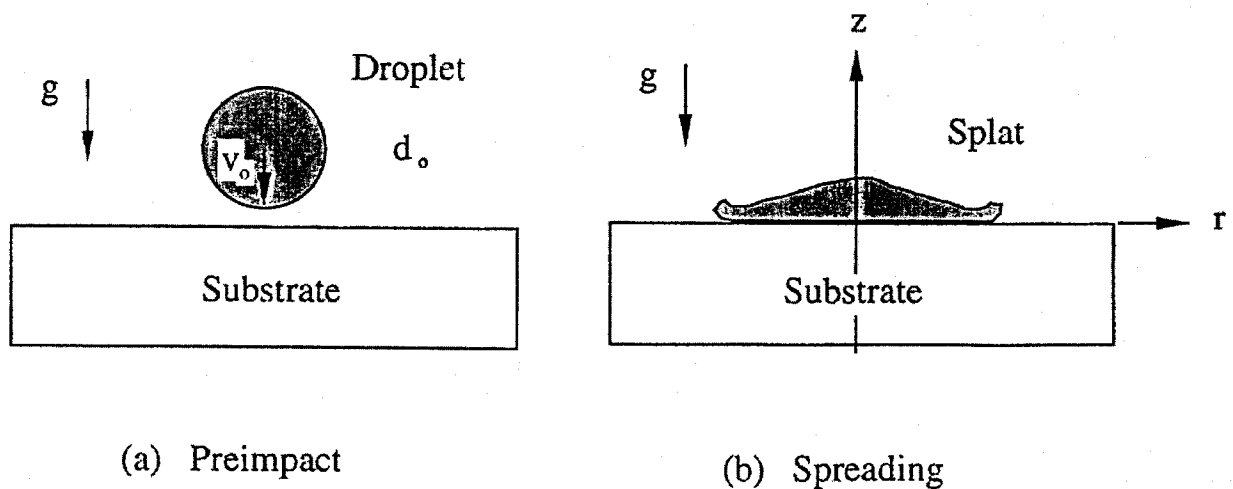


Figure 7: Definition of the problem to be studied.

In this process, it is obvious that transport phenomena like fluid dynamics, heat and mass transfer play a key role. Examples of strong coupling between fluid dynamics, heat transfer and solidification are the non-intuitive solidified shapes observed in (Waldvogel, et al. 1998) and in Figure 8. The droplet size and material in Figure 8 are relevant to the studies presented in this thesis. As a first step in these complex phenomena, scale analysis and analytical modelings provide an insight into the relative importance of the various process parameters. The relevant dimensionless parameters are:

$$\text{Reynolds number} \quad Re = \frac{\rho v_0 d_0}{\mu} \quad (1)$$

$$\text{Weber number} \quad We = \frac{\rho d_0 v_0^2}{\sigma} \quad (2)$$

$$\text{Ohnesorge number} \quad Oh = \frac{\sqrt{We}}{Re} = \frac{\mu}{\sqrt{\rho d_0 \sigma}} \quad (3)$$

$$\text{Prandtl number} \quad Pr = \frac{\mu c_L}{k_L} \quad (4)$$

$$\text{Stefan number} \quad Ste = \frac{c_L (T_M - T_{2,0})}{L} \quad (5)$$

$$\text{superheat parameter} \quad SHP = \frac{T_{1,0} - T_M}{T_M - T_{2,0}} \quad (6)$$

In the above definitions, L , c_L , k and T_M are respectively the latent heat of fusion, specific heat, thermal conductivity and equilibrium melting temperature. The indexes L , 0 and 2 stand respectively for liquid, initial and substrate. The other symbols have been defined above. The first two dimensionless groups, the Reynolds and Weber number, which measure the relative importance of inertial to viscous forces and inertial to surface tension forces, respectively, determine the fate, spreading (no drop breakup) or splashing (drop breakup), of a drop upon impact (Mundo, et al. 1995, Stow and Hadfield 1981), the rate and magnitude of spreading (Madejski 1976), as well as the subsequent oscillatory motion of the droplet fluid (Fukai, et al. 1993, Zhang and Basaran 1997). The Weber number, We , is commonly used in droplet impact studies ($v_0 > 0$). The Reynolds number, Re , is frequently used in the study of droplet impact at

high Weber numbers (Engel 1955), while the Ohnesorge number, Oh , often appears in droplet impact studies at low Weber numbers (Schiaffino and Sonin 1997c). The last three dimensionless numbers describe the heat transfer and phase change phenomena. The Prandtl number is the ratio of the momentum (fluid dynamics) and thermal diffusivities. The Stefan number (more precisely its inverse) scales the relative importance of the phase change to the heat transfer process, while the superheat parameter measures the relative importance of the droplet initial temperature difference with the equilibrium melting temperature.

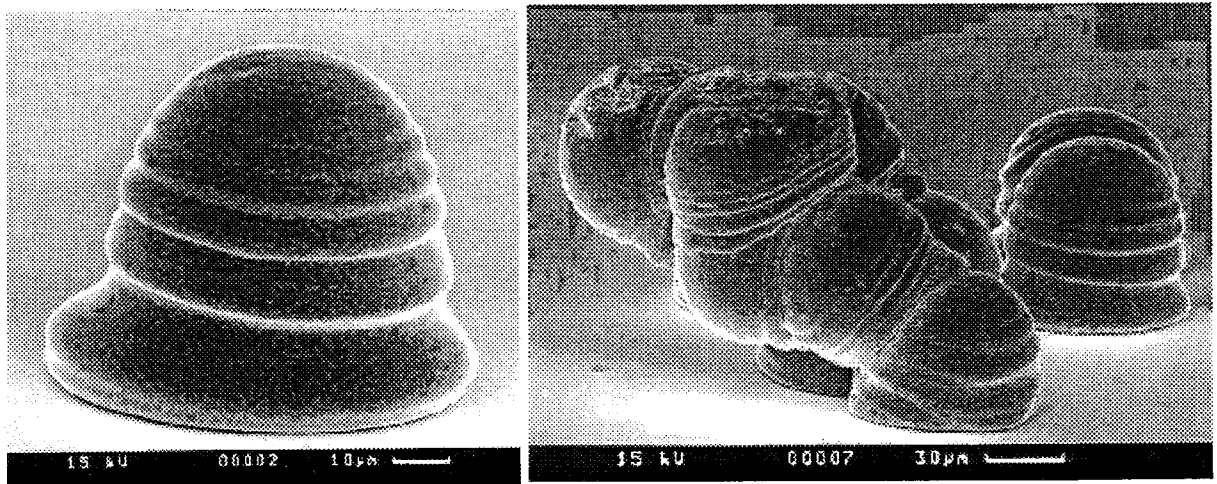


Figure 8: Non-intuitive Pb-Sn droplet shapes due to the coupling between fluid dynamics, heat transfer and solidification. The figure right shows a pile-up of several microdroplets impacted on top of each other, a first step towards on-demand manufacturing of conductive microstructures. Both Scanning Electron Micrographs (SEM) have been performed by Peter Wägli, Laboratory for Solid State Physics, ETH Zurich.

1.3.2. Analytical Modelings as a First Insight

Most of the research in the 1960's and early 1970's was focused on metallurgical aspects of the process only (Anantharaman and Suryanarayana 1971, Jones 1982, Jones 1973). In order to understandably provide mathematical tractability, it has been common to oversimplify or neglect the fluid dynamics of the process, assuming that the droplet first spreads and subsequently cools and solidifies (Jones 1971). Several attempts have been reported on estimating analytically the extension and duration of the spreading, solidification and oscillations of a quenched (i.e. impacted on a colder substrate) droplet. In the literature, criteria are given for estimating the relative importance of the viscous, capillary, inertia and solidification phenomena on the above- mentioned space and time scales. These criteria can sometimes be represented by maps, as shown in Figure 9, distinguishing the domains of influence of the physical mechanisms involved (Schiaffino and Sonin 1997a). These analyzes have often been used and validated in conjunction with experimental evaluations or numerical calculations (Madejski 1976, Pasandideh-Fard, et al. 1998, Schiaffino and Sonin 1997a). A common starting point of these analytical modelings is to balance the initial and final mechanical energies in the process, i.e. kinetic and surface energies, accounting for energy dissipated through impact and solidification. The derivation of such an analytical model is presented in Appendix A of this thesis. Some of the major analytical results available to date are summarized hereafter.

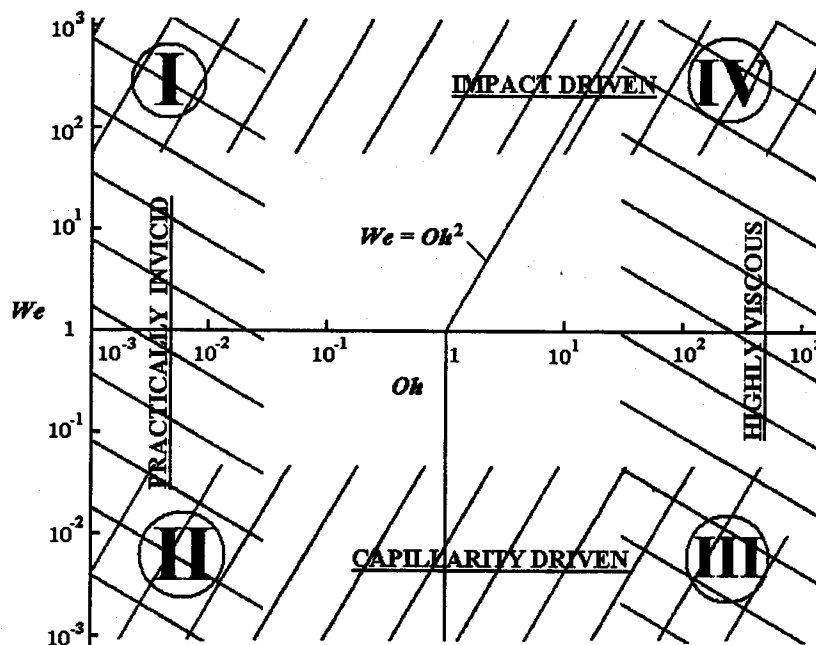


Figure 9: The four limits in the (Ohnesorge, Weber) plane characterizing the impact of a molten droplet.. Courtesy of Prof. D. Poulikakos, based on (Schiaffino and Sonin 1997a).

The spreading extension can be used as a first approximation of the solidified bump size. It can be calculated without considering the influence of solidification on the spreading (assuming that the droplet first spreads, and only subsequently cools and solidifies (Jones 1971)), or by considering a coupling between solidification and spreading. Theoretical and experimental results have shown that neglecting this coupling is justifiable for a variety of conditions (Bennett and Poulikakos 1994, Madejski 1983, Madejski 1976, Mcpherson 1980). Bennett and Poulikakos (1993) have reviewed some of the models that neglect the influence of solidification on the spreading history, and they provide the following equation for the maximum spread factor β_{\max} , defined as the ratio of the maximum diameter d_{\max} of the wetted substrate area over the initial droplet diameter d_0 :

$$\frac{\left(\frac{\beta_{\max}}{1.2941}\right)^5}{\text{Re}} + \frac{3(\beta_{\max}^2 - 4)}{\text{We}} = 1 \quad (7)$$

It should be emphasized that d_{\max} can be different from the final diameter, because the droplet can oscillate until an equilibrium diameter is arrived at. Actually, some authors do this distinction (Bennett and Poulikakos 1993, Pasandideh-Fard, et al. 1996, Schiaffino and Sonin 1997a), while others do not (Jones 1971, Madejski 1976). Bennett and Poulikakos, in their order of magnitude analysis, assume the equilibrium contact angle to be $\frac{\pi}{2}$ for simplicity. They also separate the We-Re plane in two regions, where β_{\max} can be calculated by considering individually either the viscous dissipation or the surface tension effects in Eq. (7), with less than 20% error. The boundary that separates the two regions is the line

$$\text{We} = 2.8 \text{Re}^{0.457} \quad (8)$$

The effects of a gravity and of a temperature-dependent surface tension on the maximum spread factor have been examined by Attinger et al. (1999), and their analysis, reproduced in Appendix A, yields the following equation,

$$\frac{1}{12} \left(1 + \frac{1}{Fr}\right) + \frac{1}{\text{We}} = \frac{1}{\beta_{\max}^2} \left(\frac{1}{18Fr}\right) + \beta_{\max}^2 (1 - \cos \alpha_a) \left(\frac{1}{4\text{We}} + \frac{Ma}{6\text{Re}}\right) + \beta_{\max}^2 \frac{1}{3\sqrt{\text{Re}}} \quad (9)$$

The first analytical study taking simultaneous fluid dynamics and solidification effects in metal droplet quenching into account has been reported by Madejski (1976). This analysis represents a milestone in the early efforts to study heat transfer and solidi-

fication phenomena during droplet impact on a cold substrate. Madejski's solidification model accounts for viscous energy dissipation and surface tension effects. The solidification calculation was based on a Stefan-type model, where the advance of the solidification front is unidirectional and controlled solely by conductive heat transfer, assuming both the splat and the substrate as semi-infinite bodies. Madejski also assumed that solidification starts immediately at impact, i.e. superheat effects are neglected. He postulated a dependence of the spread factor on the Weber, Reynolds as well as on the Prandtl number through a parameter $\lambda(\text{RePr})$ that quantified the freezing behavior of the droplet:

$$\beta_{\max} = f(\text{We}, \text{Re}, \lambda) \quad (10)$$

The above equation has been expressed analytically for cases without solidification, and had to be evaluated numerically for cases where spreading and solidification occurred simultaneously (Figure 10). Agreement between the theoretical predictions and experiments by Madejski was deemed adequate for high enough values of Reynolds, Weber and Peclet ($\text{Pe} = \text{RePr}$) numbers (11000-150000, 25-10000, 70-1300) (Madejski 1976).

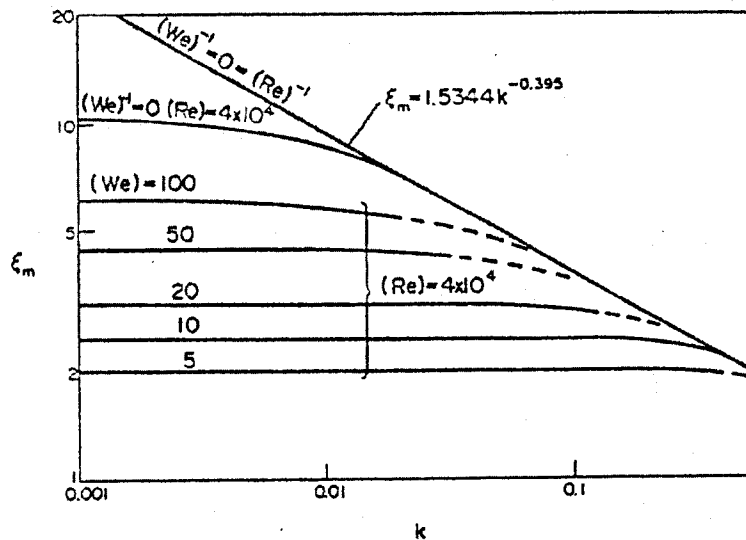


Figure 10: Maximum splat radius β_{\max} (here ξ_m) as a function of the Weber number, Reynolds number and a solidification parameter λ (here k), dependent on the Reynolds and Prandtl number (Madejski 1976).

Pasandideh-Fard et al. (1998) also presented an analytical expression for β_{\max} valid in the presence of solidification. They assumed that there is no thermal contact resistance between the splat and the substrate, that the substrate remains isothermal, and that heat transfer occurs solely through one-dimensional heat conduction. They also assumed that the onset of solidification is simultaneous with the instant of impact, that the Stefan number is low, and that the kinetic energy of the mass that solidifies gets lost. Contrary to the treatment of Madejski (1976), they assumed that the solidified part of the droplet is a disk with a diameter of $d_{\max}/2$, but they developed an analytic expression for the maximum spread factor that takes solidification into account:

$$\beta_{\max} = \frac{\sqrt{We + 12}}{\sqrt{3(1 - \cos\theta_a) + 4\left(\frac{We}{\sqrt{Re}}\right) + We\sqrt{\frac{3Ste}{4RePr}}}} \quad (11)$$

It is noted here that the assumptions made in deriving the above equation are usually not satisfied in spray deposition and micromanufacturing applications, like in the cases that will be considered in the present thesis. In these processes, it has been shown that both overheat above droplet melting temperature and the temperature of the substrate will significantly alter the solidification process of an impacting droplet (Bennett and Poulikakos 1994). Interfacial contact resistance to heat transfer between the droplet solidified layer and the substrate also has a strong influence on the advancement of solidification front in a spreading droplet (Waldvogel and Poulikakos 1997). Nevertheless, Eq. (11) provides an estimate on the limit of the influence of solidification on droplet spreading. The magnitude of the term $We\sqrt{\frac{3Ste}{4RePr}}$ in comparison with the other two terms in the denominator of the above equation determines whether solidification influences droplet spreading. Comparison with the other two terms in the denominator shows that the kinetic energy loss due to solidification will be too small to affect droplet spreading if

$$\sqrt{\frac{Ste}{Pr}} \ll 1. \quad (12)$$

Not only maximum spread diameters, but also the time scales of spreading and solidification, as well as final shape approximations, are important in droplet quenching. Assuming the final droplet shape to be a disk, Pasandideh-Fard et al. (1996) estimated the time for a liquid droplet to spread to its maximum diameter as

$$t_{\text{spr}} = \frac{8d_0}{3v_0} \quad (13)$$

Experimental results reported in (Pasandideh-Fard, et al. 1996) agreed reasonably well with the above estimate, and confirmed in the case of moderate Weber numbers (27-28), that inertial phenomena dominate the first phase of droplet spreading, and that t_{spr} does not depend significantly on the value of the equilibrium wetting angle. It should be emphasized that the uncompensated Young force at the wetting line has been neglected in the derivation of Eqs. (7) through (13), thus the above treatments do not apply to low Weber numbers.

Recently, Schiaffino and Sonin (1997a) have provided useful correlations and laws for predicting the spreading and solidification scales of a molten droplet, particularly in the previously neglected low Weber case. They proceeded in terms of both similarity laws and experimentation. From the spreading dynamics point of view, they distinguished four regions in the (Oh, We) plane, numbered from I to IV as in Figure 9. The Weber number scales the driving force for the spreading and the Ohnesorge number scales the force that resists the spreading. Due to the low viscosity of molten metals, the majority of metal droplet deposition problems lie in the low Oh domains I and II. From the expressions of characteristic spreading times given by Schiaffino and Sonin (1997a) for the four domains in Figure 9, it appears that the spreading time estimation by Pasandideh-Fard et al., Eq. (13), is only valid for domain I of Figure 9 (low Oh, high We).

The final shape of a solidified droplet depends strongly on the importance of the coupling between spreading, oscillations and solidification. The most comprehensive treatment of this issue is due to Schiaffino and Sonin (1997a). They approximated the solidification time t_s by the time to remove the latent heat during solidification, neglecting the time to remove the initial superheat (Gao and Sonin 1994). Two other important effects, which have been shown to be significant in other studies, were neglected in their theoretical formulations: convection effects within the droplet (Zhao, et al. 1996a) and thermal contact resistance at the splat-substrate interface (Bennett and Poulidakos 1994, Wang and Matthys 1991). They also assumed that the liquid, solid and substrate all share the same thermal properties. In that case,

$$t_s = \frac{\rho d_0^2}{k} \frac{L}{(T_m - T_s)} \quad (14)$$

Under these assumptions, they provided expressions for comparing the spreading time to the solidification time, valid for all the four regions of Figure 9. In most of the experiments reported by Schiaffino and Sonin (1997a), the solidification time is longer than the spreading time. This implies that most of the liquid mass solidifies after the wetting line has come to a halt. However, experiments conducted in (Schiaffino and Sonin 1997a) showed that, for low Weber numbers, solidification controls the arrest of

the wetting line. In regions II and III of Figure 9, due to the high importance of surface tension, the solidified droplet shape can be approximated by a spherical cap, as in Figure 5b, left.

This ‘spherical cap’ assumption is of course only valid if the liquid stops oscillating before solidification occurs. This is controlled by the ratio of the damping time and the solidification time:

$$\frac{t_{damp}}{t_s} = \lambda' \frac{Ste}{Pr} \quad (15)$$

where experiments determined the material-related constant $\lambda' = 0.035$ in region II. If $\frac{t_{damp}}{t_s}$ is not small, the coupling between solidification and oscillations engenders the ripples observed in some experiments ((Schiaffino and Sonin 1997a, Waldvogel and Poulikakos 1997), and Figure 8) and predicted by numerical calculations (Waldvogel and Poulikakos 1997). This criterion (15) is comparable to that of Eq. (12). In the highly viscous region III, the damping time scale is much smaller than the solidification time scale.

Clearly, however, analytical models cannot accurately predict the actual fluid dynamics (Zhang and Basaran 1997), heat transfer and solidification ((Waldvogel, et al. 1998) and Chapter 2, 3 and 4 of the present thesis) of an impacting microdroplet. Numerical models have therefore been developed, with various degrees of complexity.

1.3.3. Numerical Treatments

Numerical simulations of heat transfer and solidification, involving an array of droplets have been performed by Orme et al. (1996) for evaluating different strategies of droplet deposition in near-net-shape manufacturing. The fluid dynamics were neglected, i.e. a hemispherical ‘spherical cap’ droplet shape was assumed, and solidification was assumed to occur at the equilibrium temperature. It should be emphasized that this treatment is only valid for cases where the droplet solidifies when spreading and oscillations have come to an end, which is not really common in splat quenching. For example, in a typical application of solder jetting involving eutectic tin-lead solder droplets impinging on a substrate at 48°C (Chapter 2 and 4 of the present thesis), the criterion of Pasandideh-Fard et al. in Eq. (12), $\sqrt{\frac{Ste}{Pr}} = 5.53$, clearly implies that there is a coupling between fluid dynamics and solidification.

Rangel and Bian (1997) proposed a numerical treatment of simultaneous droplet spreading and solidification. In the liquid region, they assumed a velocity field that satisfies the continuity equation as well as the shear-free condition on the free surface of

the liquid. Using the energy equation for each phase, and an expression for the latent heat release at the solid-liquid interface, they obtained an expression for the interface propagation. They were able to study substrate remelting. But their assumption that the height of the liquid phase is constant in space, as in Madejski's treatment, is not always verified by the predictions of more sophisticated numerical models as shown in (Waldvogel and Poulikakos 1997).

Numerical treatments of droplet quenching taking complete fluid dynamics into account are presented hereafter. So far, all approaches we were able to locate in the literature postulate that phase change occurs at the equilibrium solidification temperature (a review on non-equilibrium phase change and its implications on droplet quenching can be found in (Attinger, et al. 2000a)). It has also been assumed that the phase change interface is a sharp boundary, which is appropriate for a phase change interface growing in a planar way, which is likely to occur (Attinger, et al. 2000a) due to velocities of the phase change front of the order of 1 m/s. The numerical treatment of Pasandideh-Fard et al. (1998) assumes axisymmetry, uses the Eulerian formulation of the governing equations and is based on a modified Volume of Fluid (SOLA-VOF) algorithm for fluid flow. Values of boundary conditions such as the liquid-solid contact angle and thermal contact resistance were provided, respectively estimated, by measurements. The coupling between solidification and flow was studied via a modified fixed velocity method (Salcudean and Abdullah 1988), where a liquid volume fraction function distinguishes the liquid, solid and two-phase domains. The energy equation accounts for convection and uses an enthalpy formulation for treating the phase change. In the enthalpy formulation (extensively described by Shyy et al. (1996)), the phase change region is artificially extended over a small temperature range, and the heat transfer equation is rewritten in terms of enthalpy instead of temperature. Another example of the use of the Volume of Fluid method in droplet solidification modeling can be found in Liu et al. (1993). Che et al. (February 1999) performed numerical simulations of fluid flow and phase change occurring during droplet 'pile-up', i.e. the impact of a liquid droplet on a predeposited, solidified droplet. Both the motion of the fluid within each drop and the motion of the ambient fluid are solved with a single set of equations. A front-tracking scheme and an indicator function are used for dealing with the phase boundaries between the drop and the ambient fluid, allowing the treatment of recalescence. An enthalpy formulation is used for modeling solidification. A drawback of the Volume of Fluids and front tracking numerical treatments presented above (Che, et al. February 1999, Pasandideh-Fard, et al. 1998, Liu, et al. 1993) is that their general resolution and free surface modeling capabilities are still below the requirements for the intermediate Weber number domain pertaining to solder droplet jetting.

The numerical work presented in this thesis is the continuation of a more accurate (at least in terms of free surface modeling and numerical accuracy) investigation of

key transport phenomena during the impingement of molten metal on a flat substrate, investigation whose milestones are found in (Fukai, et al. 1995, Fukai, et al. 1993, Waldvogel and Poulidakos 1997, Xiong, et al. 1998, Zhao, et al. 1996a).

1.3.4. Experimental Studies

Experimental investigations involving millimeter- and in particular micrometer-size droplets are quite challenging, due to the very fast fluid flow and thermal transients as well as the small length scales involved (Chandra and Avedisian 1991, Mundo, et al. 1995, Pasandideh-Fard, et al. 1998, Wang and Matthys 1996, Yarin and Weiss 1995). Therefore, most of the transient measurements have been carried out with millimeter-size droplets. Some of the major experimental achievements of Worthington's successors are presented hereafter.

Gao and Sonin (1994) presented a study of the precise deposition and solidification of molten wax microdrops for the following scenarios: single droplets, low and high frequency deposition of multiple droplets to produce columns, sweep deposition of continuous beads, and repeated sweep deposition for the buildup of layered objects.

Pasandideh-Fard et al. (1998) deposited millimeter-size tin droplets on a flat polished steel plate. The Weber and Reynolds numbers were respectively 71 and 12000. The Stefan number was varied in order to study both cases where solidification influences the spreading and where it does not, according to Eq. (12) In the case where solidification influenced the spreading, their experimental spread factor β_{\max} was found to be significantly larger than the value predicted by their analytical treatment, as in Eq. (11). The authors attributed this finding to their neglecting the effect of thermal contact resistance. Accordingly, a better agreement between analytical and experimental results, with less than 5 % discrepancy, was obtained by considering in the analysis the influence of the thermal contact resistance on the solid layer growth.

Besides shape measurements, such as spread factors and contact angles, several temperature measurements have been performed and matched with numerical simulations in order to estimate the values of the thermal contact resistance between the splat and the substrate (Bennett and Poulidakos 1994, Pasandideh-Fard, et al. 1998, Wang and Matthys 1996). The understanding of the physics pertaining to thermal contact resistance is a critical issue in predicting final shapes of solidified droplets, as will be shown in Chapter 4 of the present thesis.

1.4. Structure of the Thesis

The present work includes experimental investigations as well as theoretical modelings. On the experimental front, we investigated with strobe microscopy the spreading of a microdroplet on a flat substrate (Chapter 2), focusing on the coupling between fluid dynamics, heat transfer and solidification, and accounting for the wetting phenomenon. A theoretical and numerical modeling (Chapter 3) investigates the melting of a substrate caused by a molten droplet impact. The effects of various process parameters on the substrate melting are discussed. Two comparisons (end of Chapter 3, Chapter 4) have been performed between numerical and experimental results, respectively with and without substrate melting. These comparisons show a good agreement between experiments and modeling; the related findings are discussed. An analytical model has been derived (Appendix A), which is focused on the influence of the temperature dependence of the surface energy on the spreading.

Chapter 2: Transient Behavior and Wetting Angle Dynamics during Molten Droplet Deposition²

2.1. Review of the Literature

Scientific research interest on droplet-surface interactions has recently increased driven by a need for an in-depth understanding of new aspects of droplet impact phenomena that are important to emerging technologies such as spray deposition (Orme 1993, Orme, et al. 1996) and picoliter size solder droplet dispensing. Picoliter size droplet dispensing (the application to which the present work is directly relevant) is used for advanced surface mount technologies in the packaging of electronic microchips. In this technology, monodispersed arrays of molten metal microdroplets (25-100 μm in diameters) are printed on a substrate, each microdroplet (or bump) forming an electrical connection. Important advantages of picoliter size droplet dispensing over other bumping technologies are the flexibility and low cost, because neither masks nor screens are required (Hayes and Wallace 1998, Waldvogel, et al. 1998).

Many physical phenomena related to the prediction of bump shape and metallic properties are not well understood. There is still a lack of basic understanding and modeling capabilities for phenomena such as the dynamic behavior of the wetting angle between the substrate and the droplet (Haferl, et al. 2000), the thermal contact resistance between splat and substrate as well as the rapid solidification phenomenon (Attinger, et al. 2000a), including heterogeneous nucleation and recalescence, as well as the possible remelting of the substrate (Amon, et al. 1996). These are typical mesoscopic phenomena, whose physics is often related to nanoscale phenomena and cannot be fully understood using the classical continuum approach. A common way to handle these mesoscopic phenomena is to match experiments with numerical or analytical models, in order to estimate the needed model parameters. Using this approach, several temperature measurements under relatively large (mm-size) solidifying droplets have been performed and matched with numerical simulations in order to estimate the values of the thermal contact resistance between the splat and the substrate (Bennett

² Most of the material of this chapter has been published as:

Attinger, D., Z. Zhao, and D. Poulikakos. 2000. An Experimental Study of Molten Microdroplet Surface Deposition And Solidification: Transient Behavior and Wetting Angle Dynamics. *Journal of Heat Transfer* **122**(3):544-556, and presented at two conferences: **Attinger, D., Z. Zhao, and D. Poulikakos.** 1999. Visualization and Measurements of Picoliter-Size Molten Droplet Impact Dynamics and Solidification on a Surface, p. 159-169, International Mechanical Engineering Congress and Exposition, Winter Annual Meeting of ASME, vol. HTD 364-3, Nashville, Tennessee, and **Attinger, D., Z. Zhao, and D. Poulikakos.** 2000. On Factors Influencing the Wetting Angle Behavior After a Molten Microdroplet Impacts a Surface, p. 235-243, Eighth International Conference on Liquid Atomization and Spray Systems, Pasadena, CA, USA, July 2000.

and Poulikakos 1994, Pasandideh-Fard, et al. 1998, Wang and Matthys 1996), or to estimate the nucleation temperature (Bennett and Poulikakos 1994).

The evolution of the wetting angle during droplet spreading contains largely unresolved physics. The wetting angle behavior at the molecular level is governed by intermolecular forces (Blake and Haynes 1969). The relation, if any, between the molecular angle and the macroscopic angle (visible with a low power microscope, and measured in the present study) is also not well established (Dussan 1979). Empirical correlations such as Hoffman's law (Hoffmann 1975) express the dynamic evolution of the macroscopic wetting angle α as a function of the Capillary number Ca at the wetting line and of the equilibrium wetting angle α_{eq} , for steady flows under conditions of negligible Weber number (Dussan 1979). In the impact of a droplet on a flat surface, the fluid dynamics is unsteady and the Weber number based on the contact line velocity not negligible. Therefore the motion of the droplet free surface near the contact line and the dynamics of the bulk fluid may influence the value of the wetting angle. Furthermore, in a molten droplet impact, there is the additional contribution of heat transfer, which can drastically change flow properties by glassification, or can even arrest the motion of the contact line by solidification. Fukai et al. (1995) and Pasandideh-Fard et al. (1998) used experimentally measured advancing and receding wetting angles in their numerical models to study the effects of surface wetting on the spreading and recoiling motion of a droplet after impingement on a dry surface. However, since these angles and substrate temperatures have been measured for rather larger systems, with respect to both time and space scales, the question arises if the conclusions can be applied to smaller scales of the kind found in picoliter size solder droplet dispensing and spray casting.

A promising approach to obtain direct insight in the thermophysics of picoliter-size molten droplet impact is the high-speed visualization of such a process. If it were possible to observe with enough time and space resolution the spreading and solidification dynamics of picoliter solder droplet impact, in addition to the direct information that the experiments would provide, a comparison with numerical studies of the same problem such as those by Waldvogel and Poulikakos (1997) and by Xiong et al. (1998) would be feasible. Such experiments are reported in the present chapter, and a comparison between experiments and numerical simulations is reported in Chapter 4. A key finding of the above two papers is that a strong coupling occurs between heat transfer, fluid dynamics and phase change, leading to a wavy surface of the solder bumps. Although this wavy surface appears in both numerical and experimental studies (the latter yielding only the shape of the completely solidified microbump), there is still a significant discrepancy between numerical results and final shape micrographs (Xiong, et al. 1998). A visualization of the microdroplet in motion accompanied by relevant quantitative measurements contributes significantly to the understanding of this phenomenon.

A variety of visualization techniques have been applied in the experimental investigations of droplet impact dynamics, including high-speed camera techniques (Inada, et al. 1983, Pederson 1970, Savic and Boulton 1955, Toda 1974, Ueda, et al. 1979), strobe photography (Chandra and Avedisian 1991, Stow and Hadfield 1981, Wachters and Westerling 1966), and strobe videography (Mundo, et al. 1995, Yarin and Weiss 1995). There is one basic distinction between high-speed camera and flash techniques: the former records the highest number of frames from a single event, while the latter reconstructs the event by patching together several frames taken at different instants from several reproducible events. In our case, the expected short duration of the phenomenon (of the order of 100 microseconds) prevented the use of most high-speed cameras. For example, even a very fast CCD camera such as the Kodak EKTAPRO (40'500 partial frames per second and available in our laboratory) could only give a rough qualitative recording of the phenomenon. Intensified CCD cameras have a time delay between two frames smaller than 50 ns and could have solved the time resolution problem. However, this expensive technology only allows recording a limited number of frames (8 to 30) of a single event (Ohl, et al. 1995), so that the reconstruction problematic of one event from several reproducible events would have arisen in this case as well. The high speed 16 mm camera technique has not been considered, because of its complex machinery, high costs and difficulty of implementation (Levin and Hobbs 1971).

In contrast with the methods discussed above, the strobe photography and strobe videography techniques are methods whereby a variable number of short pulse illuminations (1 to 10 pulses) are produced at specific instants during each event, and recorded by a 35 mm camera or a CCD camera, respectively. By generating a sequence of identical drops and practically identical impact events per drop, one can capture different stages of the process in each event and piece together from images of droplets taken at progressive stages the entire impact, spreading and solidification process. Key parameters describing the droplet spreading process, i.e. splat/substrate contact area, splat diameter and thickness as well as the wetting angle (Pasandideh-Fard, et al. 1998) can be subsequently measured from the recorded pictures of spreading droplets. The strobe techniques rely therefore on the generation of droplets in a highly repeatable manner (Chandra and Avedisian 1991, Mundo, et al. 1995, Wachters and Westerling 1966, Yarin and Weiss 1995) since the impact process is reconstructed from images of several impact events.

Good quality images of a droplet spreading process have been reported in the literature using short-duration strobe photography (Chandra and Avedisian 1991, Pasandideh-Fard, et al. 1998) for millimeter-size droplets, and strobe videography (Yarin and Weiss 1995) for droplet diameters of the order of 60 μm to about 1 mm. To exemplify, the study of Pasandideh-Fard et al. (1998) reports a visualization of impact

and solidification of relatively large (approx. 2 mm) liquid metal tin drops on a cold substrate. Hence, the resulting Weber number value of $We=71$ does not correspond to the relatively low Weber domain ($4 < We < 10$) encountered in picoliter size solder droplet dispensing that is the focus of the present research. In the present study a strobe videography technique, called strobe microscopy because of its microscopic object, coupled with a digital grabbing of the images for the ease of postprocessing is developed and implemented.

2.2. Experimental Setup

2.2.1. Molten Solder Microdroplet Deposition System

To investigate the dynamic process of impact and solidification of picoliter size molten metal droplet on the surface of a semiconductor device, a molten solder microdroplet jetting device was set up at ETH Zurich with technical assistance from MicroFab Technologies Inc. (Dallas, Texas). The method used for the generation of monodispersed picoliter-size droplets of solder at demand with the potential of use in the manufacturing of electronic components was described in (Hayes and Wallace 1998, Hayes, et al. 1992), and is summarized as follows. By applying an electric pulse to a piezoelectric material not in direct contact with the fluid, picoliter volumes of molten metal are ejected from an orifice at demand in accordance with the electric pulse frequency. After oscillating, the ejected tiny amount of metal assumes a spherical shape due to minimization of surface tension energy. The process is termed solder jetting at demand. The jetting apparatus used in the present study is shown schematically in Figure 11. Solder is melted in an enclosed reservoir by resistance heating. The molten solder reservoir is pressurized with Nitrogen to insulate the melt with a chemically inert environment and provide back pressure for jetting. A Nitrogen flowing as a curtain around the path of the droplet toward the substrate limits the interaction with the surrounding air and prevents, at least to a good extent, droplet oxidation. Molten solder temperatures in the reservoir and the capillary tube are both monitored by thermocouples and controlled through the heaters. The waveform of the drive pulse for solder jetting is electronically generated and digitally controlled. By varying the waveform, the diameter and the velocity of ejected solder droplets can be altered in the ranges of 50-100 μm and 1-2.5 m/s, respectively. The alloy used in this study is a eutectic tin lead solder (63% Sn-37% Pb) with 99.99% purity, specially developed for solder jetting by Witmetaal B.V., Holland. Delay time between droplet ejection can be changed by varying the waveform driver frequency for droplet generation. However, the repeatability of droplet diameter and ejection velocity is greatly improved when the frequency of droplet ejection is maintained constant during experiment. In the present study, a droplet generation frequency of 12 Hz was used.

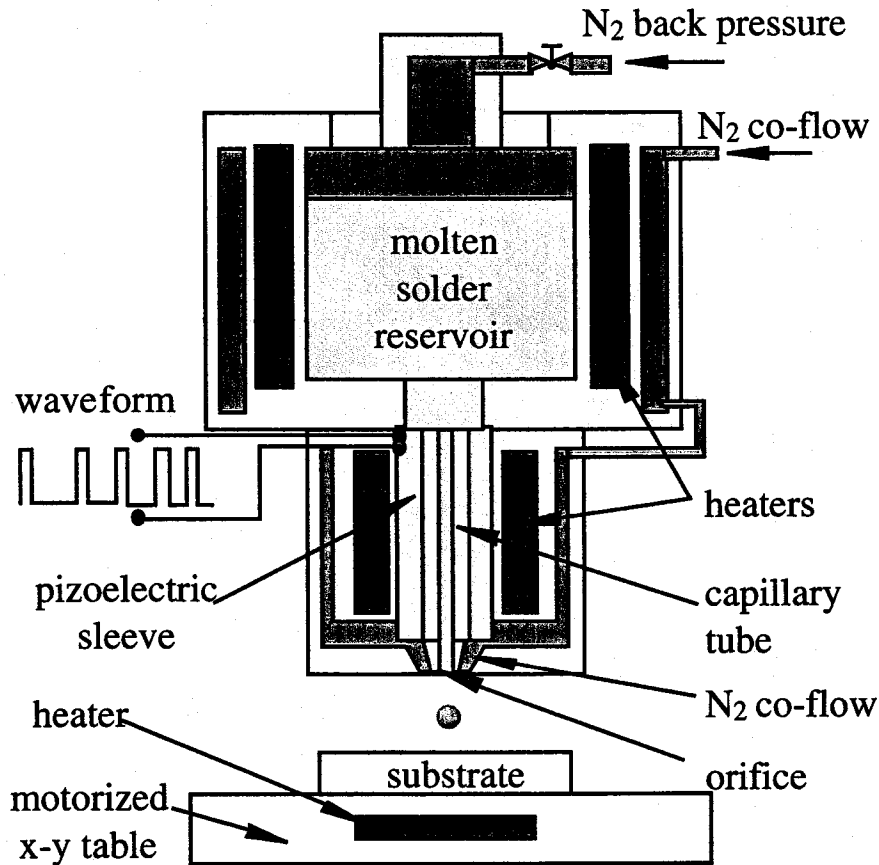


Figure 11: Schematic of the picoliter size solder droplet deposition apparatus.

After ejection from the orifice, a solder droplet travels approximately 1 mm and impacts the substrate mounted horizontally on a motorized x-y precision stage (Photon Control PTS 1000, England). The substrate in the present study is a semiconductor wafer (EM Marin, Switzerland) cut to a die size of approximately 10x50mm. The wafer consists of the following layers from top to bottom: 0.1 μm thick Au, 0.3 μm Ti90W alloy, 1 μm Silicon Nitride (conductivity $k=2.33(+0.11) \text{ Wm}^{-1}\text{K}^{-1}$, heat capacity $\rho c=2.62(+0.22)*10^{-6} \text{ Jm}^{-3}\text{K}^{-1}$)(Arx 1998), and 675 μm P-Silicon. The substrate wafer slide is mounted on a heated copper plate with a thin layer of thermal interface paste (HTC Electrolube, England) between the wafer and the copper plate, with $k=0.84 \text{ Wm}^{-1}\text{K}^{-1}$. The wafer top ($T_{2,0}$) and bottom surface initial temperatures are measured with two K-type thermocouples (Omega 304 SS9), the former being epoxied on the wafer with a 1mm-size island of conductive Epoxy (AV138M/HV998 Novartis, Switzerland) with $k=0.6 \text{ Wm}^{-1}\text{K}^{-1}$. The bead diameter of the thermocouples is 250 μm . The copper plate

temperature was controlled with a Proportional-Integral-Derivative (PID) regulator to vary $T_{2,0}$ between 48°C and 145 °C. Since the wafer slides used for printing have to be frequently replaced, the temperature measurements are carried out on another wafer slide, permanently deposited on the copper plate, and moved under the printhead at the same conditions as the wafer slide where droplets impact. Both radiation from the metallic parts of the printing device and convection from the co-flow increased significantly the wafer temperatures. The x-y stage motion (2mm/s) is so slow that the thermocouples reach a steady state value before passing under the jet orifice and maintain it after passing by the jet orifice. Therefore the transient temperature effect is considered to be negligible.

2.2.2. Visualization of Solder Droplet Deposition using Strobe Microscopy

As described in the introduction, the technique used for the visualization of droplet impact and solidification is a strobe microscopy technique (Yarin and Weiss 1995) where only one image is taken at one instant during the impact and solidification process for each drop studied. The imaging system used to record the droplet deposition process is shown schematically in Figure 12.

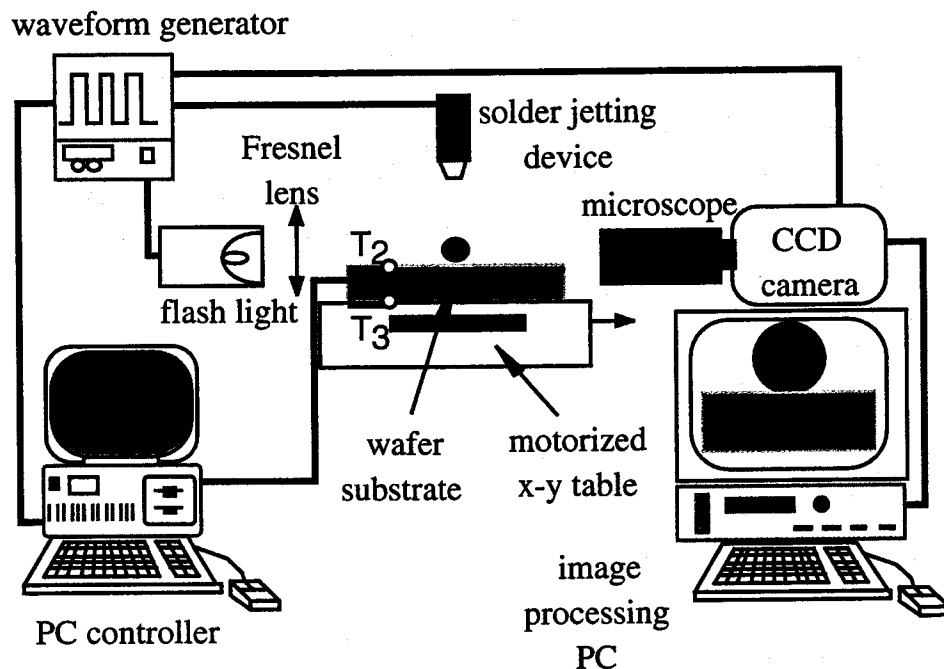


Figure 12: Strobe Microscopy technique used for recording the solder droplet deposition process.

Backlighting for the first series of experiments is provided by a Xenon flash light unit (Hamamatsu L4634). The flash energy is 0.15 J/burst and the duration of each burst of flash is 1 μ s with less than 200 ns jittering. The time resolution of the sequence recording is set to 5 μ s. A Fresnel lens is used to provide uniform and intensified (focused) backlighting field for the microscope. The droplet images are magnified using a microscope objective (Microtech Zoom 70, USA) with 29x optical magnification on the CCD matrix plane, which provides a space resolution of 1.2 μ m in the object plane. The conditions for the wetting angle measurement are slightly different from the first experiments in this chapter. The optical magnification is increased up to 36 times. In order to capture the fast kinematics during the beginning of the spreading (with contact line velocities of the order of 2 to 4 m/s), a faster Xenon flash light unit (FX-HSPS, Wedel, Germany) is employed. It provides a shorter flash duration of 150 ns with less than 60 ns jittering, with a flash energy of 0.1 J/burst. The time resolution of the sequence recording is also increased up to 300 nanoseconds during the first stage of the spreading.

Images of the droplets are acquired with a Jai M10 progressive scan CCD camera (Denmark) in triggered mode and are digitized and stored in the image processing PC. An example of the picture quality of a droplet in motion is given in Figure 13 (b). As a result of high power of optical magnification, the ambient light introduces little optical noise on droplet images, and the flashlight acts therefore as a shutter. The waveform generator that activates the solder jetting device sends a signal with a preset delay to trigger the flashlight when a solder droplet hits the substrate. To record the progressive stages of solder droplet spreading and solidification, the delay time between droplet ejection and a burst of back lighting is increased between successive images.

In order to provide a free impact surface for each impinging droplet, the motorized x-y stage is maintained at a constant linear speed of 2 mm/s in the focal plane of the microscope during experimental runs. This translation velocity of 2 mm/s is about three orders of magnitude smaller than the impact velocity of 1.5 m/s. In a reference frame attached to the translation stage, this motion corresponds to a deviation from the vertical direction of the impact smaller than 0.1 degrees, thus negligible.

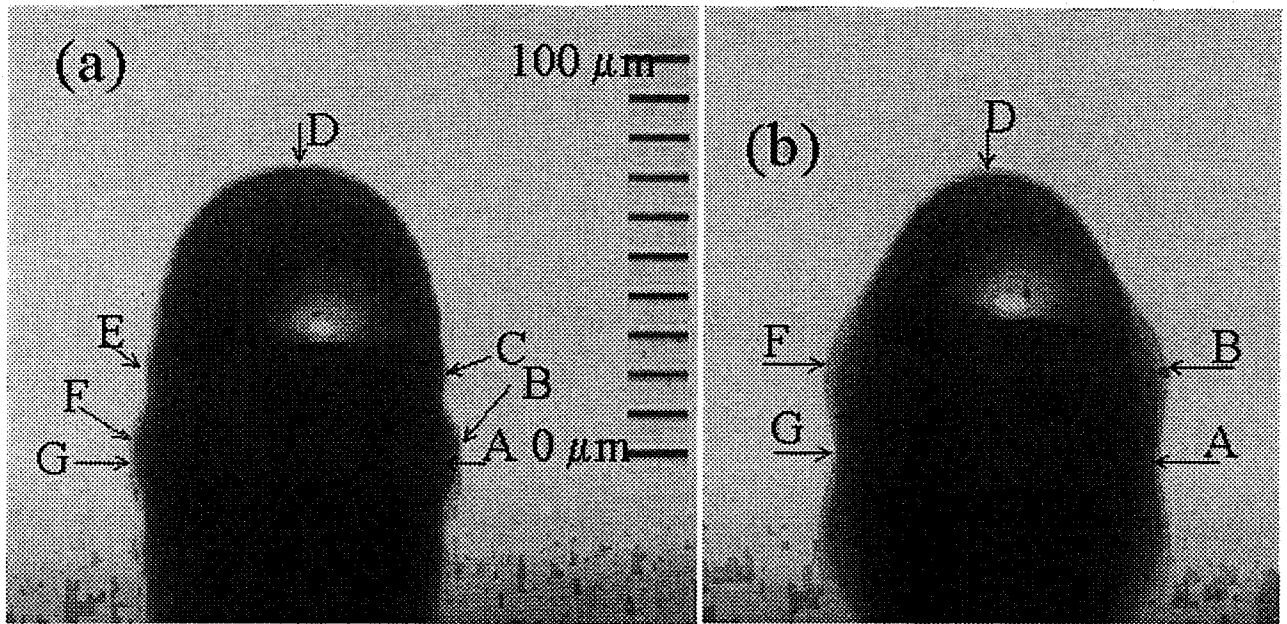


Figure 13: Measured points on the droplet surface. Points A and G determine the droplet wetting area diameter. D is the highest visible point of the surface, when viewing from the side, not always at the axis of symmetry. The distance from D to segment AG determines the visible droplet height H , above the surface (identified by the segment AG). The shadow below the surface and the light spot, 'inside' the droplet are optical effects. The accuracy in determining the vertical and horizontal position of A and G decreases for wetting angle values near 90° , and larger than 110° , respectively.

2.2.3. Image Analysis and Discussion of the Experimental Uncertainties

Image analysis is carried out using an image processing software (Optimas 6.2, Media Cybernetics, USA) that allows the measurement of droplet area and the motion analysis of selected points for a sequence of images. Figure 13 shows a measurement example of droplet wetting area diameter (distance between A and G) and droplet height (distance from point D to segment AG). It should be emphasized that such measurements involve uncertainties, e.g. due to the human identification of the measured points. In the case of clearly defined points such as in Figure 13 (b), 20 measurements of the points on the same image yield a standard deviation (in percentage of the initial droplet diameter) of 0.06, 0.54, 0.91, 0.44 and 0.16 % for the vertical position of D, the distance between D and segment AG, and the position of the single points A and G, as well as the wetting area diameter, respectively. It is worth noting that a wetting angle α larger than 110° can cause significant optical blurring (as in Figure 14, $30 \mu\text{s}$), and therefore increase the error for the wetting area diameter.

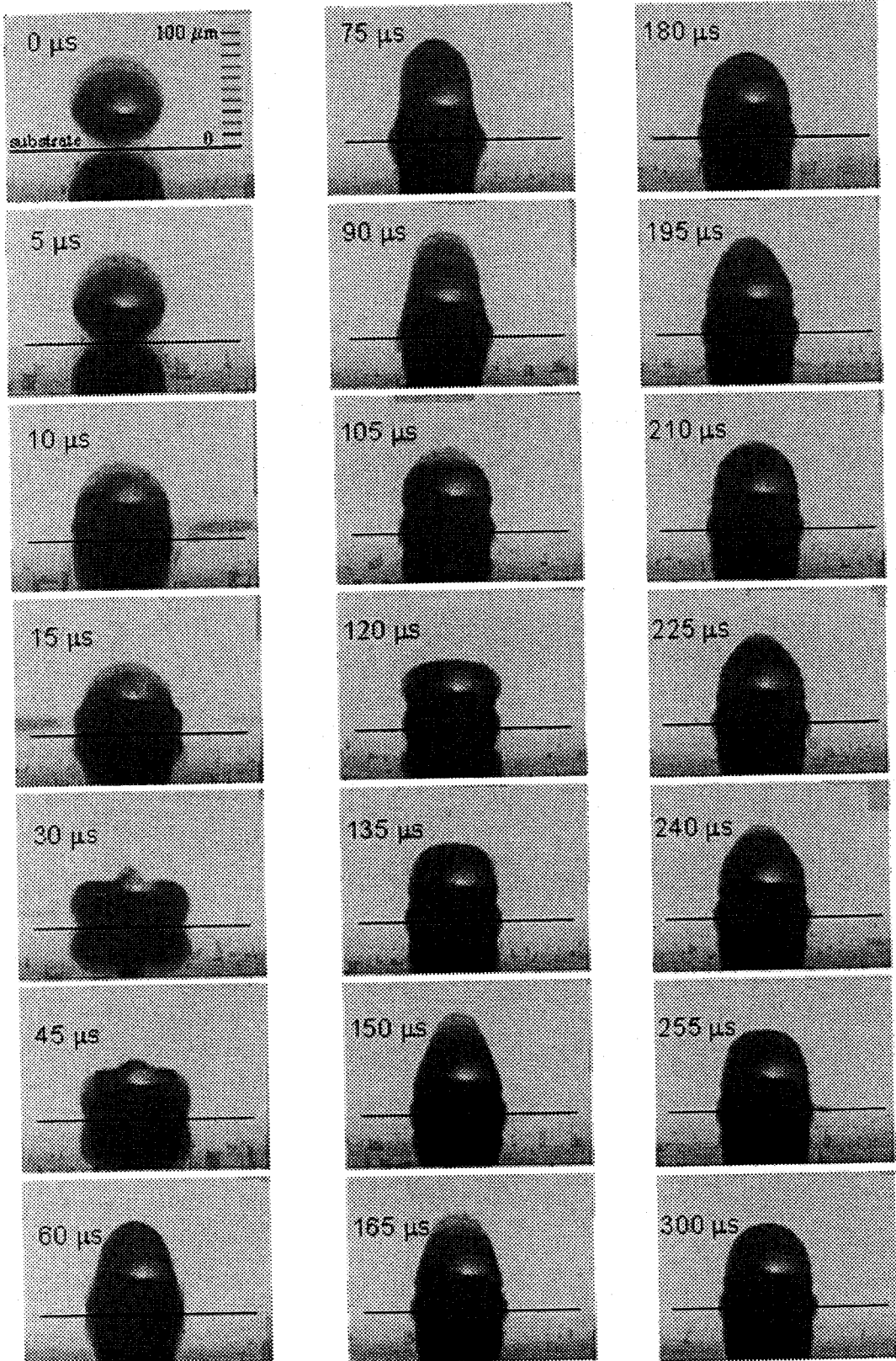


Figure 14: Spreading, oscillations and freezing of a solder droplet on a flat substrate. Initial conditions: $v_0 = 1.54 \text{ m/s}$, $d_0 = 80 \text{ mm}$, $T_{1,0} = 210^\circ\text{C}$, $T_{2,0} = 48^\circ\text{C}$.

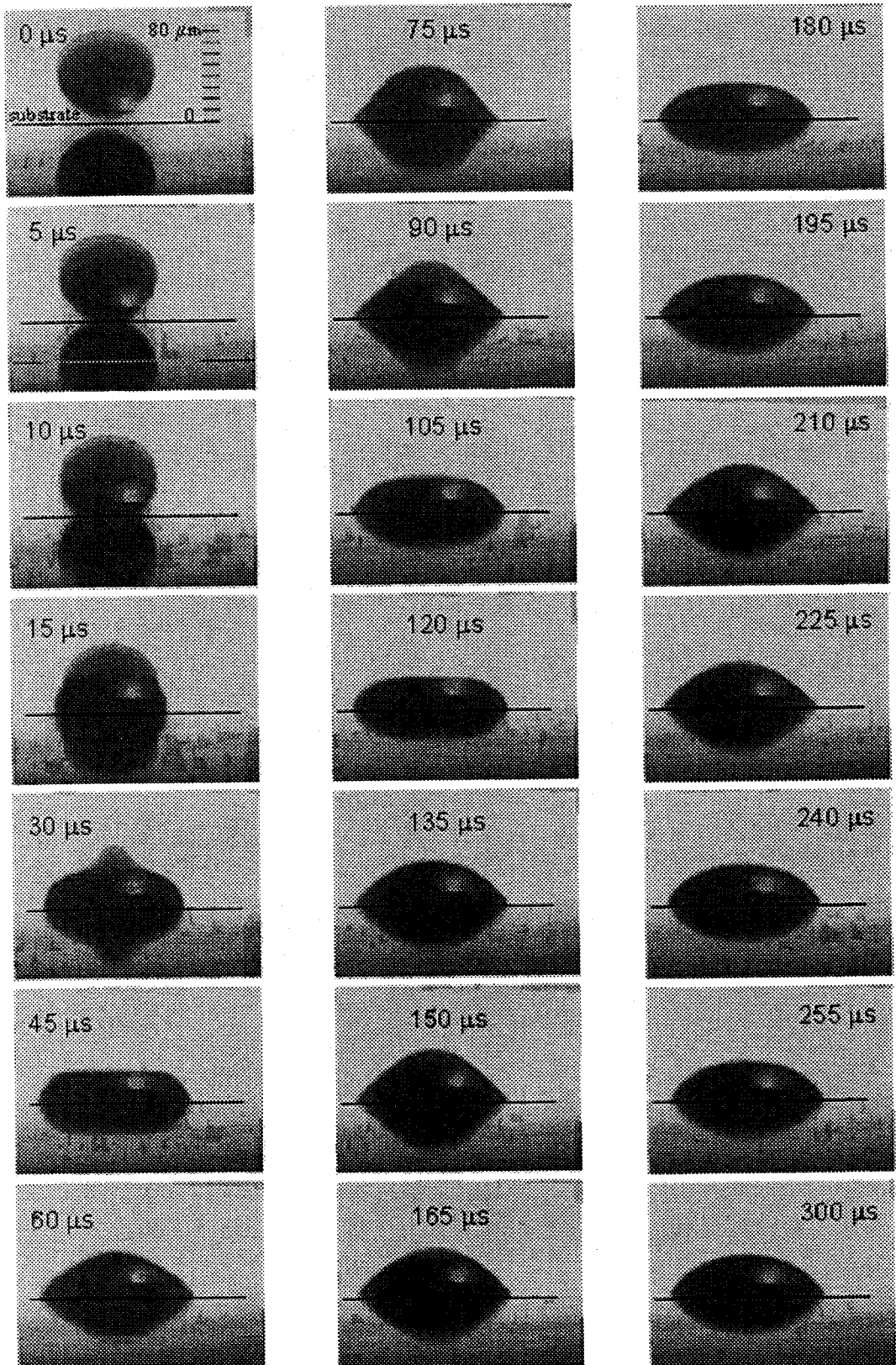


Figure 15: Spreading, oscillations and freezing of a solder droplet on a flat substrate. Initial conditions: $v_0 = 1.49 \text{ m/s}$, $d_0 = 84 \text{ μm}$, $T_{1,0} = 210^\circ\text{C}$, $T_{2,0} = 135^\circ\text{C}$.

The choice of a strobe microscopy technique that consists of building an impact sequence from a series of single pictures, each of them taken from a different droplet requires a highly reproducible process. There are several factors that can influence the reproducibility of droplet release and solidification. We examined with the setup used for the first series of experiments two possible perturbation sources, i.e. the stability in the drop position and velocity, as well as the importance of the wafer heating due to the heat released by solidification of the previous drop.

The positions of the top, bottom, left and right extreme points of 99 solder droplets in the same conditions as in the experiment have been measured with a constant delay between ejection and flash. The standard deviation in the horizontal position of the extreme right and left position is respectively 1.32 % and 1.46 % of the diameter (80 μm), and the standard deviation in the vertical position for the top and bottom points is 2.2 % ($\pm 1.76 \mu\text{m}$) and 1.72 %, respectively. The maximum standard deviation in the vertical position corresponds to a jitter in the droplet ejection of $\pm 1.17 \mu\text{s}$. Since this error is markedly larger than the error due to the human identification of the measured points, the major cause of uncertainties in the measurements is the needed repeatability of the visualization technique.

The magnitude of wafer slide heating due to the heat released by solidification of the previous drop has been evaluated in two ways. First, we estimated the final increase in the wafer temperature after the impact of a series of droplets that corresponds to our experimental conditions. Then, we estimated if the transient local heat release of a previous drop would affect the initial conditions for the actual drop. The final temperature increase was estimated as follows. Assuming that the heat released by the drops increases the wafer temperature uniformly, we express the temperature increase ΔT of a typical wafer slide (10mm by 50mm surface):

$$\Delta T = \frac{nE_Q}{\sum_i \rho_i V_i c_i} \quad (16)$$

where n , E_Q , ρ , V and c are the number of droplets, the heat released by droplet solidification and subcooling, the density, volume and heat capacity of each layer i of the wafer. In the case where 300 droplets (i.e. 3 sequences of 100 drops) at 210°C impact a wafer slide of the same composition as the one used in the experiments, we obtain that the wafer temperature increase ΔT is less than 0.1K, thus negligible. The transient effect of the previous droplet impact on the actual drop can be calculated accurately numerically, but we obtained an acceptable estimate by assuming that the entire E_Q is released at time $t = 0$, in a half sphere of an infinite radius. In other words, we consider that each droplet acts as an instantaneous heat source on the surface. In this

case, an analytical relation exists for the temporal and local evolution of the temperature (Poulikakos 1994). Considering a pitch distance between droplets of 166 micrometers (corresponding to a printing frequency of 12 Hz), the maximum transient temperature variation due to heat released by the previously impacting droplet for a distance of 166 micrometers from the heating source, was found to be 0.03 K in a gold hemisphere and 0.13 K in an Silicon hemisphere, thus negligible.

A further difference between the experiments and the ideal case of a spherical droplet impinging on a substrate is that there are still small residual shape oscillations from the ejection process at the instant of impact. Hence, the droplet shape at the time of impact is not absolutely spherical. This error can be estimated by observing the maximum error in non-sphericity on the pictures right before impact: at the distance used for printing, the diameter oscillation amplitude was $\pm 5\%$ of the droplet diameter. A series of measurements showed that the phase lag between the oscillations of the horizontal diameter and the vertical diameter equals π , thus this oscillation should not influence the measurement of droplet size, based on the visible area. Accordingly, the measurement of droplet velocity before impact was based on the motion of the two points at the extreme left and right of the droplet. Their height is a bit more difficult to determine than, for example, the height of the bottom point of the droplet, but it does not oscillate in the vertical direction.

2.3. Results

2.3.1. Experimental Conditions

Two series of experiments were performed. The first series was focused on the transient behavior of the spreading and solidification process. The second series was focused on the wetting angle dynamics. In the first series, sequences of molten solder microdroplet impingement on a colder wafer such as those shown in Figure 14 and Figure 15 have been recorded for different initial temperatures of the top surface of the wafer ($T_{2,0} = 48, 62, 81, 98, 118$ and 135 °C). The temperature of the bottom surface of the wafer was measured to be in each case 5 to 6 K lower than $T_{2,0}$. Each sequence was reconstructed from about 100 frames, the delay between drop release and flash being increased in steps of 5 μs between each frame. In each sequence, the time $t=0$ corresponds to the last picture before impact. The maximum corresponding error in determining the time $t=0$ when the droplet contacts the substrate is therefore 5 μs . The produced drops had a mean diameter d_0 in the range of 79.7 to 83.9 μm and a velocity v_0 in the range of 1.49 to 1.58 m/s, with average values of 81.4 μm and 1.52 m/s, respectively.

The characteristic numbers, defined in the nomenclature, are shown in Table 1. They are based on the following values for the thermophysical properties: $\sigma=0.345 \text{ Jm}^{-2}$, $\mu=0.00262 \text{ Pa s}$, $L=42000 \text{ J/kg}$, $c_L=238 \text{ J kg}^{-1} \text{ K}^{-1}$, $k_L=25 \text{ Wm}^{-1}\text{K}^{-1}$ and $T_M=183 \text{ }^\circ\text{C}$, and on the average measured values of velocities and diameter.

v_0 (m/s)	1.52 \pm 0.06					
$T_{2,0}$ [$^\circ\text{C}$]	48	62	81	98	118	135
Re	381					
We	4.4					
Ste	0.77	0.69	0.58	0.48	0.37	0.27
Oh	0.0055					
Pr	0.025					

Table 1: Initial conditions for the first series of experiments pertaining to the overview of the spreading and solidification process.

The second series of experiments, focusing on the evolution of the wetting angle, was performed with a more precise lighting, an increased optical magnification and time resolution, as described above. Four sequences of data were collected, where the surface temperatures and the initial impact velocities were varied as shown in Table 2. The mean value of the initial diameter d_0 was slightly smaller than in the first series of experiments ($74.1 \pm 2 \mu\text{m}$), and has been used for the calculation of the Reynolds and Weber numbers. The remaining experimental conditions were the same as in the first series of experiments.

v_0 (m/s)	2.35	2.31	1.49	1.51
$T_{2,0}$ ($^\circ\text{C}$)	145	59	65	119
Re	546	537	348	350
We	9.7	9.4	3.9	4.0
Ste	0.22	0.70	0.67	0.36
Oh	0.0057			
Pr	0.025			

Table 2: Initial conditions for the second series of experiments focusing on the evolution of the wetting angle

2.3.2. Qualitative Investigation of the Spreading and Solidification Process

Figure 14 shows a reconstructed sequence corresponding to an initial wafer temperature $T_{2,0}$ of 48 °C. A qualitative inspection of Figure 14 reveals that the spreading time (defined as the time taken by the droplet to spread to its maximum contact area) is approximately 30 μ s. The subsequent contour shapes caused by the upward motion of the droplet fluid indicate that the fraction of solidified mass is small within the first cycle of the droplet oscillation. The large variation of droplet height during the subsequent oscillation also suggests that the damping effect of viscous force is less important than the effect of surface tension force.

In the case of impact on a substrate with $We > 1$, the radial pressure gradient induced by the impact drives the process of droplet spreading (Attinger, et al. 2000a, Bennett and Poulikakos 1993, Haferl, et al. 2000, Schiaffino and Sonin 1997a). Surface tension forces, liquid viscous forces, and solidification work together to arrest the droplet spreading. According to Bennett and Poulikakos (1993), surface tension effects dominate the termination of droplet spreading over viscous effect when

$$We \ll 2.8Re^{0.457} \quad (17)$$

For the droplet impingement conditions in Figure 14, the right-hand-side of the above equation has a value of 42.3. Comparison with the Weber number, about ten times smaller, indicates that the condition for the droplet deposition shown in Figure 14 is well into the surface tension domain concerning the relative influence of viscous dissipation and surface tension.

Solidification effects can influence droplet motion (Schiaffino and Sonin 1997a). Neglecting the presence of contact thermal resistance between the substrate and the droplet bottom, the ratio of spreading time, t_{spr} , to the solidification time, t_s , can be estimated from (Schiaffino and Sonin 1997a),

$$t_{spr}/t_s = OhSte/Pr \quad (18)$$

The ratio calculated from the above equation is 0.17, indicating that the droplet spreading time is smaller than the solidification time. It is expected that the above ratio will be further reduced in the presence of interface thermal contact resistance. According to Figure 14, the spreading time is approximately 30 μ s before the recoiling motion

in the liquid region. No changes of the droplet shape are visible for the points located at the top of the droplet contour after 255 μs . Assuming that the arrest of droplet oscillatory motion is caused by solidification and not by viscous damping (which is reasonable since four visible ripples on the drop surface indicate that solidification arrested most of the drop motion), the ratio of the measured droplet spreading time to solidification time is 0.12. This agrees relatively well with the prediction of Eq. (18).

While droplet solidification is significantly slower than droplet spreading as shown above, it is also obvious that the subsequent oscillatory motion of the droplet is strongly affected by solidification. First, it can be shown by counting the number of frames for each oscillatory cycle that the oscillation frequency is increased with the upward propagation of the droplet solidification front, which reduces the total liquid mass of the droplet. Numerical simulations suggested that the oscillation frequency of an impacting droplet is closely related to the droplet natural frequency (Fukai, et al. 1993),

$$f \propto (\sigma/\rho_L V_L)^{1/2} \quad (19)$$

where V_L is the liquid volume. As the solidification front propagates into the molten region, the remaining liquid mass of the droplet decreases, which results in an increase of the oscillation frequency. Second, Figure 14 confirms that the ripples visible on the drop surface are due to a strong coupling between solidification and oscillations, which was suggested by numerical results pertaining to a comparable parameter range (Waldvogel and Poulikakos 1997, Xiong, et al. 1998).

Solidification can influence the spreading. This occurs by freezing at the wetting line (Schiaffino and Sonin 1997b), or by destruction of kinetic energy by solidification (Pasandideh-Fard, et al. 1998). The parameter measuring the spreading is the spread factor, β , defined as the ratio of the diameter d of the wetted substrate area over the initial droplet diameter d_0 . A comparison between Figure 14 and Figure 15 shows a significant increase of the maximum spread factor β_{max} when the substrate temperature is increased to 135 $^{\circ}\text{C}$. Assuming heat transfer between the substrate and the droplet only affects the spreading by delaying the solidification start (Attinger, et al. 2000a, Schiaffino and Sonin 1997a), the increase of β_{max} with increasing substrate temperature shows that solidification influences the spreading.

Other effects caused by an increase in the substrate temperature are visible in comparing Figure 14 and Figure 15. The final height decreases and no ripples are visible anymore: the droplet assumes a lens shape. These and other phenomena are discussed in the next section, which considers measurements from pictures of droplet spreading for increasing initial substrate temperatures.

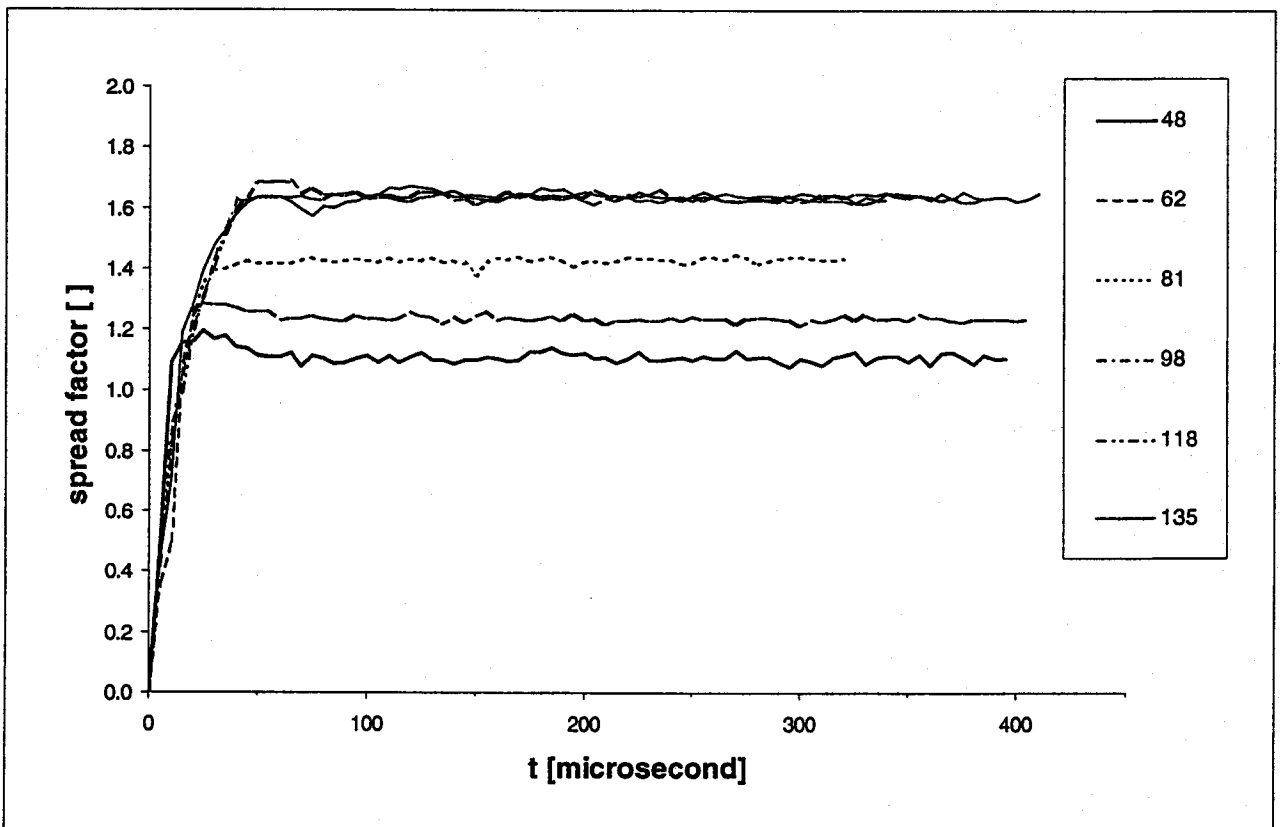


Figure 16: Time evolution of the spread factor β , with the substrate temperature $T_{2,0}$ as a parameter. The error is estimated in section 2.2.3.

2.3.3. Quantitative Investigation of the Spreading and Solidification

Process

The time evolution of the spread factor β , measured as in Figure 13, is shown in Figure 16 with the substrate initial temperature $T_{2,0}$ as a parameter. The time resolution is 5 μs . In the first 15 μs after impact, β increases from 0 to about 1 in a similar way for all values of $T_{2,0}$ examined. However, the attained final values β_∞ depend markedly on $T_{2,0}$. These final values increase with substrate temperature for $T_{2,0}$ between 48 and 98°C, and are almost constant for higher temperatures. The dynamic nondimensional parameters of impact, including We, Re, and Oh numbers, are approximately the same in every case. The difference is the thermodynamic parameter for phase change, the Stefan number, calculated in Table 1. The similar behavior of $\beta(t)$ for $T_{2,0}$ in the range 98 to 135 °C indicates that above 98°C (i.e. below $\text{Ste}=0.48$), there is no dependency of β on the Stefan number. This implies that solidification does not influence the spreading for $T_{2,0}$ over 98°C. Therefore, the assumption that the droplet spreads first and solidifies subsequently appears to be valid in this range of $T_{2,0}$. This is indicated by the good agreement between the final spread factor we measured for $T_{2,0}$ above 98°C ($\beta_{\text{max}} \approx 1.6$) and results from an analytical relation of Pasandideh-Fard et al. (1996). This relation estimates the maximum spread factor in the absence of solidification to be 1.65 with our mean values of Re, We, and with an advancing wetting angle value of 135° in the early stages of spreading (to be discussed later in connection with Figure 21 and Figure 22). It is worth noting that the above analytical relation is based on the assumption of a reasonably high Reynolds number, so as to produce a thin boundary layer in the liquid as it spreads, which is only partially valid in our case ($\text{Re} = 381$). We found it interesting that this relation predicts within 5% the spreading ratio of our measurements in the absence of solidification (i.e. when the substrate initial temperature is high). This is why we have tested the extension of this relation (Pasandideh-Fard, et al. 1998) that considers solidification effects by assuming that the influence of solidification is manifested by kinetic energy destruction. In this case, the model results do not agree well with our experimental results. The calculated maximum spread factors lie between 1.52 and 1.57, and our experimental values between 1.20 and 1.69. One possible reason for this discrepancy could be that solidification influences the spreading by arresting the wetting line via freezing rather than by destroying kinetic energy. In a published numerical study pertaining to the same parameter range as this experimental study, Waldvogel and Poulikakos (1997) have shown that freezing at the wetting line controls wetting line arrest. This has also been observed experimentally by Schiaffino and Sonin (1997b) for low Weber numbers. However, the history of the spread factor β for the

lowest substrate temperature $T_{2,0} = 48^\circ\text{C}$ (Figure 16) shows a maximum value of β significantly bigger (8%) than the final value of β . This measurement, concerning the highest Stefan number (0.77) of our measurement range, would contradict the hypothesis that freezing at the wetting line controls the maximum spreading. This apparent contradiction is probably a consequence of the significant blurring at the contact between splat and substrate in Figure 14 ($30\ \mu\text{s}$), which makes the accurate measurement of the maximum spread factor difficult.

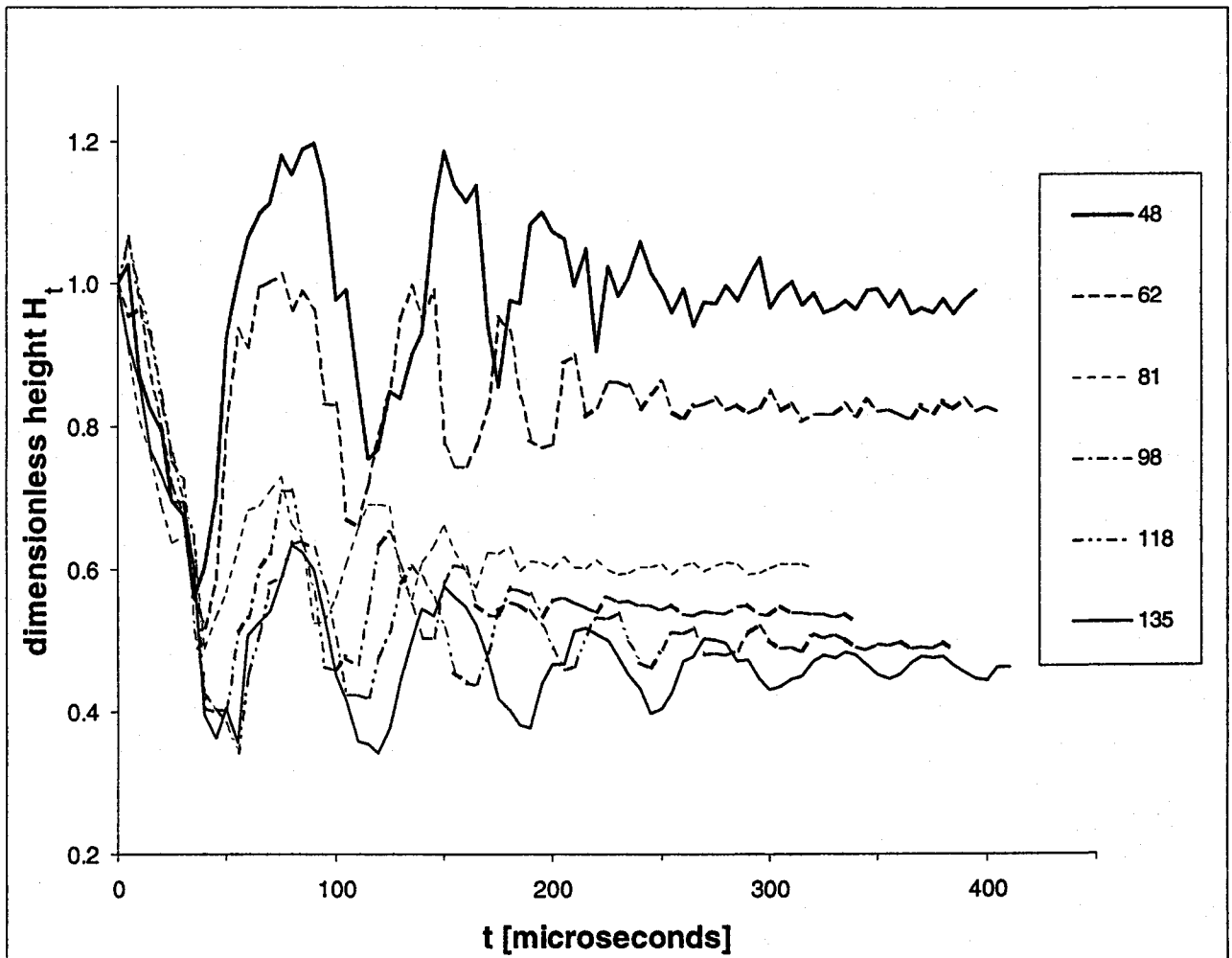


Figure 17: Time evolution of the dimensionless visible droplet height over the substrate H_t , with the substrate temperature $T_{2,0}$ as a parameter. The error is estimated in section 2.2.3.

Figure 17 shows the time evolution of the dimensionless visible droplet height over the substrate (defined in Figure 13 as the maximum height when viewing from the side at any time instance), with $T_{2,0}$ as a parameter. It should be emphasized that the visible droplet height does not always correspond to the height of the intersection of the axis of symmetry with the free surface. For example, simulations by Waldvogel and Poulikakos (1997) have shown that, in the early stages of the spreading, the height of the intersection of the axis of symmetry with the free surface is smaller than the droplet height visible from the side. The motion of the droplet height shown in Figure 17 can be termed as a damped oscillation with increasing frequency. Figure 18 shows the final, maximum and minimum values of the visible droplet height, each corresponding to a fixed substrate temperature. The maximum visible height is measured from the beginning of first recoiling, and the final visible height is measured by averaging the height of the 10 last frames of each visualization series. The final, maximum and minimum values of the visible droplet height decrease monotonically with $T_{2,0}$. At temperatures below 98°C , the monotonical decrease of final height with substrate temperature can be correlated with the increase of β_{\max} with substrate temperature (Figure 16).

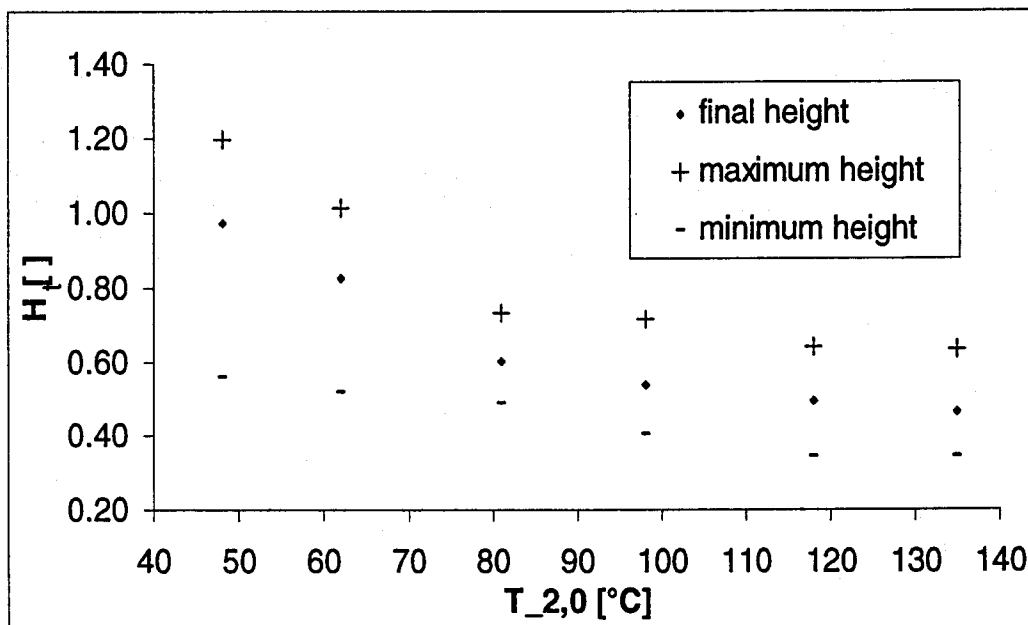


Figure 18: Final, maximum and minimum droplet dimensionless visible height H , as a function of $T_{2,0}$. The error is estimated in section 2.2.3.

Quantitative information about the solidification time has been extracted from Figure 17 as follows. We assume that the droplet is frozen when the droplet height remains constant (within $\pm 2\%$ of the initial diameter) for a time length more than half a period of its oscillations (corresponding to a series of 10 successive frames). The apparent solidification time is then defined arbitrarily as the time of the first frame of the above mentioned series. The apparent solidification time is represented in Figure 19. It depends nonmonotonically on $T_{2,0}$, with a minimum of about $165 \mu\text{s}$ at $T_{2,0} = 98 \text{ }^\circ\text{C}$. This nonmonotonic dependence of the apparent solidification time on $T_{2,0}$ indicates a nonmonotonic dependence of the effective solidification time on $T_{2,0}$, as calculated in previous numerical simulations (Waldvogel and Poulikakos 1997, Xiong, et al. 1998).

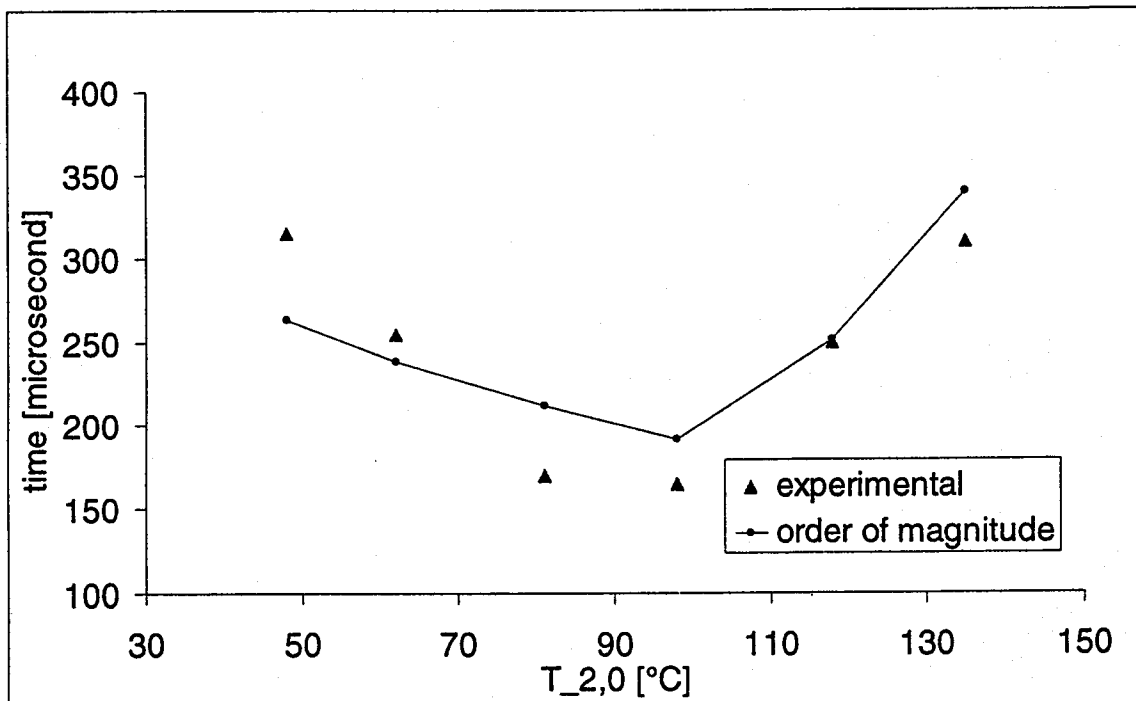


Figure 19: Solidification time t_s as a function of $T_{2,0}$. The experimental values refer to the apparent solidification time, and the order of magnitude values refer to Eqs. (20) to (23).

An order of magnitude explanation of this nonmonotonic dependence of the solidification time on $T_{2,0}$ is presented hereafter. If we neglect the effect of superheat and subcooling, we can consider that the energy E_s released by the solidification of the droplet is constant with respect to $T_{2,0}$:

$$E_s = \rho VL \quad (20)$$

The solidification time t_s is expressed as follows:

$$t_s = \frac{E_s}{\dot{q}} \quad (21)$$

We also assume that the heat flux \dot{q} can be expressed by

$$\dot{q} = h_E S (T_M - T_{2,0}) \quad (22)$$

where h_E is an effective heat transfer coefficient and

$$S = \frac{\pi}{4} d_0^2 \beta_\infty^2 \quad (23)$$

is the contact surface between splat and droplet (the final spread factor β_∞ is measured from Figure 16). The variation of the solidification time t_s therefore only depends on \dot{q} , i.e. on the product of S (increasing with $T_{2,0}$) and the temperature difference (decreasing with increasing $T_{2,0}$). The coupling of these two opposite trends leads to a minimum in the solidification time. Values of the solidification time calculated by this order of magnitude model described above are shown in Figure 19. The value of the effective heat transfer coefficient used in Eq. (22) ($h_E = 4.3 \cdot 10^5 [\text{Wm}^{-2}\text{K}^{-1}]$) has been determined by minimizing the differences between the model and the experiments results, in a least square sense. It is worth noting that h_E expresses both the effects of convection in the liquid part of the splat and conductive heat transfer at the splat/substrate interface. These two heat transfer modes have been respectively examined by (Zarzalejo, et al. 1999) and (Wang and Matthys 1996), matching experiments with numerical or analytical models. Although the goal of our analytical model is to give a physical explanation of the observed non-monotonic dependence of the solidification time on $T_{2,0}$ and not to provide quantitative results, the estimated value for h_E

agrees in an order of magnitude sense with the results of (Wang and Matthys 1996). The effect of thermal contact resistance on the spreading dynamics cannot be accurately pursued with the present approximate model. A thorough study of this effect has been performed by Xiong et al. (1998), who matched the shapes of solidified droplets with the shapes obtained by numerical simulations at different Biot numbers.

2.3.4. Wetting Angle Dynamics

The visualization method presented here allows the measurement of the evolution of the apparent wetting angle α . This angle is always measured at the contact line between the droplet and the wafer substrate, as shown in Figure 20, which is a representative frame for our wetting measurements. Each frame allows a double measurement of α , on the left and on the right of the droplet. A graphical estimate in Figure 20 yields an angular precision of ± 12 degrees. It is worth noting that α can only be considered to be a *wetting* angle as long as no solidification has occurred at the contact line. Indicators of the fact that solidification has not occurred are for example the temporal evolution of the spread factor and the temporal variation of the apparent wetting angle. The experimental conditions for the experiments on wetting dynamics are slightly different from the first series of experiments performed in this study, as described above. The time resolution of 300 ns used is well below the jitter due to instabilities in droplet ejection, so we have selected to base our interpretation of the results on plots of the wetting angle as a function of the spread factor β (Figure 21) instead of as a function of time (Figure 22).

Figure 21 shows the evolution of the apparent wetting angle α as a function of the spread factor β for the four cases described in Table 2. These cases differ by the impact velocity v_0 and the initial substrate temperature $T_{2,0}$. At least two regimes can be distinguished in Figure 21: a first regime where α decreases linearly ($\beta < 0.8$), and where the behavior is comparable in the four measurement sequences, and a second regime ($\beta > 0.8$), where no consistent behavior for all cases can be observed. In the first regime, measurements and a general optical inspection of the frames do not reveal significant angle and shape differences between the four examined cases, defined by their respective initial impact velocities v_0 and surface temperature $T_{2,0}$: (2.35, 145), (2.31, 59), (1.51, 119) and (1.49 m/s, 65 °C). A linear curve fit in this first regime yields the following correlation, shown in Figure 21:

$$\alpha(\beta) = 160^\circ - 71\beta, \beta < 0.8 \quad (24)$$

The second regime can be either a horizontal plateau ($\alpha \sim 90^\circ$) terminated by a region where the value of α oscillates at the maximum value of β as in the case (1.51, 119), or a regime of increase and subsequent decrease of α as in the cases (2.31, 59) and (1.49, 65), where α first increases to a local maximum and then decreases to a final value of about 90° (the interpretation of the results in Figure 21 is aided by plots such as Figure 22, where time is a coordinate).

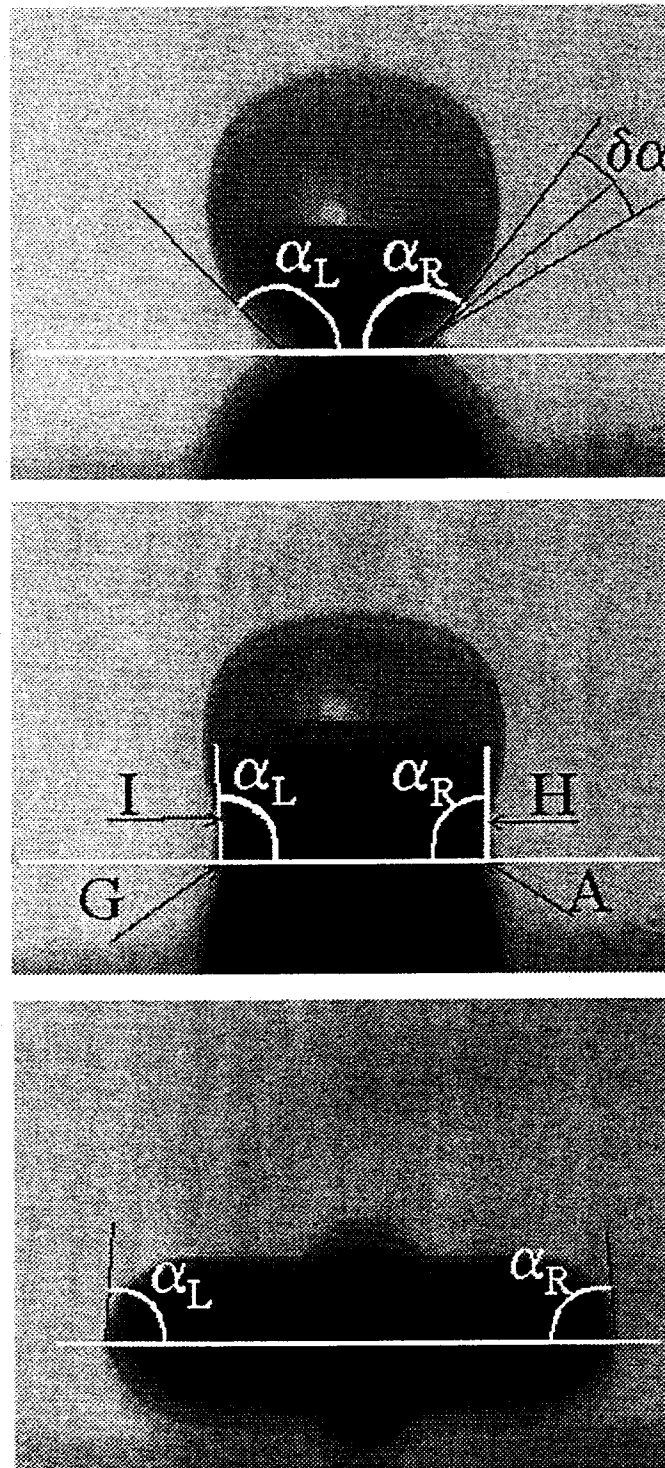


Figure 20: Determination of the apparent dynamic wetting angles. Angle α_L is determined by points (I,G,A), and angle α_R by (H,A,G). The measurement uncertainty $\delta\alpha_R$ comes primarily from the positioning of A and H, its value is estimated $\pm 12^\circ$.

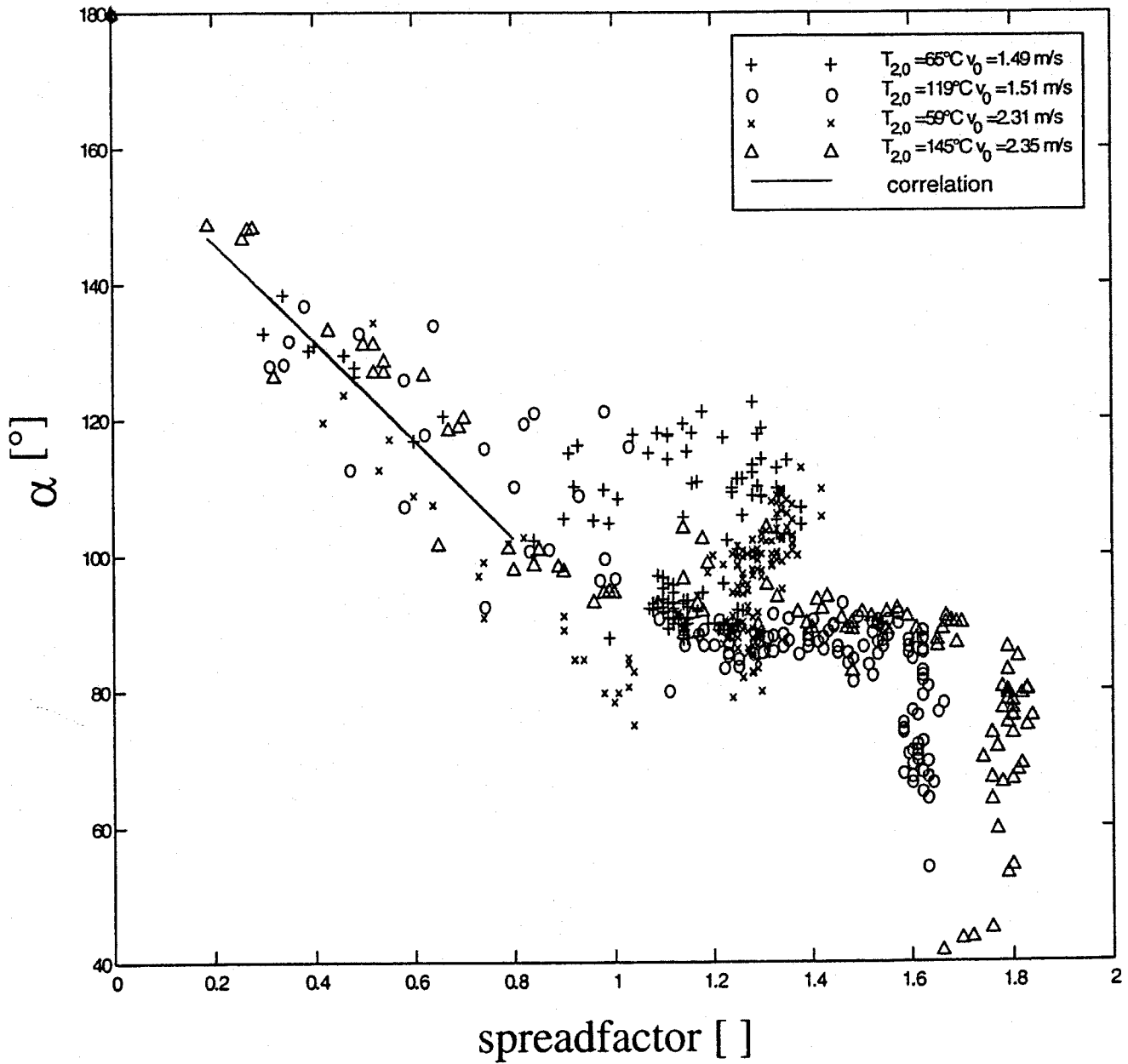


Figure 21: Evolution of the wetting angle α as a function of the spread factor β for the specified initial substrate temperatures $T_{2,0}$ and impact velocities v_0 . The angular error is estimated in Figure 20.

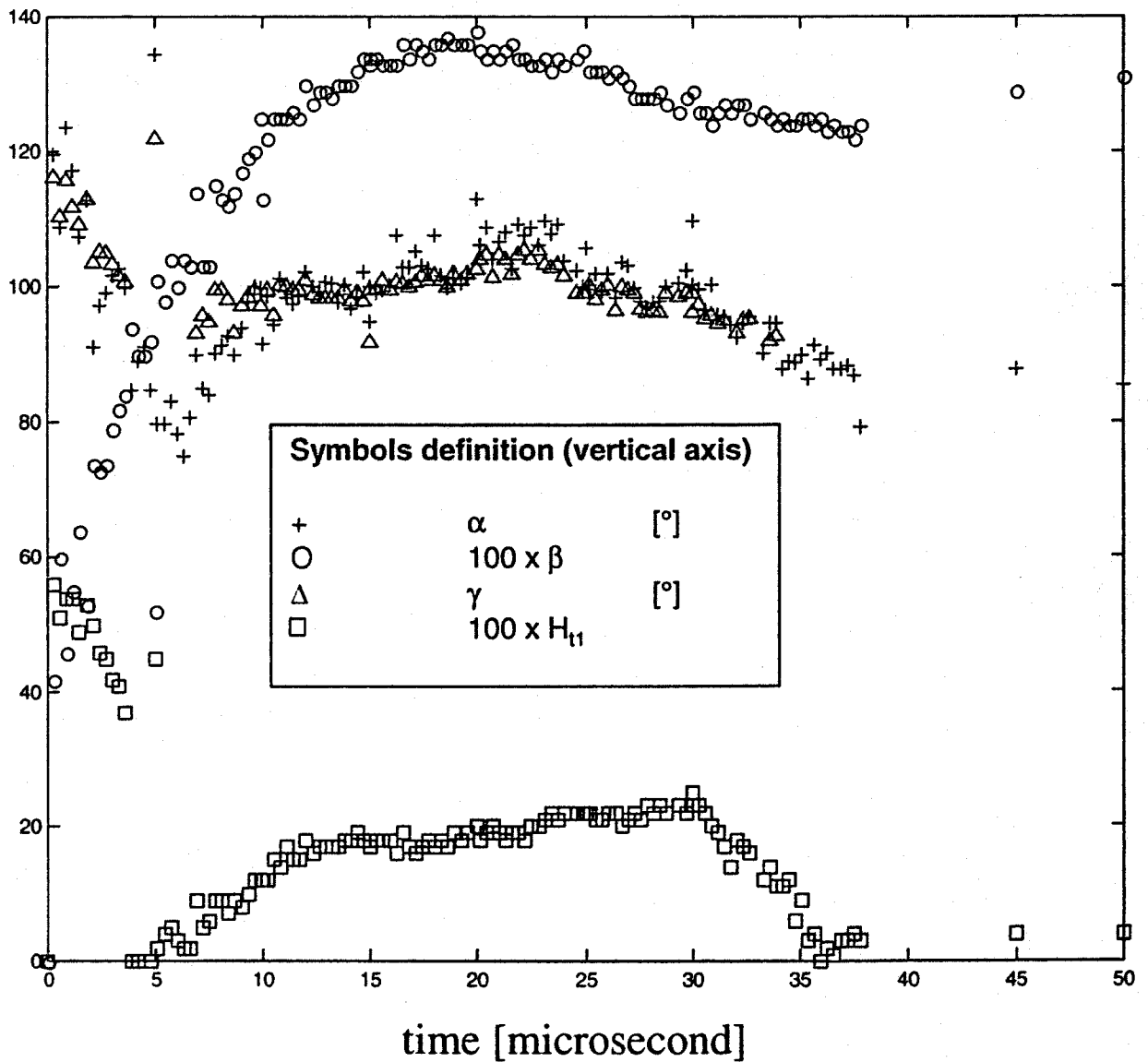


Figure 22: Time evolution of the spread factor β , the contact angle α , the first ripple angle γ and the first ripple nondimensional height H_{t1} in the case ($v_0=2.31\text{m/s}$, $T_{2,0}=59^\circ\text{C}$). The error is estimated in section 2.2.3 and in Figure 20.

The last case (2.35, 145) can be viewed as a combination of a plateau and a small zone of increase and subsequent decrease of α for $\beta \in [1.1, 1.3]$. It is worth stressing that, although not explicitly extractable from Figure 21 because time is not a coordinate, oscillations of the value of α at the maximum values of β (for example $\beta = 1.6$ and $\beta = 1.8$) were observed. Witness to this fact are the frames between 45 and 150 μs in Figure 15.

The results for α in the first regime can be interpreted as follows. The decrease of the apparent wetting angle value with the spread factor corresponds qualitatively to the predictions of Hoffman's experimental correlation (Dussan 1979, Hoffmann 1975), which expresses that the wetting angle decreases with decreasing capillary numbers (this is the case in the early part of the impact, because the spherical droplet shape induces a contact line velocity that decreases with time):

$$\alpha = f_{\text{Hoff}} \left(Ca + f_{\text{Hoff}}^{-1}(\alpha_{\text{eq}}) \right) \quad (25)$$

$$f_{\text{Hoff}}(Ca) = 4.54Ca^{0.353}, \quad Ca < O(0.1) \quad (26)$$

The second term in the parenthesis of Eq. (25) is a correction factor for the influence of the equilibrium wetting angle α_{eq} . Theoretical verification of Hoffman's correlation has been obtained for the case of perfect wetting ($\alpha_{\text{eq}} = 0$) via hydrodynamic analyses by Voinov and Tanner (Tanner 1979, Voinov 1976). Equation (26) expresses this correlation for the range of Capillary numbers that pertains to our study (Kistler 1993).

Hoffman suggested analytically that flow inertia could influence α for $We > 0.015$ (Hoffmann 1975). The analyses of Tanner and Voinov focused on the slow viscous flow regime, neglecting flow inertia in the Navier-Stokes equations. Publications can be found stating that inertia effects on the wetting angle can be ignored for $Ca \leq O(0.1)$, without commenting on the influence of the Weber number (Kistler 1993). However, most of these wetting studies are performed with high viscosity oils. In the first regime of the droplet spreading observed in this study, the measured contact line velocities of 2-4 m/s correspond to Ca of the order of $1.5 \cdot 10^{-2}$ - $3.2 \cdot 10^{-2}$, and simultaneously to We of the order of 7 to 28. These moderate Weber numbers clearly imply that the fluid inertia is not negligible in comparison with capillary forces. This indicates the existence of situations where inertia is not negligible even at low Ca , for example in the case of low viscosity materials such as liquid metals.

A second limitation of Hoffman's correlation and of its hydrodynamic justifications is that they are expressed for steady flows only. Therefore, the application of

Hoffman's correlation to an unsteady droplet impact is questionable. However, since Hoffman's correlation is the only widely known available general wetting correlation, it is worth comparing it with our measurements.

Quantitatively, it is difficult to compare the evolution of α with the evolution of the capillary number in this first regime since the equilibrium wetting angle is a priori unknown, and since we only measured an average velocity at the contact line, meaning an average Ca. Assuming an equilibrium wetting angle near zero, these values of Ca of $1.5 \cdot 10^{-2}$ and $3.2 \cdot 10^{-2}$ correspond via Eqs. (25) and (26) to wetting angles of respectively 59° and 77° . The assumption of a small equilibrium wetting angle value has been confirmed to some extent in this study experimentally. To this end, we placed on a microheater a wafer slide supporting a solidified solder droplet (80 μm diameter) and heated the slide at 180°C during two minutes. Frames (a) and (b) in Figure 23 are top views of the droplet respectively before (at solid state) and at the end of the heating. The drastic increase of diameter of the drop during melting indicates that the melting drop wets the substrate very well creating a film-like structure, corresponding to a small equilibrium wetting angle. We used Atomic Force Microscopy (AFM) in order to quantify the wetting angle value as follows. The slide was removed from the heater right after heating and cooled on a steel surface at ambient temperature in order to freeze the equilibrium wetting angle. It is worth noting that AFM measurements of a liquid surface, in particular of a contact line region at relatively high temperatures are not very reliable and difficult to perform since AFM has been developed for solid surfaces. Implementation in liquid and molten interfaces measurements is at best at its infancy (Haferl et. al., 1999). The measured values of the frozen contact angle, from the border of the contact line up to 9 microns from that line, were smaller than 30° (Figure 23). Even if the equilibrium angle were 40° , the dynamic angles values calculated with Hoffman's correlation would only slightly increase (respectively from 59° to 65° and from 77° to 81° as discussed earlier), which still does not agree with the measured values that all lie between 90° and 140° . The fact that a single correlation, Eq. (24), could be extracted from impacts with different velocities (Figure 21) also suggests that Hoffman's correlation is not valid in the first part of the curve describing our measurements. Since Hoffman's correlation does not account for the bulk fluid inertia and the influence of the free surface shape in the vicinity of the contact line, further measurements had to be performed in order to consider the influence of these phenomena on droplet spreading.

The influence of the free surface motion near the wetting angle on this same angle can be examined by tracking the position of the first free surface ripple relative to the contact line. A characteristic free surface point describing the location of the first ripple is the lowest point above the substrate where the horizontal cross-section of the droplet reaches a local maximum, represented by point *B* (or *F*) in Figure 13 (this point

can fall on the contact line, e.g. when the drop has a meniscus shape). An indicator of the influence of the first ripple position on the contact angle α is the angle γ , defined as the angle BAG (or AGF) in Figure 13. It is worth noting that γ cannot be defined when points B and A (or F and G) coincide. This 'first ripple angle' γ , when defined, is shown in Figure 22 as a function of time for the case (2.31 m/s, 59°C). A clear relation between α and γ during this first part of the spreading is obvious, and is also visible in the three other wetting angle measurement sequences (not shown in Figure 22 for clarity), as well as in the frames 2 and 3 of Figure 15. The nondimensional height of the first ripple above the substrate H_{r1} is also shown in Figure 22 in order to determine unequivocally the position of the first ripple.

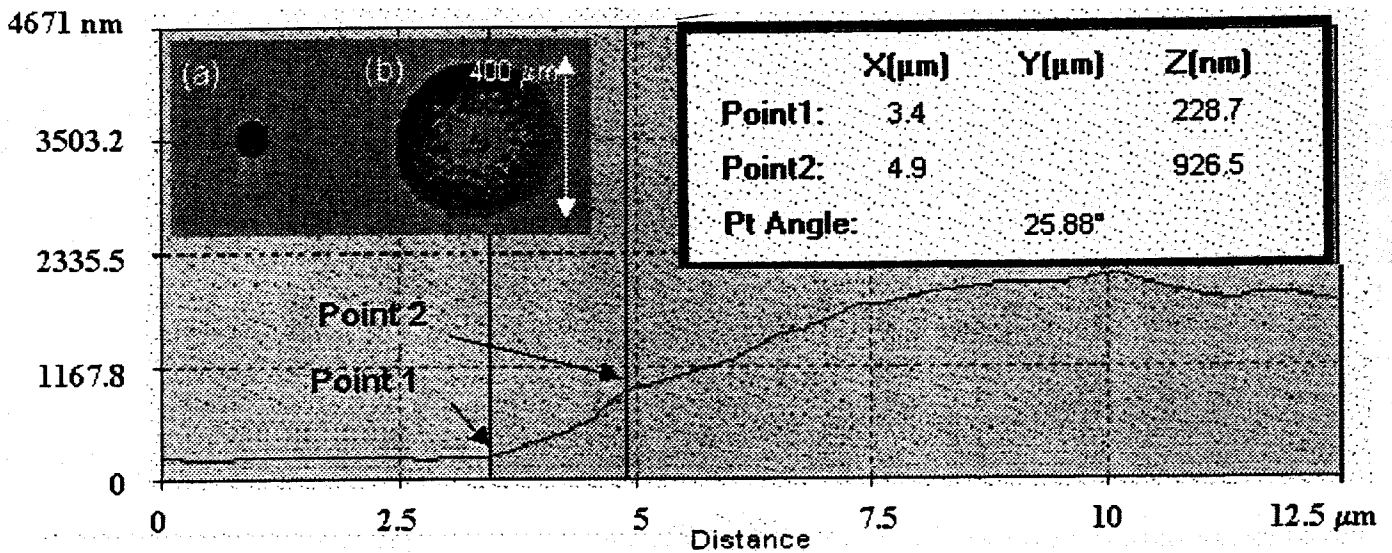


Figure 23: Contact angle measurement with Atomic Force Microscopy. The two vertical lines determine the position of the angle measurement on the splat profile. Frames (a) and (b) show the top view of the same (previously solidified) drop before (a) and after 2 minutes heating (b) above its melting temperature (183°C).

The second regime of the spreading ($\beta > 0.8$) allows a better insight into the relation between γ and α . In Figure 22 these two angles values exhibit a coordinated increase and subsequent decrease for $t \in [15, 30 \mu\text{s}]$. This indicates that the apparent wetting angle and the bending of the free surface over it represented by γ are dependent. This makes sense physically, for example, when one considers the limit case where the contact line freezes suddenly and the first ripple continues to advance because of the bulk fluid flow, as in cases (1.49 m/s, 65 °C) and (2.31, 59) in Figure 21: here the apparent α will increase only because of the combination between bulk fluid dynamics and heat transfer, and not because of wetting phenomena. Frames 3-5 in Figure 14 show a similar increase and subsequent decrease of the value of alpha, as in the measurement (1.49, 65). It is worth noting that the apparent receding observed in both low-temperature cases (Figure 16, Figure 21 and Figure 22) is not consistent with the fact that solidification arrests the spreading at low temperature. The exact reasons are not clear to us at the present time.

Another increase and subsequent decrease of the value of α , smaller than in both low-temperature cases, is also observed in Figure 21 in one high temperature case (2.35, 145). This can also be correlated with a bending of the free surface above the substrate and a corresponding increase of γ . Contrary to both low-temperature cases, this bending is probably caused by the bulk fluid motion instead of solidification, since the latter only affects the motion of the contact line at a later stage. In the other high temperature case (1.51, 119) the wetting angle remains approximately constant at 90° for $\beta > 1$, while the characteristic point describing the location of the first ripple falls on the contact line. This absence of bending of the free surface near the substrate could be explained by an impact velocity lower than in the case (2.35, 145).

We also attempted to test Hoffman's correlation in the second regime for both our high substrate temperature cases. Contact line velocities were estimated to be 1.44m/s and 0.84 m/s for the cases (2.35 m/s, 145 °C) and (1.51, 119) respectively, in the ranges of $\beta \in (1.4, 1.8)$ and $(1.2, 1.6)$. These velocities correspond to Ca of $1.1 \cdot 10^{-2}$ and $6.3 \cdot 10^{-3}$. The resulting wetting angle values obtained from Hoffman's correlation, assuming again an equilibrium wetting angle of zero, are 53 and 43°, respectively. These values differ greatly from the measured values of about 90°. It should be noted that this finding is not sensitive to the assumed value of the equilibrium wetting angle: even if the measured equilibrium angle were 40°, the wetting angle predicted by Hoffman's correlation would be increased by less than 11 degrees, which is far from sufficient to yield agreement with our measurements.

A few examples of quantitative and qualitative disagreements between transient wetting measurements and Hoffman's correlation have recently been published. In the case of the impact and spreading of a millimeter-size droplet, opposite trends between measurements and Hoffman's law have been shown (Megaridis, et al. 2000). In the case

of a coating layer flowing on a moving curtain, Blake et al. (1999) have shown experimentally that there is evidence of a nonlocal hydrodynamic influence on the dynamic contact angle, a finding that clearly invalidates the local nature of Hoffman's law, as stated by Eq. (25). Novel approaches are therefore needed for gaining a better insight on wetting physics in regimes exhibiting inertia and non-stationary flow patterns. There is today a wide agreement, justified by preliminary results (Blake and Ruschak 1997), that discrete methods such as Molecular Dynamics (Haile 1992) will show the way to a deeper understanding of wetting. However, current computing limitations for Molecular Dynamics, in terms of time and space scales ($O(\text{ps}, \text{nm})$), will prohibit most experimental validations of this new findings in the next decade, so that complementary innovative approaches would be welcome. To this aim, there is currently an interesting trend towards hybrid approaches, where continuum and Molecular Dynamic schemes are applied together to the same macroscopic problem, respectively to the bulk fluid domain and the microscopic domain. With hybrid methods (Hadjiconstantinou 1999), where the continuum and molecular solutions are constantly matched over a narrow overlap region, the space scale limitation of Molecular Dynamic simulation is removed. However, there is to the best of our knowledge currently no available approach that would remove the time scale limitation, which is inherent to the molecular dynamics method.

Chapter 3: Melting and Resolidification of a Substrate caused by Molten Microdroplet Impact³

3.1. Review of the Literature

Understanding and optimizing the substrate *melting* due to the heat released by the impacting molten droplet (a phenomenon sometimes called *remelting* in the literature, assuming implicitly that the substrate is produced by previously solidified drops) is important for novel spray deposition manufacturing technologies like microcasting (Zarzalejo, et al. 1999) and net-form manufacturing (Orme, et al. 2000). These techniques aim at building metallic parts of a typical size of the order of 1 to 100 millimeters by targeted deposition of drops on top of each other, with a droplet size ranging from 100 μm to a few millimeters. Samples built with aluminum (Orme, et al. 2000) or steel and copper (Amon, et al. 1996) are shown in Figure 6 and the importance of the remelting amount on the sample shape and quality has been discussed in the introduction of this thesis.

Driven by the importance of these manufacturing technologies, some aspects of the physics involved in the substrate melting problem have been examined experimentally, analytically as well as numerically. Experimental investigations of substrate melting involving millimeter- and in particular micrometer-size droplets are quite challenging, due to the very fast fluid flow and thermal transients as well as the small length scales involved. In addition, since the materials of interest are non-transparent metals, it has been to the best of our knowledge not possible to date to investigate experimentally neither the flow inside the deforming molten region nor the phase change interface motion. Accordingly, experimental studies have been performed with rather larger millimeter-size droplets, focusing on specific aspects like heat transfer between the drop and the substrate (Pasandideh-Fard and Mostaghimi 1996, Wang and Matthys 1996), dynamic spread factor and contact angle (Megaridis, et al. 2000, Pasandideh-Fard, et al. 1996), shape of solidified splats (Madejski 1976), maximum substrate melting depth through cross-sectioning and polishing (Kang, et al. 1995, Zarzalejo, et al. 1999). Up to now, all the theoretical studies on substrate melting have either neglected or drastically simplified the fluid dynamics in the droplet without accurate justification and in order to (understandably) provide mathematical tractability. This is an approach that is certainly an acceptable first step toward understanding a complex problem. Rangel and Bian (1997) added substrate melting to Madejski's analytical approach (described in

³ Most of the material of this chapter has been submitted to the ASME Journal of Heat Transfer, as Attinger, D., and D. Poulidakos. Melting and Resolidification of a Substrate caused by Molten Microdroplet Impact, and presented at the International Conference of Theoretical and Applied Mechanics, Chicago, Illinois, USA as: Attinger, D., V. Butty, S. E. Haferl, and D. Poulidakos. 2000. Numerical Modeling of Microdroplet Impact and Solidification with Substrate Melting.

the introduction) and used a better analytical model for the fluid flow, satisfying the shear-free condition at the free surface of the liquid. They did not consider thermal contact resistance between the splat and the substrate, assuming that the remelting creates a continuous contact between splat and substrate (Schmaltz and Amon 1996), and neglected radial conduction in the thermal energy equation. Wang et al. (1998) proposed operational maps for the melting of a substrate suddenly brought in contact with a thin layer of solidified metal experiencing no motion, focusing therefore on the solidification aspect of the problem. This situation could be comparable to substrate melting caused by drop impact, assuming that the fluid dynamics time scale is much smaller than the solidification time scales (Jones 1971), which can be justifiable but only for a certain range of initial conditions (Bennett and Poulikakos 1994, Madejski 1983, Madejski 1976, Mcpherson 1980). The model of Wang et al. (1998) simulates phase change under non-equilibrium conditions, assuming a constant heat transfer coefficient between the substrate and the splat before, during and after substrate melting (this coefficient accounts for the imperfect heat transfer between both the drop and the substrate and was studied extensively in (Wang and Matthys 1996)). Wang et al. (1998) produced substrate melting maps identifying whether substrate melting occurs, and quantified the melting depth as a function of the superheat parameter SHP and the interfacial Biot number Bi for a given pair of materials. At least two publications have reported comparisons between simulations and experiments, in which the substrate melting depth was evidenced by cross-sections. First, Kang et al. (1995) studied the impact of a 3mm droplet on top of a previously solidified one, at a velocity of 2.1 m/s. Their 1-D solidification model (with 2-D substrate conduction) was shown to provide a reasonable agreement with experiments with eutectic tin-lead solder, at least in the region near the center of symmetry. Observing that the occurrence of substrate melting depended on the radial location, they concluded that consideration of the radial heat conduction in the splat was important for a better modeling of substrate melting. Second, Zarzalejo et al. (1999) performed experiments and calculations for steel droplets on steel, and concluded that convection heat transfer cannot be neglected for modeling the substrate melting, even in the case of large droplets.

The aim of the model presented in this chapter is to take into account accurately the complex fluid flow phenomena of the substrate melting problem, in order to examine qualitatively and quantitatively their importance on the substrate melting phenomenon, particularly by considering the associated convection and free-surface driven flow. The starting point of this study is a model for droplet impact involving the full Navier-Stokes equations with free surface modeling, convective heat transfer and solidification (Waldvogel and Poulikakos 1997). In this chapter the model is extended to account for substrate melting and resolidification, with consideration of the interfacial contact resistance and the mixing of substrate and droplet masses. In addition, a

more efficient grid generation algorithm is utilized. Detailed results are presented for the impact of microdroplets ($O(100)$ μm diameter) of eutectic tin-lead solder on a substrate of the same material, for they relate directly to net shape manufacturing by *printing* of liquid metal microdroplets. This technology constitutes a focal point of the research activities of the Laboratory for Thermodynamics in Emerging Technologies (Attinger, et al. 2000b, Waldvogel, et al. 1998, Waldvogel and Poulikakos 1997, Xiong, et al. 1998) at ETH Zurich. Numerical results are compared to existing experiments of other investigators with larger steel droplets (Zarzalejo, et al. 1999).

3.2. Numerical Model

3.2.1. Fluid dynamics

A mathematical model is formulated to simulate the impact of an initially spherical molten droplet on a flat substrate beginning at the instant of contact. It is based on the Navier-Stokes equations applied to an axisymmetric coordinate system shown in Figure 24, where R , Z and θ are the radial, axial and azimuthal dimensionless coordinates. Constant thermophysical properties are assumed for the fluid. The governing equations are written using a Lagrangian approach (Bach and Hassager 1985, Fukai, et al. 1993), allowing an accurate tracking of the free surface. Nondimensionalization is performed with respect to the droplet initial diameter d_0 , the impact velocity v_0 , the liquid density ρ_L , and the initial pressure in the drop p_0 . As described in (Waldvogel and Poulikakos 1997), the dimensionless forms of the mass conservation equation and the R - and Z -momentum equations are:

$$\frac{\partial \bar{P}}{\partial \tau} + \frac{1}{M^2} \left(\frac{1}{R} \frac{\partial}{\partial R} (R\bar{U}) + \frac{\partial \bar{V}}{\partial Z} \right) = 0 \quad (27)$$

$$\frac{\partial \bar{U}}{\partial \tau} - \frac{1}{R} \frac{\partial}{\partial R} (R\bar{\sigma}_{RR}) - \frac{\partial \bar{\sigma}_{RZ}}{\partial Z} + \frac{\bar{\sigma}_{\theta\theta}}{R} = 0 \quad (28)$$

$$\frac{\partial \bar{V}}{\partial \tau} - \frac{1}{R} \frac{\partial}{\partial R} (R\bar{\sigma}_{RZ}) - \frac{\partial \bar{\sigma}_{ZZ}}{\partial Z} - \frac{1}{Fr} = 0 \quad (29)$$

where M and Fr denote the Mach and Froude numbers, respectively. The term $\frac{\partial \bar{P}}{\partial \tau}$ in the mass conservation equation is due to the replacement of the density term by

a pressure term according to the (dimensional) law $\frac{\partial \rho}{\partial t} = \frac{1}{c^2} \frac{\partial p}{\partial t}$ (Batchelor 1967) for compressible fluids, in order to implement the artificial compressibility method (Hirt and Nichols 1980, Kawahara and Hirano 1983). The stress components $\bar{\sigma}_{ij}$ have the usual definition for axisymmetric modeling (Landau and Lifshitz 1959) and have been cast in dimensionless form (Waldvogel and Poulikakos 1997).

The Lagrangian velocities are given by:

$$\bar{U} = \frac{\partial R}{\partial \tau} \tag{30}$$

$$\bar{V} = \frac{\partial Z}{\partial \tau} \tag{31}$$

The initial and boundary conditions have the following form:

$$\bar{U} = 0, \bar{V} = -1, \bar{P} = \frac{4}{We}; \quad \tau = 0 \tag{32}$$

$$\bar{U} = 0, \frac{\partial \bar{V}}{\partial R} = 0; \quad R = 0 \tag{33}$$

$$\bar{U} = \bar{V} = 0, \quad \text{phase change surface} \tag{34}$$

$$\bar{\sigma}_{RR} n_R + \bar{\sigma}_{RZ} n_Z = -2 \frac{\bar{H}}{We} n_R, \quad \text{free surface} \tag{35}$$

$$\bar{\sigma}_{RZ} n_r + \bar{\sigma}_{ZZ} n_z = -2 \frac{\bar{H}}{We} n_z, \quad \text{free surface} \tag{36}$$

The last two boundary conditions above account for the stresses due to the curvature of the free surface, a very important phenomenon in microfluidics. The terms n_R and n_Z are the radial and axial components of the outward unit normal to the surface (see Figure 24), and \bar{H} the dimensionless mean curvature of the free surface. Due to lack of experimental data on dynamic wetting, the wetting force at the dynamic contact angle is neglected through this analysis. This assumption is clearly justified when the impact pressure gradient in the radial direction is high, as well as in substrate melting cases where solidification occurs at the wetting line, as will be shown later. In general, one is justified to neglect wetting if the value of the Weber number based on the contact

line velocity is greater than $O(1)$. The following dimensionless numbers are defined for the fluid dynamics:

$$\text{Reynolds number} \quad Re = \frac{\rho v_0 d_0}{\mu} \quad (37)$$

$$\text{Weber number} \quad We = \frac{\rho v_0^2 d_0}{\sigma} \quad (38)$$

$$\text{Froude number} \quad Fr = \frac{v_0^2}{d_0 g} \quad (39)$$

The fluid dynamics modeling is applied to the entire molten domain. As soon as a substrate element starts to melt, it is added to the domain where the fluid dynamics is calculated.

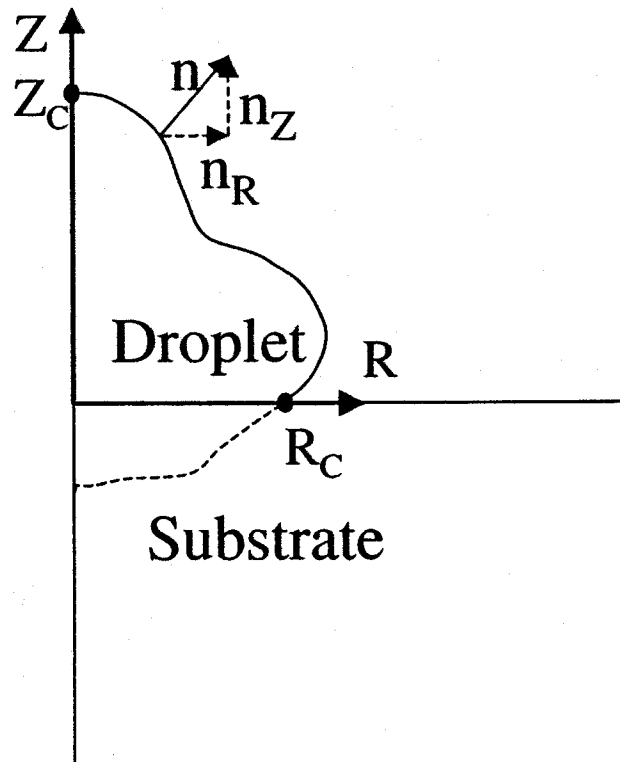


Figure 24: Schematic of the problem of interest showing axisymmetric droplet coordinate definition and melted domain (dashed line).

3.2.2. Heat transfer and Phase change

The energy equation for the droplet and substrate is also cast in Lagrangian form. The dimensionless form of this equation is:

$$C_i \frac{\partial \Theta}{\partial \tau} - \frac{1}{\text{RePr}} \left[\frac{1}{R} \frac{\partial}{\partial R} \left(K_i R \frac{\partial \Theta}{\partial R} \right) + \frac{\partial}{\partial Z} \left(K_i \frac{\partial \Theta}{\partial Z} \right) \right] = 0 \quad (40)$$

The non-dimensionalization of the heat transfer equation was carried out according to the following dimensionless numbers:

$$\text{Pr} = \frac{\mu c_L}{k_L}, C_i = \frac{\rho_i c_i}{\rho_L c_L}, K_i = \frac{k_i}{k_L} \quad (41)$$

The index $i = 1, 2$ or 3 stands for the droplet, the substrate and the interface, respectively. Initial conditions in the droplet, substrate and interface region are:

$$\Theta_1(R, Z, 0) = 1, \Theta_2(R, Z, 0) = 0, \Theta_3(R, Z, 0) = 0, \tau = 0 \quad (42)$$

Radiation heat transfer is neglected from all surfaces, and the substrate is assumed to be large enough so that the natural boundary condition (no normal heat flux) applies along the entire boundary of the computational domain. Accounting for radiation and convection between the droplet and the ambient gas has no effect on the results as shown in a previous investigation (Waldvogel and Poulidakos 1997). For all practical purposes, the cooling occurs through convection in the bulk fluid and conduction to the substrate.

The phase change is modeled according to (Bushko and Grosse 1991, Waldvogel and Poulidakos 1997), where the effect of latent heat release is introduced in the computation by a local increase of the heat capacities. This approach leads to the exact integration of the capacitance terms in the finite element formulation with linear triangular elements, and has shown very accurate energy conservation capabilities (Waldvogel and Poulidakos 1997). It is assumed that the phase change occurs through a sharp boundary, at equilibrium temperature, and that the densities of the solid and liquid material are the same in the fluid dynamics calculation. The Stefan number and superheat parameter SHP are defined as follows:

$$\text{Ste} = \frac{c_L (T_M - T_{2,0})}{L} \quad (43)$$

$$SHP = \frac{T_{1,0} - T_M}{T_M - T_{2,0}} \quad (44)$$

3.2.3. Contact Resistance

During the spreading of a droplet on a surface, the heat transfer at the interface is reduced (due, for example, to roughness, air entrapment or surface oxidation (Wang and Matthys 1996)). This is particularly true before substrate melting and the ensuing merging of the two bodies. Due to lack of experimental data on the transient contact resistance to be inputted to numerical models, this interfacial resistance to heat transfer has been handled macroscopically and empirically by introducing a tunable contact heat transfer coefficient between the drop and the substrate (Wang and Matthys 1996), or by inserting a thin interface of massless elements between the droplet and the substrate with a lower and tunable thermal conductivity (Waldvogel and Poulikakos 1997). In our model, the latter approach has been used as a starting point, and extended in order to allow the heat transfer and fluid computation to be performed during the substrate melting phase in the entire molten domain. To this end, we have added mass to the elements of the thermal interface mentioned above. A low and tunable conductivity was assigned to the elements of the interface. This dimensionless interfacial conductivity K_3 ($K_3 = k_3 k_L^{-1}$) is related through the contact Biot number ($B_i = h_3 k_L^{-1} d_0$) to the interfacial heat transfer coefficient h_3 by the equation

$$K_3 = B_i L_3, \quad (45)$$

where L_3 is the dimensionless interface thickness ($L_3 = l_3 d_0^{-1}$). Our results will be expressed in terms of the contact Biot number, which is the relevant dimensionless number for interfacial conductance (inverse resistance).

To account for the practical disappearance of the contact thermal resistance at a droplet/substrate interface region in which substrate melting occurs (Schmaltz and Amon 1996), the local conductivity of an interface element is increased to the standard conductivity value of the substrate/splat material considered, when all the nodes of this element are above the melting temperature.

3.2.4. Mixing

During the substrate melting process, the melted substrate material participates to the fluid dynamics, which induces a mixing of the droplet and substrate material. In

order to study the evolution of this mixing which can be important to the bonding quality, a mixing indicator ϕ is introduced. This indicator takes the values of 1 for splat material, and 0 for substrate material or interface material. In the absence of a chemical potential driving material diffusion between the substrate and the droplet material, the mixing equation in a Lagrangian framework is expressed as follows

$$\frac{\partial \phi}{\partial \tau} = 0 \quad (46)$$

with the initial condition:

$$\tau=0: \quad \phi(R, Z, 0) = 1, Z > 1, \quad \phi(R, Z, 0) = 0, Z \leq 1 \quad (47)$$

In the presence of a laminar flow exhibiting no chaotic mixing, which is the case in this chapter, the interface between the two bodies remains sharp. The tracking of this interface is performed by setting a specific value ($\phi=0.5$ in the case) to every droplet node that comes in contact with the droplet/substrate interface. Tracking this specific contour value of $\phi=0.5$ yields the location of the boundary between droplet and the substrate material in time.

3.3. Numerical Simulation Procedure

The computational domain was discretized with a mesh of triangular linear elements, and the numerical model was solved using a Galerkin Finite Element Method. A Crank-Nicholson scheme was used for the temporal integration of the energy and mass transfer equation. The fluid particle location and the energy conservation equations were coupled on the basis of a method proposed by Bach and Hassager (1985).

The following summarizes a single time step of computation:

(1) Identify the liquid domain: only the elements where at least one node temperature is lower than the melting temperature are considered for the fluid dynamics calculation.

(2) Impose the fluid dynamics boundary conditions, Eqs. (33) to (36).

(3) Given an initial configuration of fluid particles and flow variables, calculate the new nodal location by numerical integration of Eqs. (30) and (31). The velocities at time τ are used as initial 'guesses' for velocities at time $\tau+\Delta\tau$.

(4) Based on the current nodal locations, calculate velocity and pressure fields at $\tau+\Delta\tau$ by solving the discrete forms of the mass conservation and momentum equations (Eqs. (27) to (29)).

(5) Update the nodal locations by numerical integration of Eqs. (30) and (31) after inserting the velocities at time step τ and $\tau+\Delta\tau$.

(6) Iterate steps (3) and (4) until convergence is reached for the time step. Convergence is assumed when the maximum difference for each fluid particle flow variable was less than 0.1% from one iteration to the next.

(7) Given the temperature field at time τ , solve the energy equation, Eq. (40), to obtain the overall temperature field at time $\tau+\Delta\tau$ in the entire computational domain.

(8) Given the mixing field at time τ , solve the mixing equation, Eq. (46), in the entire computational domain to obtain the mixing field and phase boundary at time $\tau+\Delta\tau$.

Remeshing was performed every time that the element distortion attained a critical value. The element distortion is defined as the ratio of the radius of a circle passing through the three points defining an element, and the radius of a circle that circumscribes an equilateral triangle that has the same area as the element under consideration. The mesh generation was performed with a state of the art, optimized and commercially available mesh generator (Hypermesh, Altair Eng. Inc.), which has proven to be markedly more robust than the meshing generation process used in previous simulations without substrate melting (Waldvogel and Poulikakos 1997). Hypermesh was used in batch mode (Haferl, et al. November 2000) since a typical run involved about sixty complete remeshing. After a new mesh was created, the solution variables were mapped to the new nodes via interpolation of the old mesh. The temperature and mixing variables of the nodes near the mixing front and the phase change front were adjusted after each remeshing in order to conserve accurately the shape of the mixing and phase boundaries, respectively. A detailed study has been performed to determine the temporal and spatial resolution necessary to obtain time step and grid independence, the main results of which are presented in the next section. A typical run required 22 CPU hours to complete on a PC with a 500 MHz Pentium III Processor. The pressure of the substrate elements that were introduced in the fluid dynamics calculation during the melting process was initialized to the same value as the initial drop pressure ($\bar{P} = \frac{4}{We}$). No differences in the heat transfer solution and fluid dynamics were observed during test simulations with different initial pressures for the substrate elements ($\bar{P} = 0, \bar{P} = \frac{40}{We}$).

3.4. Results and Discussion

3.4.1. Baseline Case and Parametric Variations

The main goal of the runs performed is the investigation of substrate melting in the case of molten microdroplet impact of eutectic Pb-Sn solder, as described in the introduction. In addition to featuring a sharp melting interface, this material has a relatively low melting point that will facilitate future experiments, and it is the material of choice in electronics soldering applications where larger solder amounts are deposited in one location by pileup or combination of a desired number of microdroplets (Hayes and Wallace 1998, Hayes, et al. 1992, Waldvogel, et al. 1998). A first series of runs was performed in order to investigate the sensitivity of substrate melting to the thermal parameters (SHP, Bi). The baseline case corresponds to the impact at 1.5 ms^{-1} of an 80-micron diameter solder droplet at a temperature of 210°C on a solder substrate at a temperature of 182°C (1K below the equilibrium melting temperature). These conditions are typical in solder jetting applications (Hayes and Wallace 1998, Waldvogel and Poulikakos 1997). The interfacial heat transfer coefficient was set to the relatively high value of $10^7 \text{ Wm}^{-2}\text{K}^{-1}$. The thickness l_3 of the heat transfer interface was one percent of the drop diameter, i.e. 0.8 microns. The choice of an initial substrate temperature near the melting point corresponds also to conditions encountered in actual applications of micromanufacturing (Orme, et al. 2000), where the frequency of droplet deposition is high in order to minimize the manufacturing time. These values were nondimensionalized according to the following thermophysical properties for Pb-Sn eutectic solder: $\sigma=0.345 \text{ Jm}^{-2}$, $\mu=0.00262 \text{ Pas}$, $\rho_L=8218 \text{ kgm}^{-3}$, $\rho_S=8420 \text{ kgm}^{-3}$, $c_L=238 \text{ J kg}^{-1} \text{ K}^{-1}$, $c_S=176 \text{ J kg}^{-1} \text{ K}^{-1}$, $k_L=25 \text{ Wm}^{-1}\text{K}^{-1}$, $k_S=48 \text{ Wm}^{-1}\text{K}^{-1}$, $L=42000 \text{ J/kg}$ and $T_M=183^\circ\text{C}$. The thermal dimensionless groups, i.e. superheat parameter SHP, Stefan and the Biot numbers, assume respectively the values 9.64×10^{-1} , 5.7×10^{-3} and 32. The Weber and Reynolds numbers are 4.3 and 376, respectively. The substrate is flat with radial and axial dimensions eight times larger than the diameter of the droplet, in order to simulate the impact on a substrate much larger than the droplet. The chosen criterion for determining the substrate size was that the system constituted by the droplet and substrate exhibit after heat transfer and solidification a mean temperature increase smaller than 10% of the difference between the initial substrate temperature $T_{2,0}$ and the melting temperature T_M . Around the baseline case, $T_{2,0}$, h_3 and v_0 have been varied individually in order to investigate the importance on the substrate melting of SHP (0.9, 0.931 and 0.9643), Bi (0.032, 0.32, 3.2, 32 and ∞) and impact velocity v_0 (1 to 2 m s^{-1}), respectively. In order to compare the numerical results with existing experiments for larger droplets (Zarzalejo, et al. 1999) –no experiments could be found for microdroplets– a

simulation of substrate melting with mm-size steel droplets has been performed and the results of the comparison as well as interesting related findings will also be reported later in this chapter.

3.4.2. Mesh Size and Time Step Independence

A fact of central importance to every numerical solution is the independence of the reported results on the grid size and time step. In this subsection we discuss the independence of the present results for droplet impact fluid dynamics as well as substrate melting on the temporal and spatial discretization. Our baseline case, described earlier, was selected for it is a demanding case featuring a large amount of substrate melting and large temperature gradients in the presence of which energy must be conserved.

Figure 25 shows a detail of the mesh used for the baseline case, as well as a detail of the interface elements. It has a typical number of 2654 nodes and 5113 elements, with 664 nodes and 1234 elements in the droplet. In order to limit the thermal energy losses by numerical diffusion and to keep the calculation time reasonable, the region of the mesh shown in Figure 25 (where the largest temperature gradients appear) was meshed with a high and constant density of elements, while the mesh outside the shown region was gradually coarser. This 'baseline' mesh was compared to a coarser and a finer mesh. The coarser mesh has a lower density of elements in the region of high temperature gradients. It has 2076 nodes and 3978 elements, with 503 nodes and 924 elements in the droplet. The finer mesh has a higher density in the region of high temperature gradients, and this fine mesh region was also extended axially and radially from respectively -1 to -2 , and 1 to 2 . The finer mesh has about four times the elements of the baseline mesh (9905 nodes and 19517 elements, with 913 nodes and 1717 elements in the droplet). We use for the baseline case a time step of $d\tau=5\times 10^{-4}$, as used for simulations of a comparable problem without substrate melting considerations (Waldvogel and Poulikakos 1997). Results with this time step were compared to results with one smaller ($d\tau=2.5\times 10^{-4}$) and one larger ($d\tau=1.0\times 10^{-3}$) time step in order to test the effect of the temporal discretization.

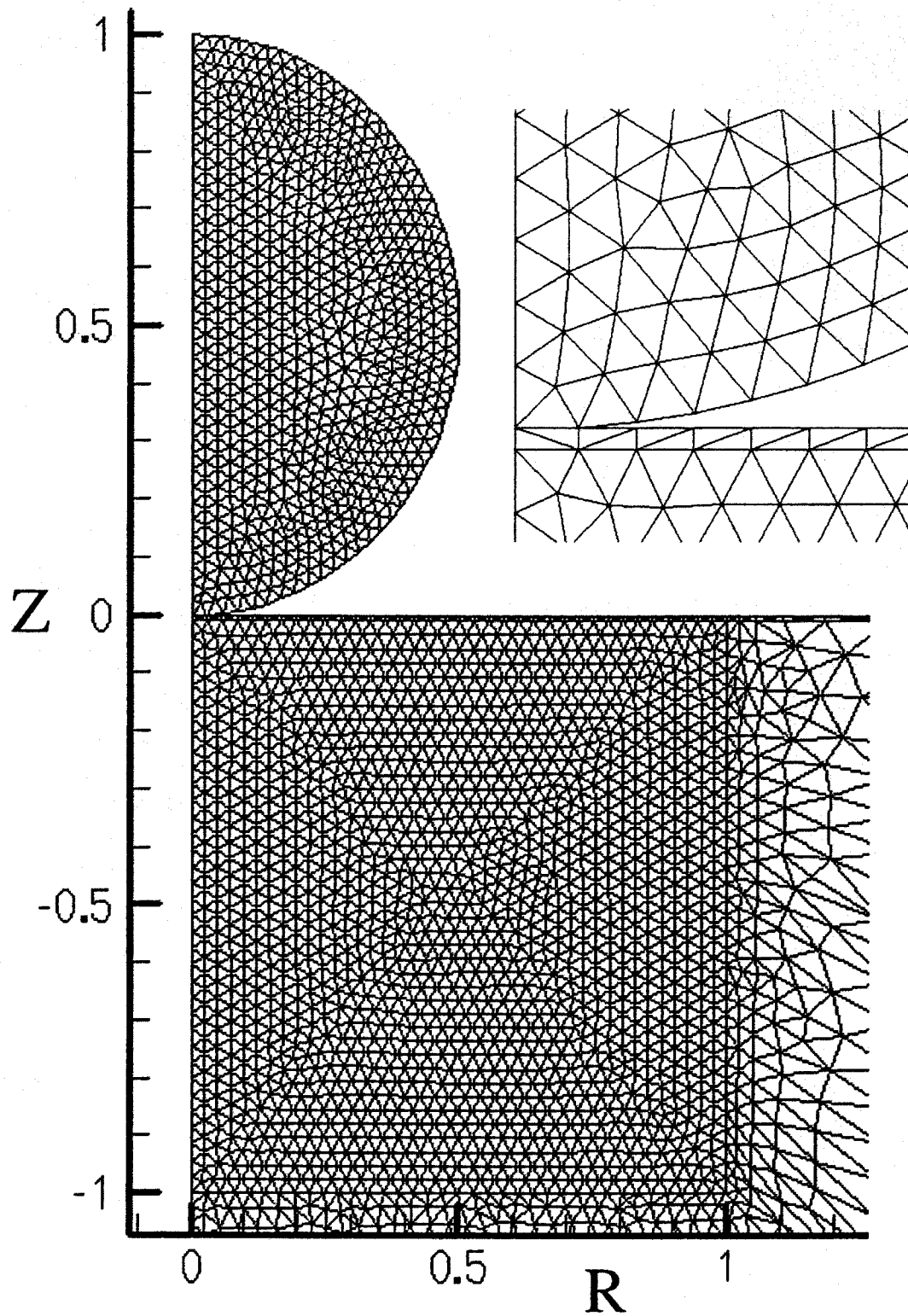


Figure 25: Details of a typical mesh used. The first layer of the substrate has a dimensionless thickness of 0.01 and its conductivity can be tuned for simulating interfacial resistance to heat transfer.

Figure 26 (a) shows the effects of the temporal and spatial discretization on the fluid dynamics, exemplified by the evolution of Z_C , the Z-axis contact point with the free surface of the droplet, as a function of time. A marked and undesirable phase lag in the position of Z_C appears in the simulation with the larger time step ($d\tau=1.0\times 10^{-3}$), while the four other simulations show a good agreement. Figure 26 (b) shows the temporal evolution of the melted volume V_M (defined in the next section). It appears that the simulation with the small time step ($d\tau=2.5\times 10^{-4}$) is not adequate for predicting the remelted volume near its maximum. This result is likely due to the accumulation of numerical inaccuracies and round off errors during the larger number of calculation steps, leading to thermal energy losses. The simulation with a coarse mesh also underestimates the amount of substrate melting. We conclude from both investigations that only two configurations are suitable for the calculation, namely the baseline case ($d\tau=5\times 10^{-4}$, baseline mesh) and the fine mesh case ($d\tau=5\times 10^{-4}$, fine mesh). Since a run with the baseline case takes about 22 hours on a Windows NT 500 MHz Pentium III workstation, a run with the fine mesh case, more than 100 hours on the same machine, the baseline case is chosen for our calculations, after verifying that the total amount of thermal energy losses at the end of the computation are acceptable (smaller than 4%).

3.4.3. General Description of the Substrate melting Process

Figure 27 shows the droplet shape and phase change boundary (separating the liquid and solid phases) at successive instants of the substrate melting process, for the baseline case. One observes that substrate melting occurs already in the early stages of the spreading ($\tau=0.05$) and that the melting process extends in the radial direction simultaneously with the droplet. No effects of interfacial contact resistance are visible, which would delay the melting with respect to the spreading advance. During the spreading of the droplet, a maximum substrate melting depth of about 10% of the initial droplet diameter is attained along the Z-axis, at the time $\tau=0.05$. The simultaneous spreading and melting indicate that in the parametric domain of interest of the present study the time scales of the fluid dynamics and the substrate melting phenomenon are of the same order, and that any model uncoupling the fluid dynamic calculation from the heat transfer and solidification process would probably oversimplify the problem. Also, the motion and shape of the phase change boundary, crossing the R-axis at time 1.0 shows the highly 2D aspects of the substrate melting and re-solidification phenomenon. For $\tau>1.0$, the phase front progresses upward and the coupling between freezing and oscillations produces ripples on the splat surface, a mechanism found and explained in the numerical work of Waldvogel and Poulikakos (1997) and verified experimentally by Attinger et al. (2000b).

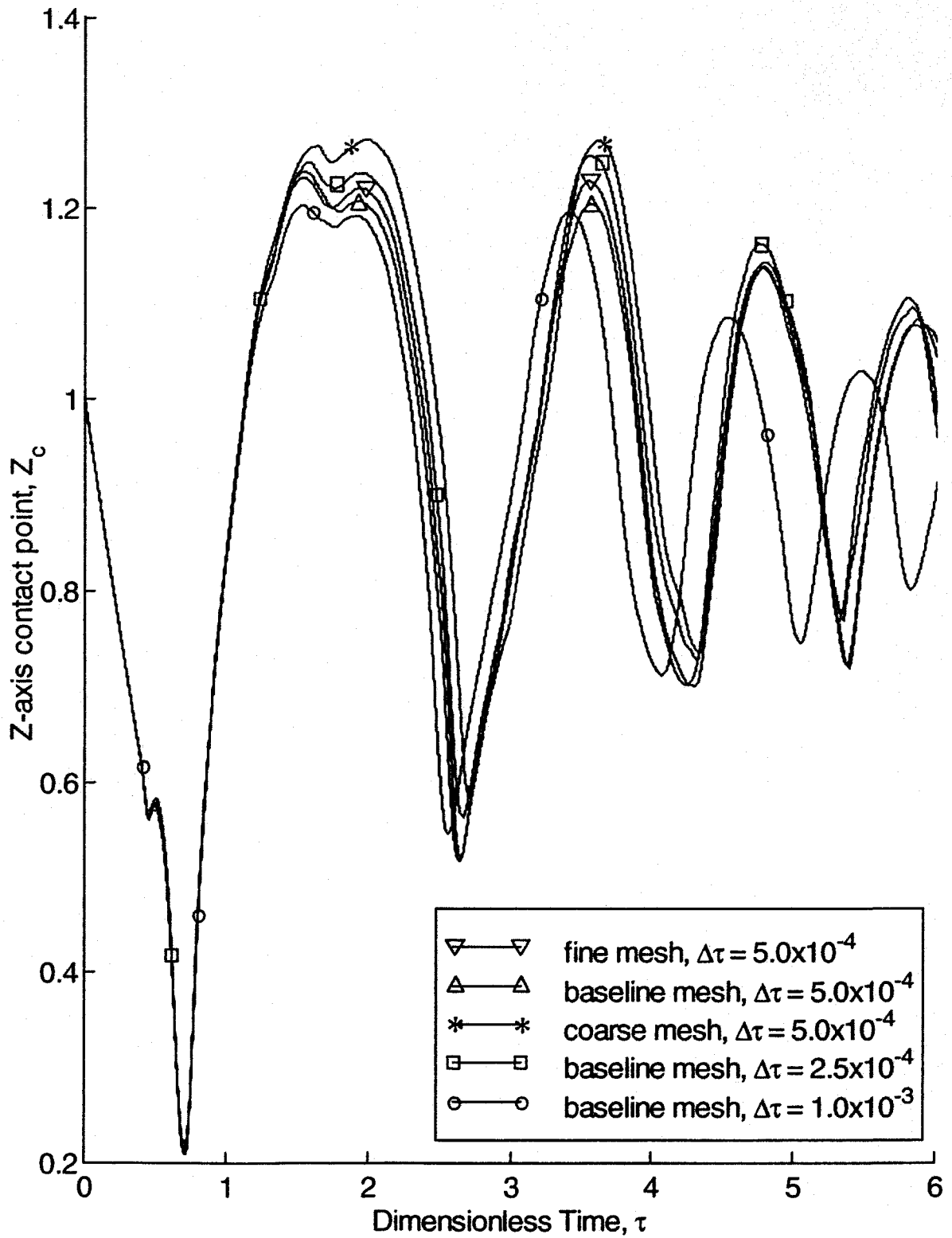


Figure 26(a): Temporal evolution of the Z-axis contact point for the baseline case, for different temporal and spatial discretizations.

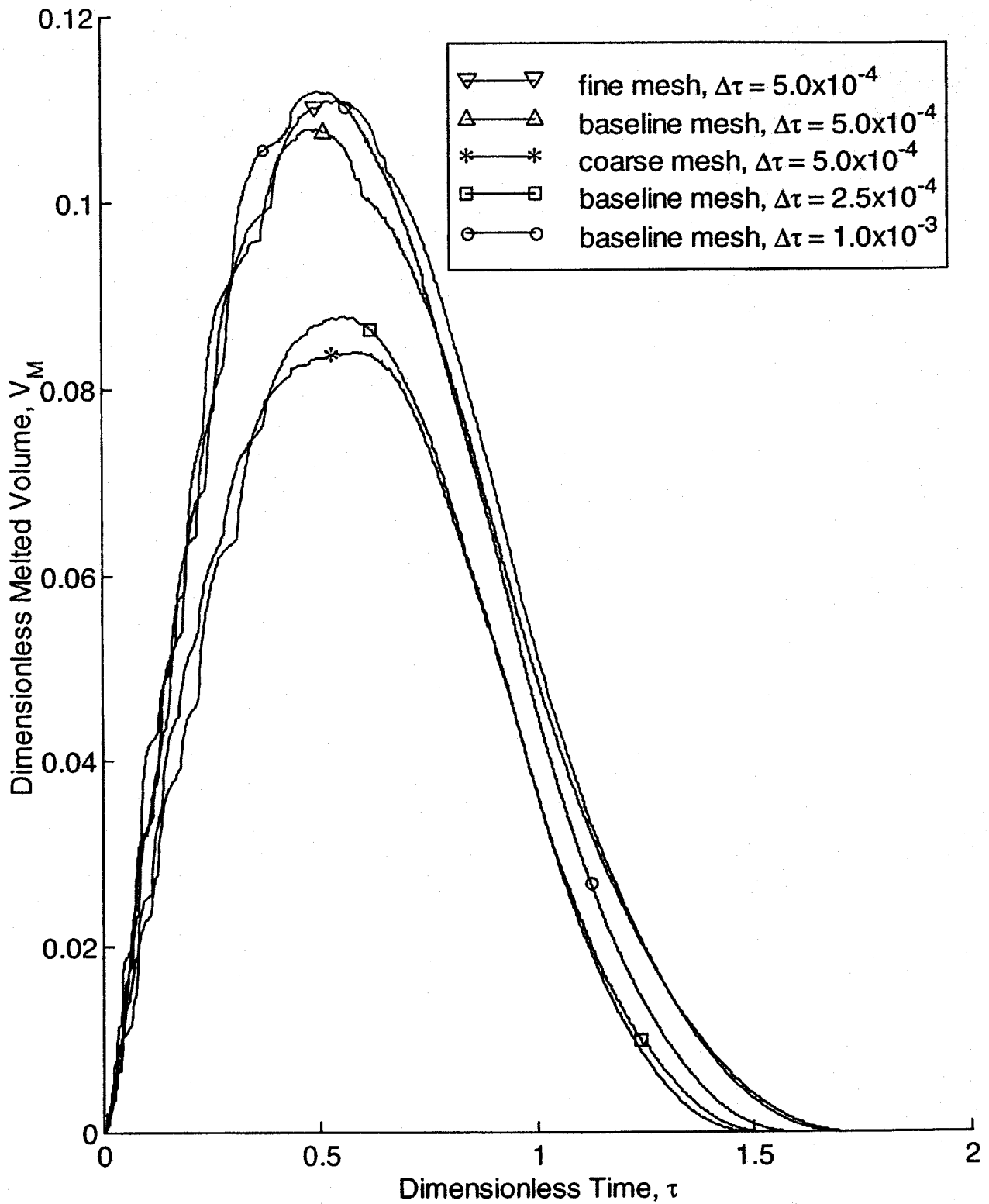


Figure 26(b) Temporal evolution of the melted volume V_M for the baseline case, for different temporal and spatial discretizations.

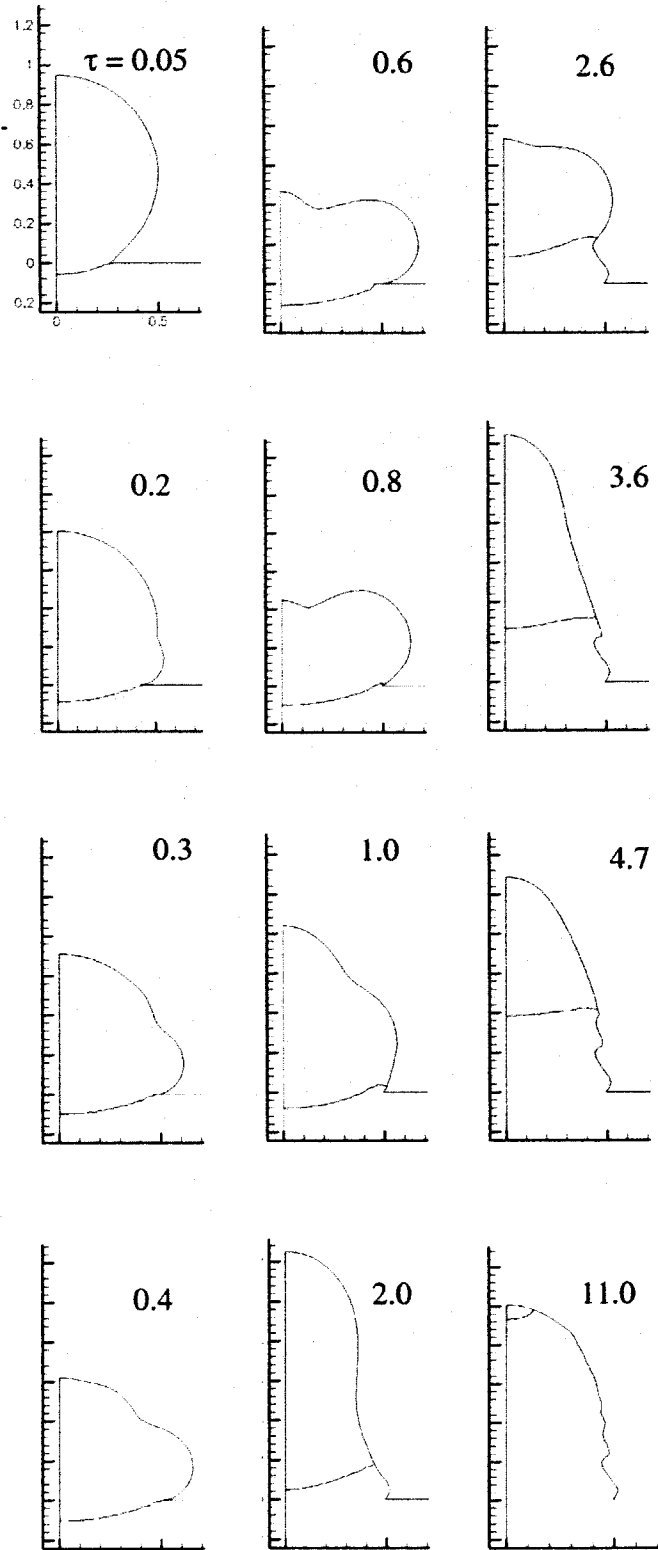


Figure 27: Droplet shape and phase change location as a function of the dimensionless time for the baseline case.

3.4.4. Quantitative Characterization of Substrate Melting

In order to discuss features of the substrate melting phenomenon, we quantify this melting in terms of the dimensionless melted volume V_M , defined as the amount of liquid material below the $Z=0$ boundary. This parameter has been preferred to the dimensionless volume of liquid in the entire computational domain V_L , for the following reason: a value of V_M larger than zero means unequivocally that some substrate material has melted while a value of V_L lower than unity does not mean that all the material below the $Z=0$ line has solidified, since our results show (Figure 27, $\tau=1.0$) that solidification can start at the periphery of the droplet while the zone near the Z -axis still experiences a significant amount of melting. It is also worth noting that we write ‘material below the $Z=0$ boundary’, rather than ‘substrate material’, since there is a significant mixing between the droplet and the substrate material, as will be shown in the next section.

Figure 28 shows the temporal evolution of V_M for three values of superheat (SHP). As expected and shown in previous studies (Wang, et al. 1998), the maximum melted volume increases with SHP. It also appears that the time when this maximum is reached increases with SHP, which can be explained by the fact that the substrate melting depth increases with the SHP, the thermal diffusivity being the same for the three cases. The time for reaching the maximum substrate melting is smaller than the time between the maximum substrate melting and the instant where the entire material below $Z=0$ is solid. This is different from the symmetry of the amount of substrate melting versus time curves presented in previous 1D simulations by Wang et al. (1998). The dependence of the total time from impact to complete solidification and of the melted volume of the substrate material on the superheat parameter SHP is shown in Figure 29 for $Bi = 0.32$. Although the melted volume increases monotonically with increasing the superheat parameter, it appears that the time τ_s from impact to complete solidification varies in a nonmonotonic way for SHP larger than 0.4: it increases markedly until a threshold value of SHP (0.95) is reached, decreases then drastically ($SHP = 0.9643$) and starts increasing again ($0.9643 \geq SHP \leq 0.98$). The explanation for this counterintuitive behavior is related to the substrate melting phenomenon. For SHP up to a threshold value (here 0.95), melting is confined in the interfacial layer, whose low thermal conductivity value is conserved through the entire process, as assumed by our numerical modeling. Hence, it takes more time to remove the higher energy content of the droplet corresponding to the increasing values of SHP. Increasing SHP above the threshold value induces complete melting of the interfacial layer and a corresponding practical disappearance of the thermal resistance between the splat and the substrate. The drastic

increase of the values of V_M indicates the participation of the substrate material below the interface to the melting process. A direct result of the complete melting of the interfacial layer is a larger heat flux between the splat and the substrate and consequently a reduction of the solidification time. The increase of the total solidification time with SHP ($0.9643 \geq \text{SHP} \leq 0.98$) reflects the fact that the initial temperature difference between droplet and substrate is reduced, yielding a reduced cooling rate. Note that the local minimum of the solidification time for low SHP values ($0.1 < \text{SHP} < 0.4$) is caused by the shape of the droplet, which in the case of the local minimum solidification time features a narrow cross-section at some height (not shown here for brevity) hindering (bottlenecking) the heat transfer to the substrate. This has been previously observed, without remelting considerations, by Xiong et al. (1998).

The strong influence of the impact velocity v_0 on the amount of melted volume is shown in Figure 30. The velocities ranging from 1 to 2 ms^{-1} correspond to Reynolds and Weber numbers in the interval (250.6; 501.3), respectively (1.903; 7.61). All the other parameters have been kept constant as in the baseline case. The amount of substrate melting increases clearly with the impact velocity: doubling v_0 increases the amount of substrate melting by about 60%. This is a clear sign of the important role of the fluid dynamics on the substrate melting process. Considering the complex flow pattern in the droplet (to be discussed later in this section), it appears that this can only be studied accurately with a modeling involving consideration of the complex fluid dynamics and free surface dynamics of droplet impact. Similarly with Figure 28, it appears also that the time where the maximum substrate melting is reached increases with the melted volume.

The influence of the interfacial heat transfer, indicated by the Biot number, on the amount of substrate melting V_M is shown in Figure 31. It appears that the substrate remelts in a comparable way for every Biot number larger than a threshold value ($\text{Bi} = 0.32$). This is related to the feature of the interfacial heat transfer model used in this study, where a low and specific heat transfer conductivity at the interface is only assumed as long as no melting has occurred. Any simulation with a Biot number markedly larger than a threshold value, with the melting boundary advancing simultaneously with the contact line (as in Figure 27), will therefore show qualitatively similar behavior. At the threshold value ($\text{Bi} = 0.32$), the initiation of substrate melting is delayed somewhat compared to cases with markedly higher values of Bi , which can be explained by the fact that the interface layer resists a longer time (up to about $\tau = 0.25$) before melting. It is interesting to note that the maximum amount of substrate melting at this threshold Biot number value is comparable to the maximum amount of substrate melting at larger Biot numbers. When the Biot number is lowered by an order of magnitude again ($\text{Bi} = 0.032$), V_M exhibits much lower values and assumes a different shape, signifying that the substrate melting is confined to the interfacial layer, whose low

thermal conductivity value is conserved through the entire process (no substrate melting takes place below the interfacial layer). It is worth noting that Kang et al. (1995) have shown that assuming an interfacial contact heat transfer coefficient h_3 of $10^6 \text{ Wm}^{-2}\text{K}^{-1}$ provided a reasonable agreement between a model of 1D freezing/melting in the droplet combined with 2D conduction in the substrate, and experiments with mm-size eutectic tin-lead solder droplets, but only in the region near the center of symmetry where the 1D hypothesis is more likely to be valid. Assuming the same contact heat transfer coefficient for the microdroplet considered here would mean a Biot number of 3.2, larger than the threshold Biot number mentioned above. In this case, the behavior is expected to be similar to that of an infinite Biot number (no contact resistance).

Key aspects of the above effects are summarized in a substrate melting “design” graph, shown in Figure 32. This graph shows the influence of the impact velocity v_0 and the superheat parameter SHP on the melted volume of substrate material V_M , assuming an infinite Biot number according to the above discussion. A series of 25 simulations has been performed (5 values of SHP and 5 values of v_0 , corresponding to the legend and the labeling of the X-axis. Figure 32 shows first a dependence of the melted volume on the SHP (compare with Figure 28), which allows controlling V_M in the range of one to more than ten percent in both cases. The general increase of the amount of substrate melting with the impact velocity demonstrates the importance of the fluid dynamics in particular for high superheat values. More details about the coupling between the fluid dynamics and the heat transfer are provided in the next section.

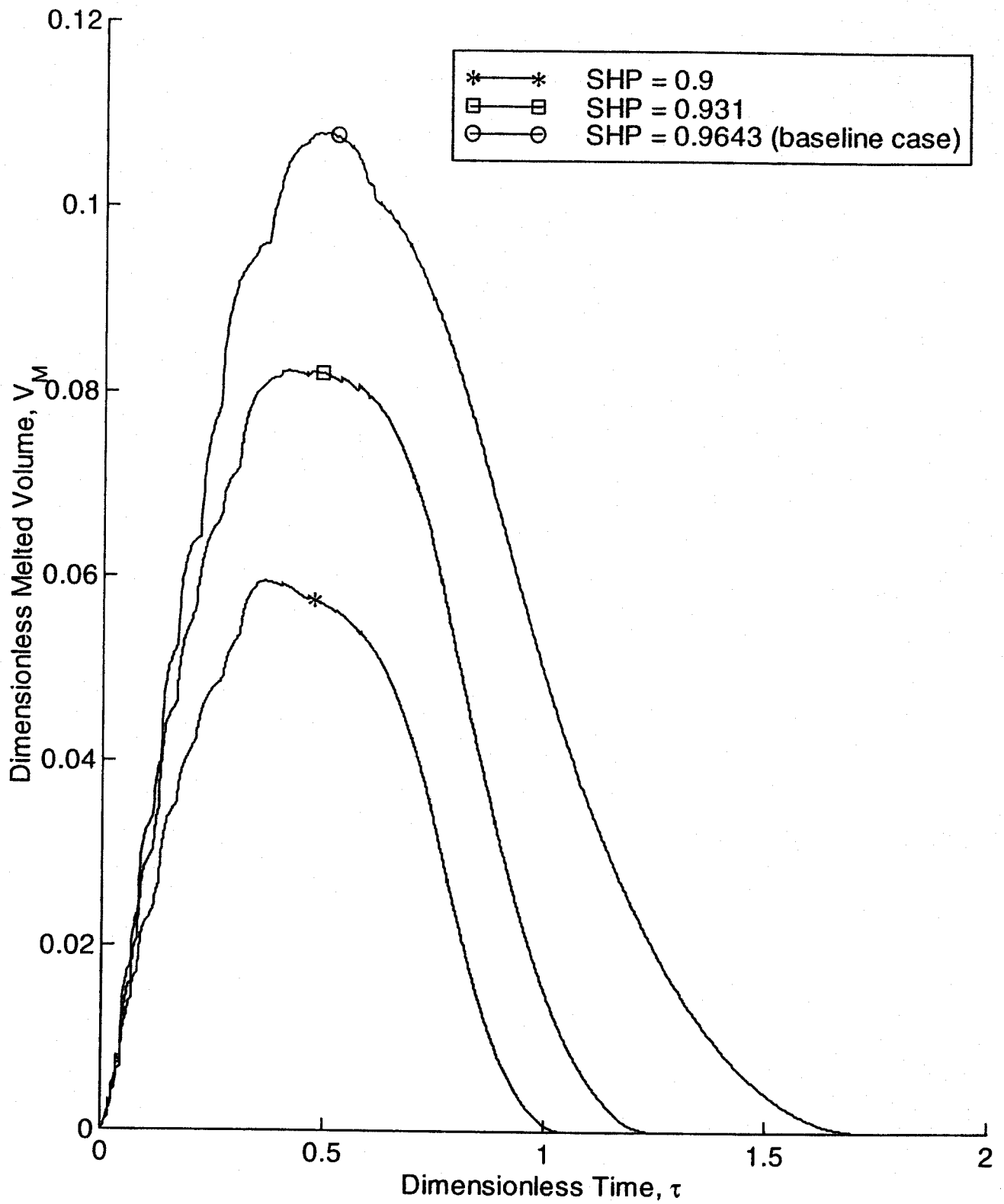


Figure 28: Temporal evolution of the melted volume V_M for different values of the superheat parameter SHP, corresponding to initial substrate temperatures of 180, 181 and 182°C.

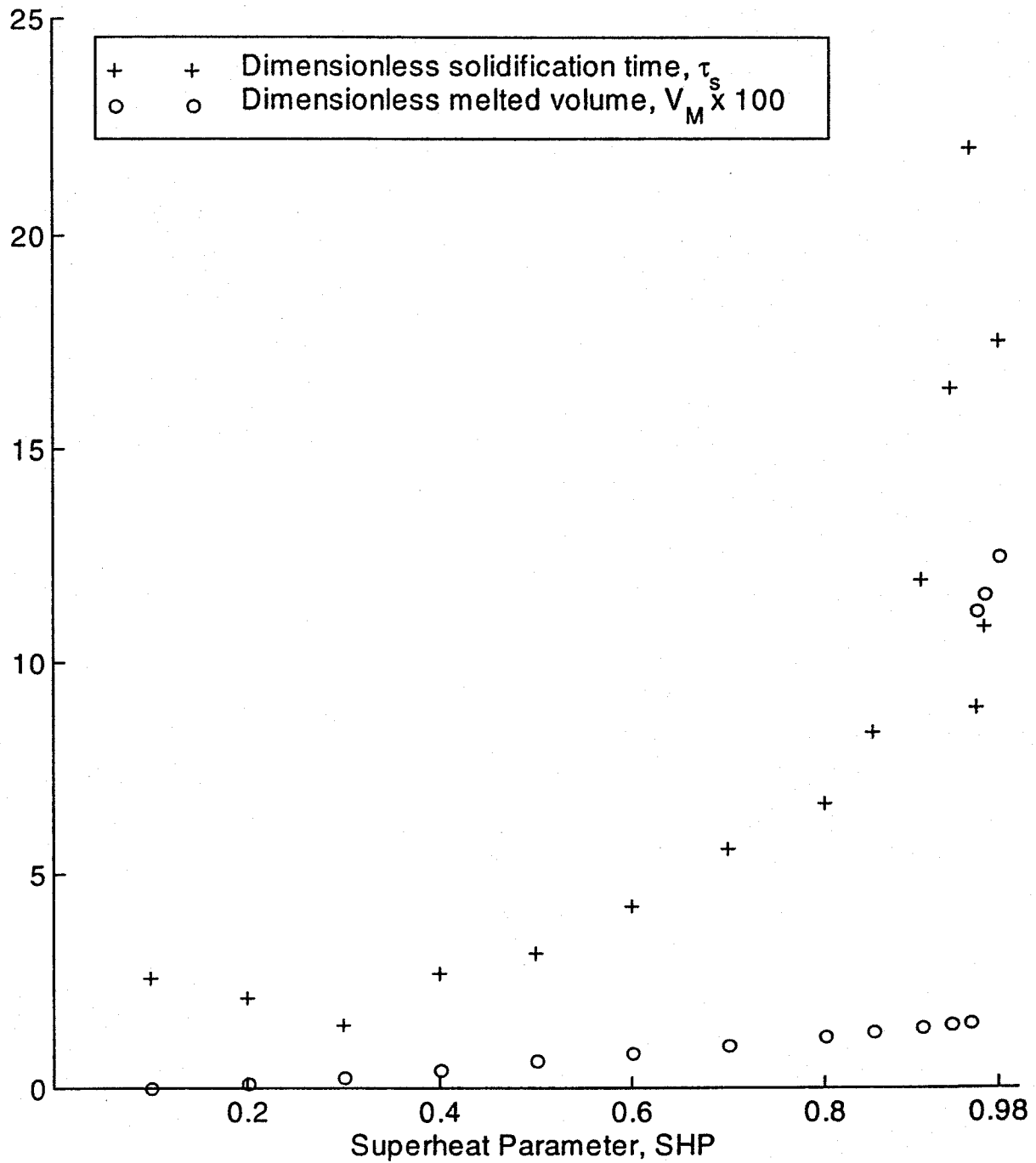


Figure 29: Time from impact to complete solidification and melted volume for different values of superheat parameter SHP in case of $Bi=0.32$.

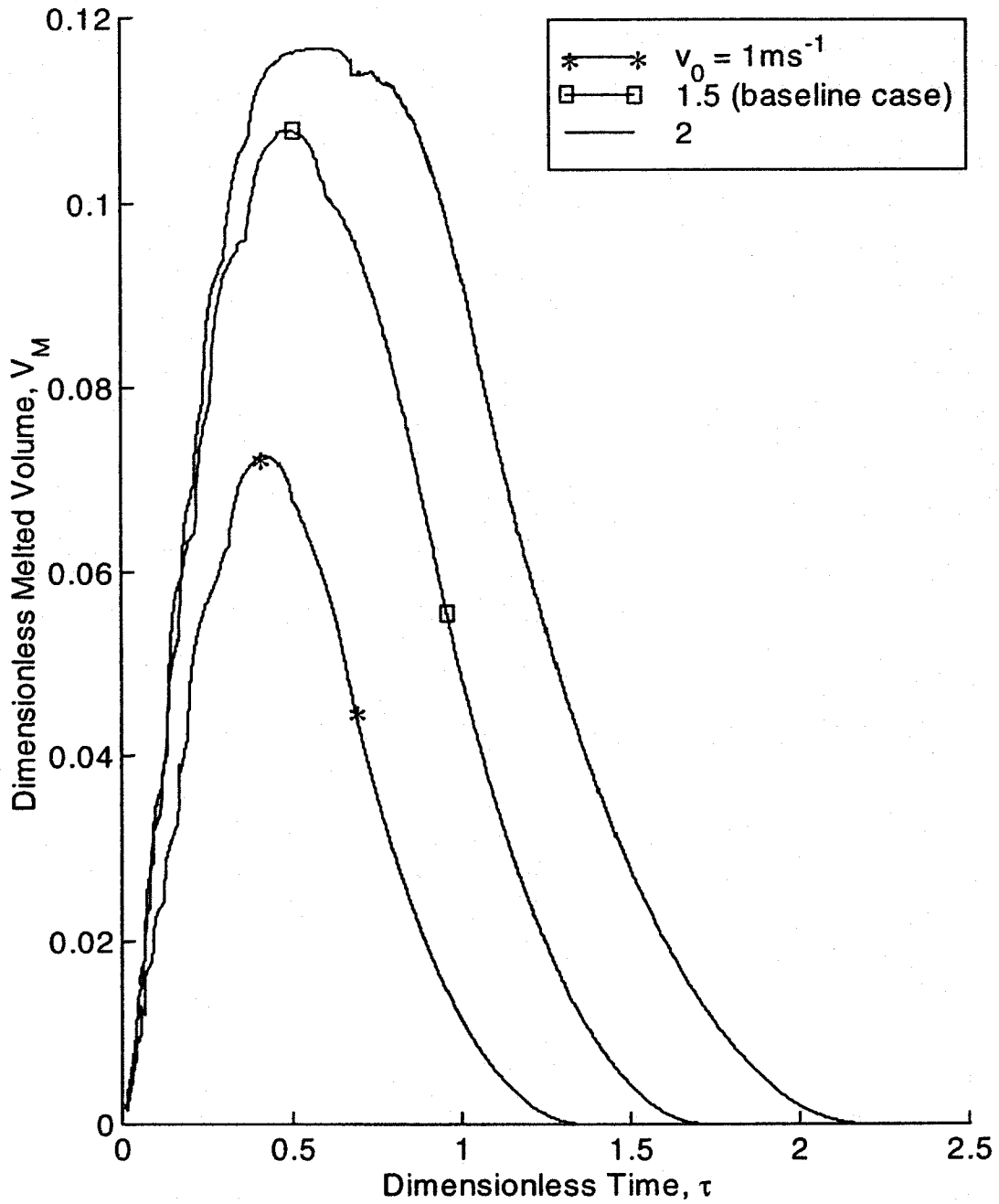


Figure 30: Temporal evolution of the melted volume V_M for different impact velocities. The velocities ranging from 1 to 2 ms^{-1} correspond to Reynolds and Weber numbers in the interval (50.6; 501.3), respectively (1.903; 7.61).

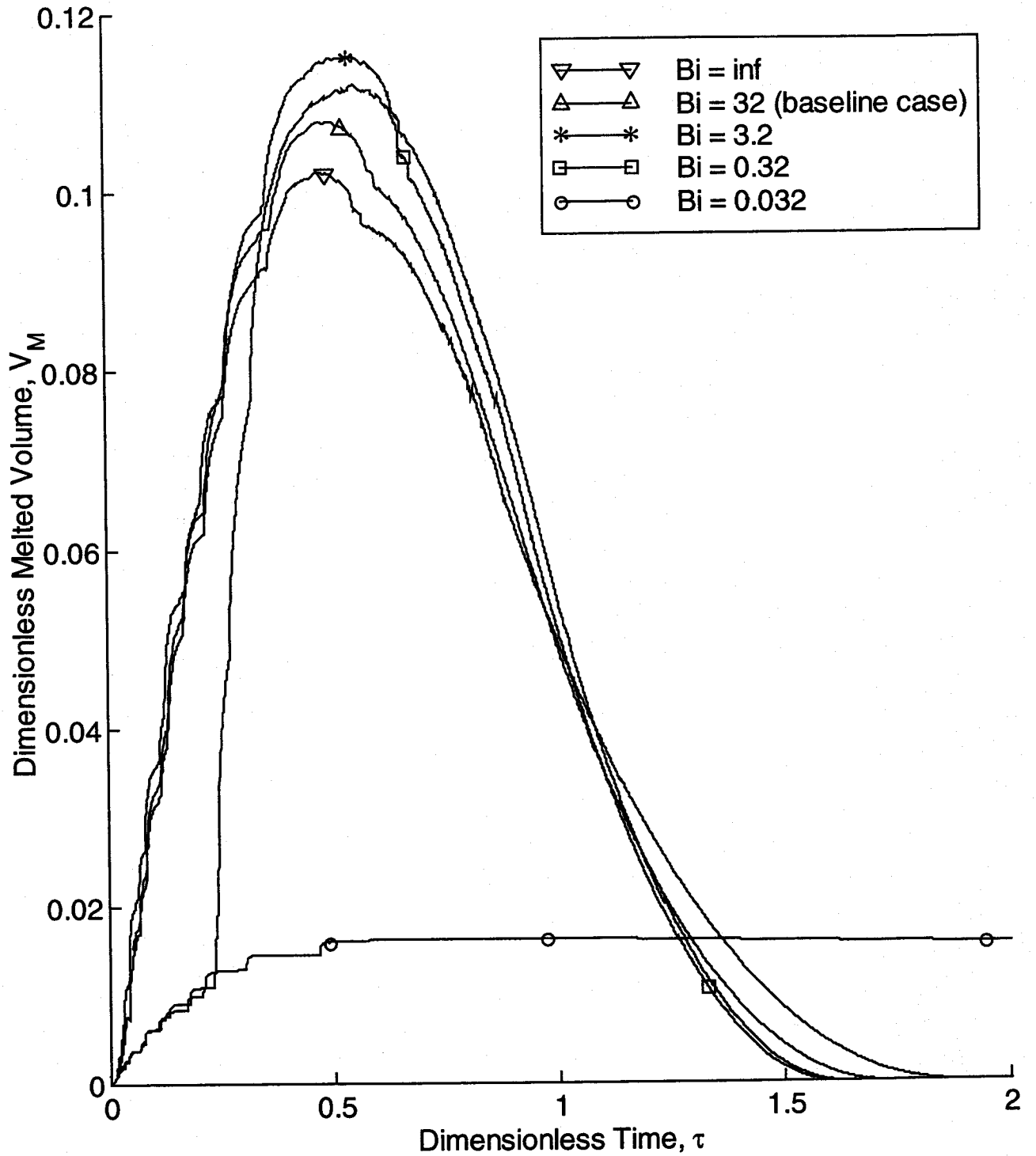


Figure 31: Temporal evolution of the melted volume V_M for different values of the Biot number. The case with an infinite Biot number is the case without thermal contact resistance between the splat and the substrate, and the four subsequent cases correspond to interfacial heat transfer coefficient values of 10^7 , 10^6 , 10^5 and $10^4 \text{ Wm}^{-2}\text{K}^{-1}$.

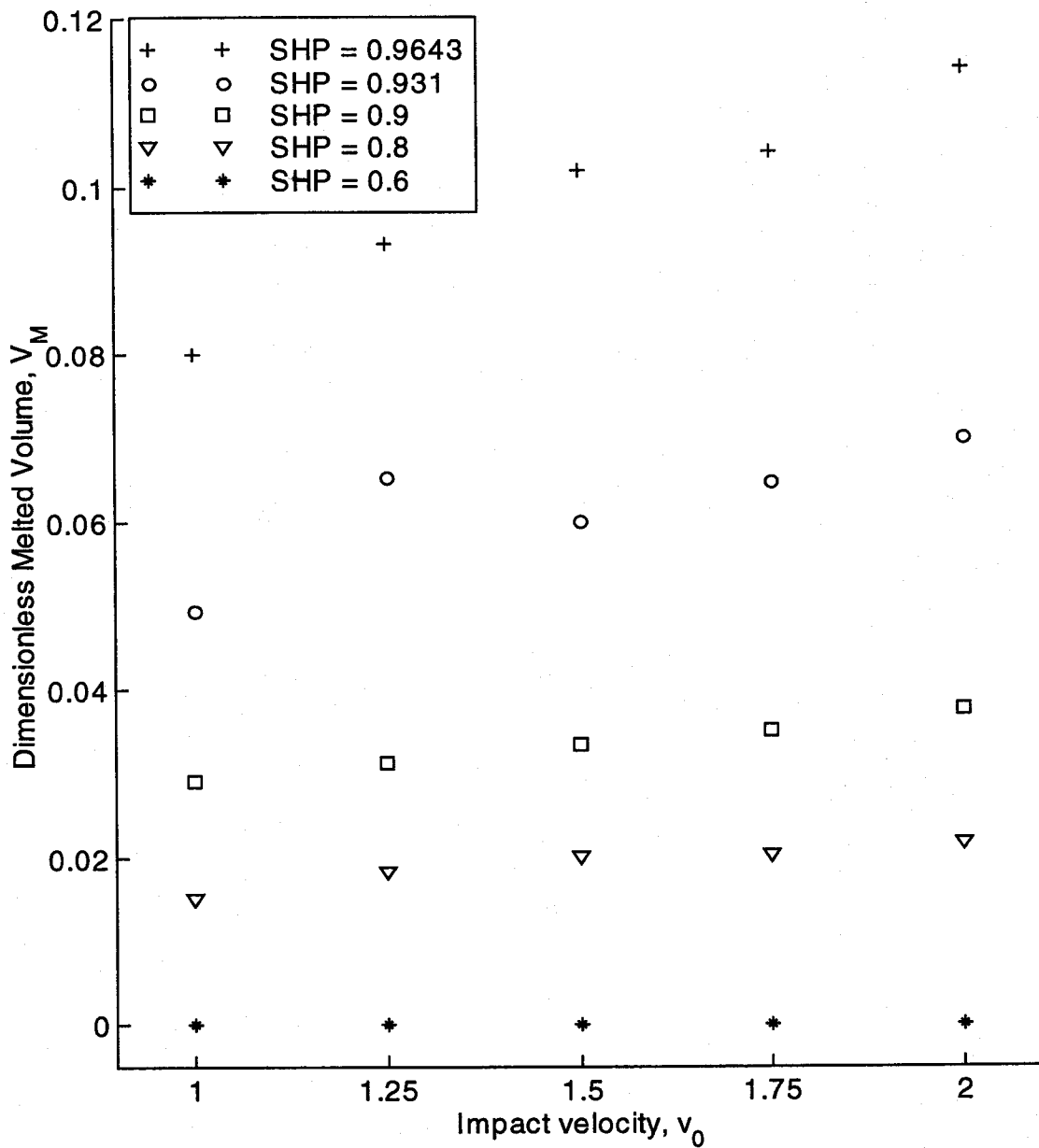


Figure 32: Maximum melted volume V_M as a function of the impact velocity for five different superheat parameter SHP in case of an infinite Biot number.

3.4.5. Considerations of the Mixing between Droplet and Substrate

Mixing between the droplet and the substrate material has never been considered in substrate melting treatment up to now (to the best of our knowledge). Investigation of this phenomenon requires the consideration of the complex fluid dynamics in the entire time-dependent molten domain. All existing substrate melting studies that we are aware of either assume that the melted substrate material does not experience any marked motion, or do not investigate the details of the motion for simplicity. The present study shows a significant and complex mixing process between the droplet and substrate material. Figure 33 provides an insight into the mechanisms governing the mixing, identifying the time history of the boundary between the substrate and droplet material. Contrary to the phase change (see Figure 27), the mixing is relatively moderate during the first phase of the spreading ($\tau < 0.8$), while a more significant amount of material is exchanged during the subsequent recoiling phase (0.8 to 2.0). The freezing process then arrests the final shape of the above-mentioned boundary. The shape of the interface between substrate and droplet material shows that substrate material has been transported in the droplet in regions near the Z-axis ($R < 0.2$) and that droplet material has been transported in the substrate in peripheral region ($R \geq 0.2$). Two mechanisms have been identified that contribute to this mixing process. First, during the spreading and simultaneous substrate melting, a donut-shaped shear-induced vortex is created in the melted substrate material by the radially moving droplet fluid. The corresponding streamlines are shown in detail (a) of Figure 33. This vortex is important to the material mixing since it lifts up substrate material from the substrate in the droplet. The mixing is albeit weak since the large radial pressure gradient that drives the droplet flow along the substrate reduces the vertical spreading of the vortex. When recoiling occurs, the vortex breaks down, giving place to an upward flow pattern (detail (b) in Fig. 10), which causes most of the mixing. Obviously, the above described complex substrate melting phenomenon caused by the impact of a warm microdroplet differs markedly from the simple ‘first-level’ representation of a an amount of hot material suddenly placed in contact with a substrate that melts without exhibiting any significant internal fluid dynamics (Kang, et al. 1995, Rangel and Bian 1997, Wang, et al. 1998, Zarzalejo, et al. 1999). Such mixing considerations are important for modeling the interfacial heat transfer coefficient at the interface between the substrate and the drop. We have shown that the initial interface at $Z=0$ is displaced and distorted during remelting. It is also worth mentioning that tracking of this mixing can be important in the case of heterogeneous substrate melting (the drop and the substrate are of dissimilar materials), not treated in the present study. In this case, the mixing fractions of both materials need to be determined over the entire computational domain in order to modify the thermal and fluid properties accordingly.

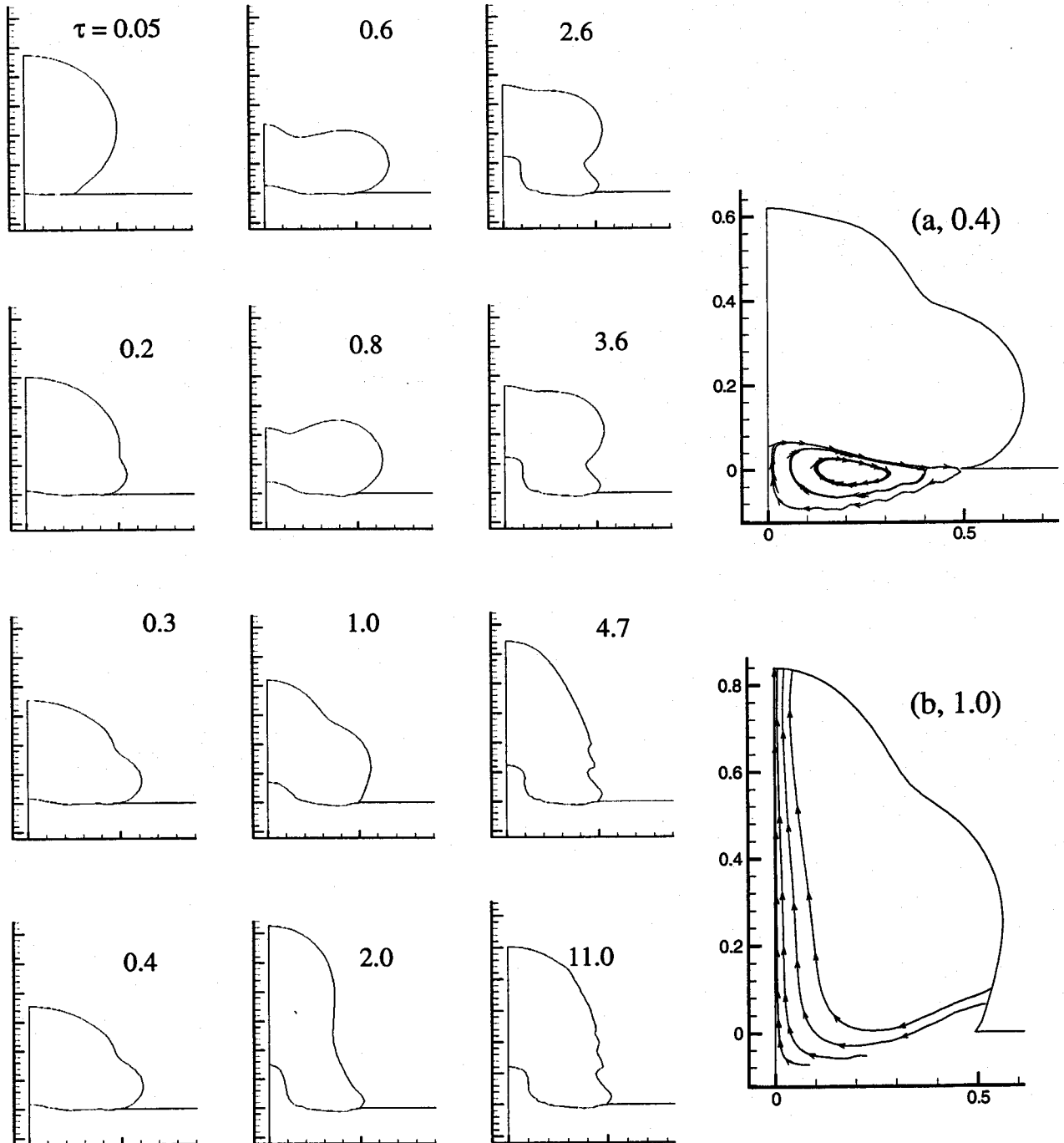


Figure 33: Droplet shape and interface between the drop and substrate material as a function of the dimensionless time for the baseline case. Details (a) and (b) show the instantaneous flow pathlines corresponding to $\tau=0.4$ and 1.0.

3.4.6. Comparison with Experiments for Larger Droplets

In substrate melting induced by microdroplets, the above study has shown that the complex coupling between fluid dynamics and heat transfer needs to be considered in its entirety, as exemplified by the dependence of the amount of substrate melting on the initial impact velocity and superheat, or by the mixing process.

Is the consideration of this coupling also important in case of substrate melting involving larger, mm size droplets? Or is it possible to uncouple the fluid dynamics from the heat transfer, with the assumption that the fluid dynamics occurs first, and only then heat transfer to the substrate? This widely used assumption (Bennett and Poulikakos 1994, Kang, et al. 1994, Madejski 1983, Madejski 1976, Mcpherson 1980) has been adopted to some extent in the work of Zarzalejo et al. (1999), one of the more complete conduction-based models, where these authors compare numerical modeling with substrate melting experiments. Their findings are shown in Figure 34(a-b), which is transferred here from the above-mentioned paper to illustrate the discussion. They simulated the experimental shape of the maximum depth of the phase change boundary (the darker line separating the portion of substrate material that has melted from that which has not) with a numerical model where the calculation domain experienced no deformation and no fluid dynamics, the droplet shape being identical to the final solidified shape of an experiment, during the entire conduction computation. They obtained a relatively good agreement between experiments and simulation (at least for the substrate melting depth along the Z-axis), but this agreement was only reached after increasing in an ad-hoc manner –by a factor five– the thermal conductivity in their diffusion heat transfer model, in order to account for convection. In other words the splat thermal conductivity was selected as the one that gives good agreement with the experiments. While this approach can be deemed as reasonable for rough estimates, in case where no fluid dynamics modeling is performed, it has clearly no predictive power, since convection is accounted for a-posteriori and in terms of an estimate that yields some agreement with previously performed experiments.

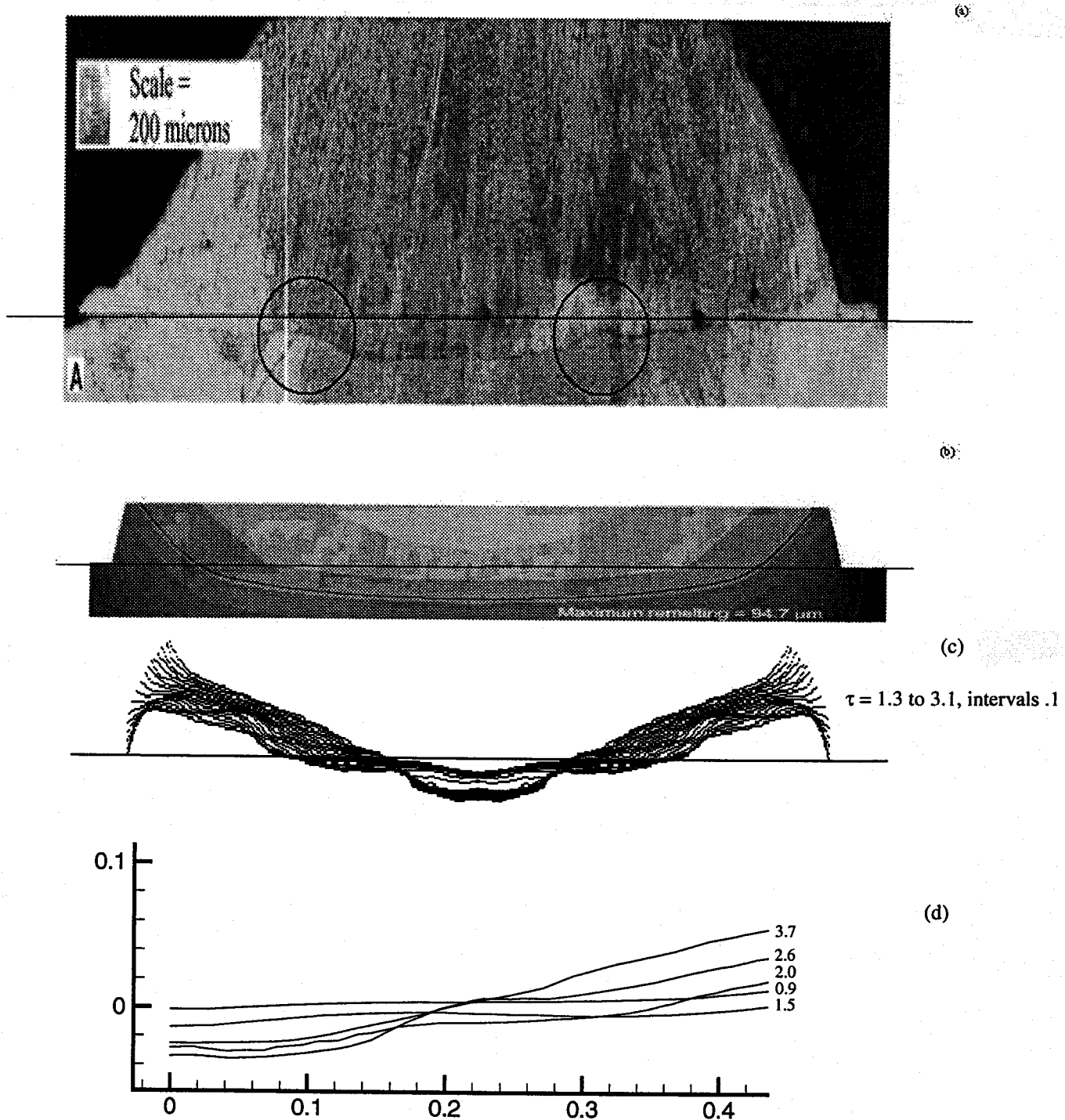


Figure 34: Experimental cross-section of a solidified 3.5 mm steel droplet on a steel substrate (Zarzalejo, et al. 1999) compared with two numerical models, (b, conduction model of Zarzalejo at al., (1999)) and (c,d present study). The horizontal line crossing figures (a, b and c) denotes the substrate surface. The maximum substrate melting location visible as a darker line in (a) is approximated by a heat-diffusion based model (b, (Zarzalejo, et al. 1999)), with a heat conductivity artificially increased for convection, and by the numerical model developed in the present study (c,d). Oscillations of the phase change front around approximately $R=0.2$ could explain the formation of the shoulders circled in the cross-section (a), since the envelope of the instantaneous phase change fronts defines the maximum substrate melting location (c).

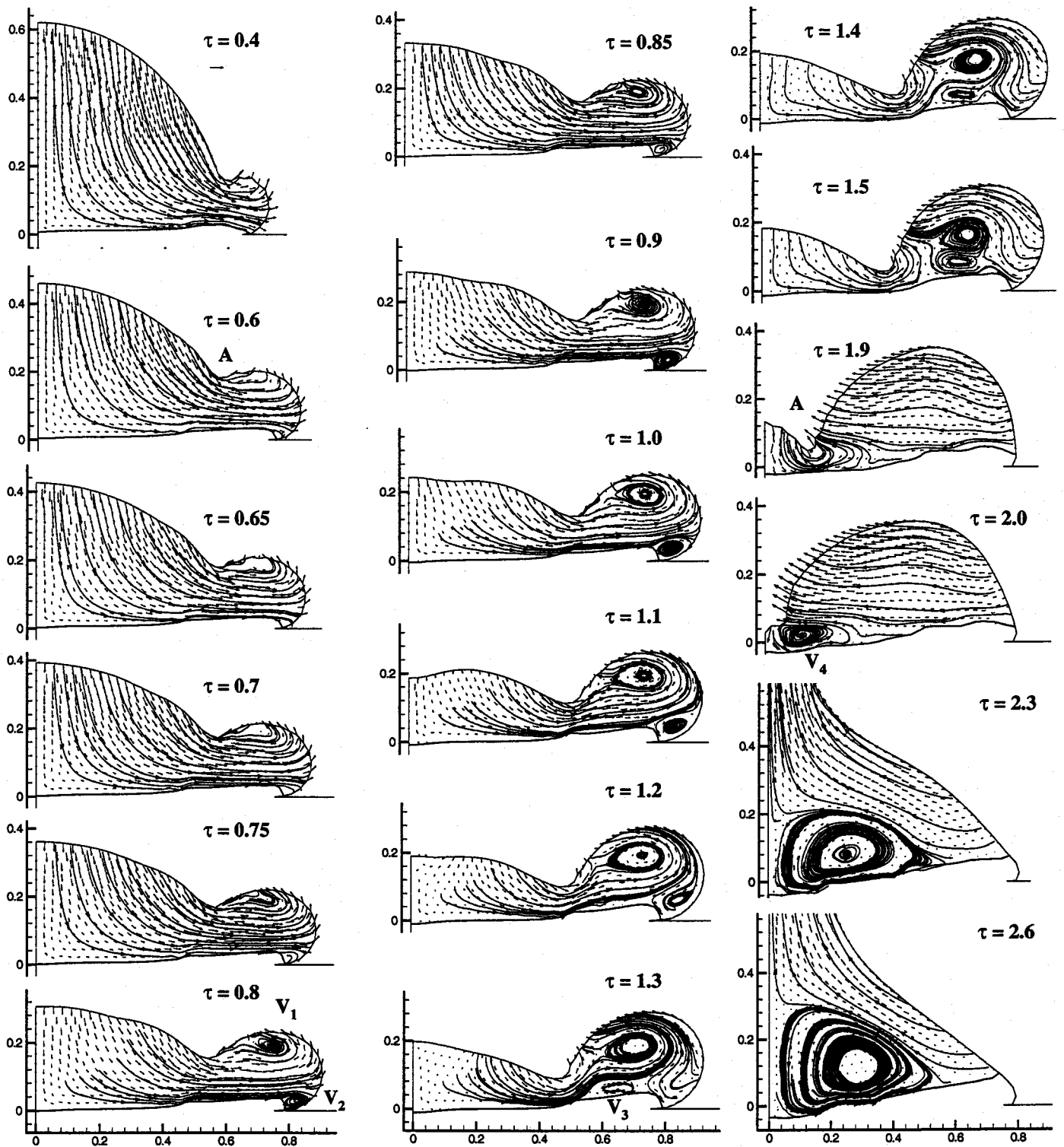


Figure 35: Droplet shape, instantaneous velocity distribution and flow pathlines corresponding to the simulation in Figure 34 (c,d). The dimensionless time is indicated, and the length of the horizontal arrow in the first frame corresponds to a dimensionless velocity of 1.

Our work suggests that considering the complex coupling between fluid dynamics and heat transfer in a complete sense can be fruitful. The case reported in (Zarzalejo, et al. 1999) is the impact of a 3.5-mm stainless steel (they have used the properties for SS308 in their numerical model) droplet at 2500°C on a flat homogeneous substrate at 35°C, with an impact velocity of the order of 1 m/s. We have performed several numerical simulations with our code to reproduce this case. The best agreement was obtained with the following values for the thermophysical properties of SS308 (Miettinen 1997, Murr 1975, Toh September, 2000): $\sigma=1.0\text{Jm}^{-2}$, $\mu=0.005\text{ Pas}$, $\rho_L=7000\text{ kgm}^{-3}$, $\rho_S=7665\text{ kgm}^{-3}$, $L=273000\text{ J/kg}$, $c_L=810\text{ J kg}^{-1}\text{ K}^{-1}$, $c_S=576\text{ J kg}^{-1}\text{ K}^{-1}$, $k_L=28.4\text{ Wm}^{-1}\text{K}^{-1}$, $k_S=23\text{ Wm}^{-1}\text{K}^{-1}$, and $T_M=1445\text{ }^\circ\text{C}$. One should keep in mind that there are variations in the values of these properties reported in the literature (Miettinen 1997 and references therein). These properties and the initial conditions given in (Zarzalejo, et al. 1999) lead to the following dimensionless numbers: $\text{Re} = 5.88 \times 10^3$, $\text{We} = 27.13$, $\text{Fr} = 41.93$, $\text{Pr} = 0.14$, $\text{Ste} = 4.21$ and $\text{SHP} = 0.43$. We assumed an infinite Biot number, in accordance with our results described in Figure 31. Results of our simulation can explain experimental findings such as the formation of the shoulders on the maximum depth of the phase change boundary circled in Figure 34(a), impossible to explain or reproduce with diffusion models (neglecting careful modeling of convection). Figure 34(c,d) shows the phase change boundary obtained with the present simulations at characteristic times. Figure 34c, drawn at the same scale as that of Figure 34(a,b), contains the phase change boundary at many such characteristic times. The bottom of the phase change boundary envelope formed by the superposition of these interfaces corresponds to the maximum depth of the phase change boundary and has a shape comparable to the experimental maximum depth phase change boundary in Figure 34(a), with two clearly visible shoulders. An explanation of the shoulder formation is provided in Figure 34(d), where the instantaneous shape of the phase change boundary is shown for 5 times ranging from before the termination of the spreading ($\tau = 1.3$ is the time of the maximum radial extension of the free surface) to well into the recoiling phase. If the phase change boundary propagates downwards in the early times (from $\tau = 0.9$ to 1.5), its evolution afterwards resembles a wave, with a nodal point at the location $R=0.2$. As a result of this wavy motion, a shoulder is formed.

The physics explaining this phenomenon is related to the complex coupling between the motion of the free surface and convection heat transfer.

Figure 35 shows the free surface, the velocity field and the streamlines corresponding to Figure 34(c-d) for a host of representative times. A mass accumulation ring is formed at the splat periphery of the droplet (also observed in several earlier investigations of droplet impact (Zhao, et al. 1996a, Zhao, et al. 1996b)). There, the spreading is arrested by solidification at the contact line ($\tau = 0.6$). The existence of this mass accu-

mulation ring induces a local minimum of the height of the free surface (point A), and a vortex pair V1 and V2. Vortex V1 is created by the recirculation of the liquid entering and contained in the ring. This flow is directed toward the free surface of the ring and gradually initiates an inward motion of the ring free surface reminiscent of the motion and swelling of a free surface wave (times 0.9 and greater). Vortex V2 is direct consequence of the larger vortex V1, since the flow entering the mass accumulation ring is first deflected slightly upwards by the shoulder shape of the freezing front ($0.4 < R < 0.8$, $\tau = 0.8$) and entrains then the flow in the zone where V2 is created. The creation of V2 can be termed as a "backward facing step effect" due to the shape of the freezing front, underpinning one more time the importance of the fluid mechanics in the freezing process. The creation of this step is a direct consequence of the fact that when the contact line is arrested by freezing, the free surface region above it keeps moving (bulging) outward due to its own inertia (time=0.6). The resulting local downward motion of the liquid in this region retards the solidification process and creates the step configuration which in turn facilitates the formation and growth of vortex V2. During the recoiling phase ($\tau = 1.2$ to 2.6), V2 breaks down and V3 is created because the ring motion displaces V1 towards the Z-axis, engendering a dead zone between V1 and the frozen material under V1. The formation of vortex V3 resembles that of a vortex on the top surface of a forward facing step. Later during recoiling ($\tau = 1.3$ to 1.9), the local minimum A moves toward the Z-axis and accelerates locally the fluid flow through the narrow channel beneath A. This increases the corresponding convection heat transfer, increasing correspondingly the melting rate below A. At the same time, the liquid of the central part of the droplet keeps moving outward. However ($\tau = 1.5$) as it enters the mass accumulation ring, it is now partially "blocked" by the abovementioned vortex pair and it is forced to turn toward the free surface in the neighbourhood of the local minimum A. The resulting flow structure also increases the melting rate below A. The vortex pair V1 and V3 stretches with time and disappears (time 1.9). The valley flow region to the left and below the vortex pair region develops into vortex V4 as the recoiling free surface approaches the centre of symmetry. This vortex grows further as the recoiling proceeds with the majority of the liquid moving upward ($\tau = 2.6$). This vortex increases again the convection heat transfer near the Z-axis. The combination of these melting rate increases (first due to the complex fluid motion under A around times 1.5 and 1.9, then to the creation of V4) explains the formation of the shoulders found experimentally on the maximum substrate melting depth and illustrates the complex coupling between free surface motion, fluid dynamics, heat transfer and phase change.

Chapter 4: Comparison between Microdroplet Impact Experiments and Calculations

4.1. Review of the Literature

In the present chapter, the numerical code described in Chapter 3 is used in order to reproduce transient droplet height measurements described in Figure 17, Chapter 2, in the absence of substrate melting. This kind of matching technique, where unknown and unavailable parameters of a numerical simulation are ‘tuned’ in order to reproduce experiments, has proven to be fruitful with larger droplets, where substantial insight has been obtained in estimating the contact resistance values (Bennett and Poulikakos 1994, Pasandideh-Fard, et al. 1998, Wang and Matthys 1996), or in understanding the complex substrate remelting process (Chapter 3 of the present Thesis). Further discussion of the literature concerning experiments and simulations of microdroplet solidification on a flat substrate can be found in Chapter 2 and Chapter 3, respectively, as well as in Chapter 1.

4.2. Experimental Case

The experimental case studied here concerns the impact of a molten solder droplet on a substrate at a lower temperature, corresponding to the low temperature experiment in Figure 17, which we redefine briefly: an 80 μm Pb-Sn solder droplet impacts with a vertical velocity v_0 of 1.54 ms^{-1} a horizontal substrate whose temperature $T_{2,0}$ equals 48°C . The substrate is a wafer whose layering and thermal properties are described in Table 3. The low temperature-case has been chosen for this matching, since it is the case where solidification occurs at the very early stages of the spreading, reducing the influence of wetting phenomena, whose physics for impact at intermediate Weber numbers is still poorly understood (end of Chapter 2).

Wafers layers (top to bottom)	Thickness l [m]	Heat Capacity, ρc [$\text{Jm}^{-3}\text{K}^{-1}$]	Thermal conductivity, k [$\text{Wm}^{-1}\text{K}^{-1}$]	Reference for the thermal properties
Au	0.1×10^{-6}	2.48×10^6	317	(Incropera and DeWitt 1995)
Ti90W	0.3×10^{-6}	$2.35\text{-}2.55 \times 10^6$	21.9-174	(Incropera and DeWitt 1995)
SiN	1×10^{-6}	2.62×10^6	2.33	(Arx 1998)
P-Si	675×10^{-6}	1.66×10^6	148	(Incropera and DeWitt 1995)

Table 3: Thermal properties and thickness of the wafer layer, top to bottom

The pairs of values in the rows corresponding to the Ti90W alloy are respectively the thermal properties properties of Ti and W, since alloy properties are not necessarily the weighted average of the properties of both components (Dunlop, et al. 1990).

4.3 Theoretical and Numerical Modeling

Modeling each of the four substrate layers separately would have induced a drastic grid refinement in the numerical modeling, since the gold layer thickness is for example only 0.12% of the droplet diameter. We have therefore considered the Au-Ti-W-SiN layer as a unique interface layer of elements on the top of the Silicon substrate, and this approach can be justified as follows: Similarly to the procedure in Chapter 3, we set up an interfacial layer at the top of the substrate, with a heat capacity and a thermal conductivity that results both from the Au-Ti-W-SiN layering and the imperfect thermal contact between the droplet and the splat (Wang and Matthys 1996). The heat capacity of the interface layer is determined by a weighted average of the heat capacities:

$$\rho c_{\text{interface}} = \frac{1}{\sum l_i} \sum l_i (\rho c)_i \quad (48)$$

$$\rho c_{\text{interface}} = 2.6 \times 10^6 \text{ [Jm}^{-3}\text{K}^{-1}] \quad (49)$$

The thermal conductivity $k_{\text{interface}}$ of the interface layer is determined by considering the layer as a series (Incropera and DeWitt 1995) of four thermal resistances:

three thermal resistances corresponding to the Au-Ti-W-SiN layers, and the resistance due to imperfect thermal contact between the splat and substrate.

$$R_{\text{interface}} = \frac{\sum l_i}{k_{\text{interface}}} = \sum \frac{l_i}{k_i} + \frac{1}{h_3} \quad (50)$$

where h_3 is the heat transfer coefficient expressing the imperfect thermal contact between splat and substrate. The above approach implies one-dimensional heat transfer in the interface layer, which is justified by the thickness of the layer (1.4 microns) with respect to the typical droplet diameter (80 microns).

Introducing the values of Table 3 in the above equation yields

$$R_{\text{interface}} = 4.3 \text{ to } 4.5 \times 10^{-7} + \frac{1}{h_3} \text{ [K m}^2\text{W}^{-1}] \quad (51)$$

where the range 4.3 to 4.5×10^{-7} corresponds to a thermal conductivity of the TiW layer of 20, respectively $170 \text{ Wm}^{-1}\text{K}^{-1}$. Since a value of 4×10^{-5} has been used as an estimate of $1/h_3$ ($h_3 = 2.5 \times 10^4 \text{ Wm}^{-2}\text{K}^{-1}$) in a similar problem (Waldvogel and Poulikakos 1997), the first term of the RHS in the above equation can be neglected and the above equation simplifies to:

$$R_{\text{interface}} \approx \frac{1}{h_3} = R_3 \quad (52)$$

Physically, the above simplification is explained by the fact that the major resistance to heat transfer at the interface is caused by the imperfect thermal contact between the splat and the substrate and not by the metallization layers at the top of the wafer.

4.3. Numerical Simulation Procedure

We have performed seven numerical simulations with the code presented in Chapter 3 (without remelting) aiming at reproducing the low temperature case described above and at testing the modeling sensitivity to variations of parameters like surface tension and Biot number.

4.4. Results and Discussion

4.4.1. Baseline Case and Parametric Variations

The simulation that was found to have the best agreement with the experiments has been performed with the following values for the thermophysical properties

of the eutectic solder: $\sigma=0.507\text{Jm}^{-2}$, $\mu=0.00262\text{Pas}$, $\rho_L=8218\text{kgm}^{-3}$, $\rho_S=8420\text{kgm}^{-3}$, $L=42000\text{J/kg}$, $c_L=238\text{J kg}^{-1}\text{K}^{-1}$, $c_S=176\text{J kg}^{-1}\text{K}^{-1}$, $k_L=25\text{Wm}^{-1}\text{K}^{-1}$, $k_S=48\text{Wm}^{-1}\text{K}^{-1}$, and $T_M=183\text{ }^\circ\text{C}$. These properties and the initial conditions correspond to the low temperature case described in Figure 14 and Figure 17. The following dimensionless numbers are obtained: $Re = 386$, $We = 3.08$, $Fr = 3022$, $Pr = 0.025$, $Ste = 0.765$, and $SHP = 0.166$. The substrate is flat with radial and axial dimensions respectively four and eight times larger than the diameter of the droplet, in order to simulate the impact on a substrate much larger than the droplet. We assumed two distinct values for h_3 , the heat transfer coefficient through the interface. The value of h_3 was set individually for every interface element in accordance with the phase of the splat material in contact with the element (liquid, respectively solid): $h_{3L} = 1.31 \times 10^5\text{ Wm}^{-2}\text{K}^{-1}$, $h_{3S} = 1.25 \times 10^4\text{ Wm}^{-2}\text{K}^{-1}$, giving the respective Biot numbers, $B_{iL} = 0.42$ and $B_{iS} = 0.04$. This approach can be considered as a first step toward a thorough consideration of the strong time dependence of the interfacial heat transfer measurements (Attinger, et al. 2000a, Pasandideh-Fard and Mostaghimi 1996, Wang and Matthys 1996).

The mesh density is similar as in the substrate melting study (Chapter 3), while the dimensionless time step is twice as large ($d\tau=1.0 \times 10^{-3}$ instead of 5×10^{-4}), since a sensitivity study showed excellent agreement between simulations of the temporal evolution the Z-axis contact point with the free surface of the droplet, using both time steps.

Four runs besides the baseline case have been performed in order to address the sensitivity of the modeling to the value of the surface tension (inputted through the Weber number) and to the value of the interfacial Biot number B_{iS} (B_{iL} is kept at a constant value that sets the initiation of the freezing at the instant of the spreading arrest). The chosen values of Weber, B_{iL} and B_{iS} are given in the following table.

Run	We	B_{iS}
baseline	3.1	0.04
low σ	6.0	0.04
high σ	1.5	0.04
high B_{iS}	3.0	0.06
low B_{iS}	3.0	0.02

Table 4: Baseline case and 4 parameter combinations used for examining the role of the surface tension and interfacial heat transfer during droplet impact and spreading on a colder substrate.

4.4.2. General Description of the Droplet Oscillation Process

The temporal evolution of the dimensionless height viewed from the side, H_t , calculated numerically for the baseline case is shown in Figure 36, and is compared

with the same parameter obtained experimentally in Chapter 2, Figure 17 (one star per measurement).

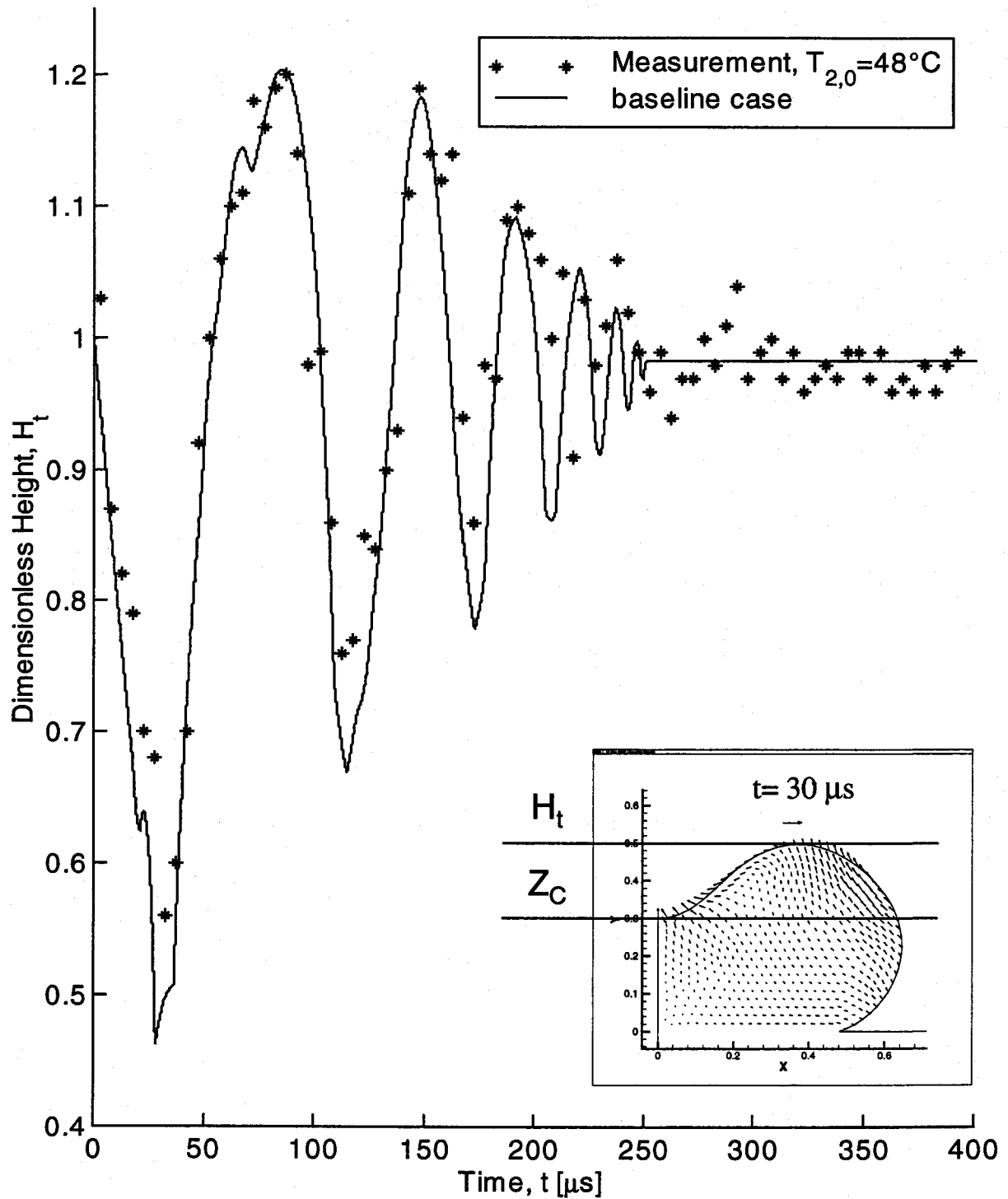


Figure 36: Comparison between measurement and simulations of the droplet height as a function of time, with a substrate initial temperature of 48°C .

The experimentally observed mildly damped oscillation process (with a frequency increase due to the freezing) is reproduced in Figure 36 by our numerical study. A good agreement in terms of maximum amplitude and frequency of the oscillation has been obtained for the first three periods of droplet height oscillation (latter measurements are too noisy to be interpreted). The final value of the simulated droplet height shows a very good agreement with the measurements. This agreement between numerical results and experiments confirms definitely the fact that the ripples visible on the frozen drop surface are formed by the competition between a freezing from below and oscillations of the free surface. The droplet cross-section in Figure 36 shows that the dimensionless height viewed from the side does not always correspond to the same point as the Z-axis contact point, shown for example in Figure 26, and the abrupt transition between both points in terms of maximum height causes the surprising shape of the droplet height curve, for example by $20 < t < 40 \text{ m}_s$.

4.4.3. Parametric Variations: Surface Energy and Biot number

The effects of surface energy variations are exemplified by two results shown in Figure 37, corresponding to half ($We = 6.0$), respectively twice ($We = 3.0$), the surface energy of the baseline case. Only the first $200 \mu\text{s}$ have been plotted for clarity. In the $We=6.0$ case (low surface tension), the frequency of the oscillations of the droplet is lower than the experimental frequency (as exemplified by the time of the second minimum of the height, $150 \mu\text{s}$). Such an increase of the oscillation frequency can be explained by means of Eq. (19), which shows that the frequency of the droplet free oscillation is proportional to the square root of the surface tension. The final height (not shown) of the case ($We = 6.0$) is also slightly smaller than in the experiments, which can be explained by the fact that the droplet spreads more in the high Weber case ($\beta_\infty = 1.08$) than in the baseline case ($\beta_\infty = 0.96$). The reason for this spreading increase at higher Weber number is that for the same amount of inertia forces driving the spreading, there are less surface forces, which should arrest the spreading. In the $We=1.5$ case (high surface tension), the frequency of the oscillations of the droplet is higher than the experimental frequency (as exemplified by the time of the first two minima of the height).

Figure 38 shows three simulations of the above-described measurement with different heat transfer coefficients between the substrate and the solidifying splat, expressed in terms of the solid interfacial Biot number B_{iS} . It appears that the rate of the increase in oscillation frequency is proportional to B_{iS} (The higher the B_{iS} is, the higher the rate of increase in oscillation frequency). This can be understood by considering again Eq. (19), which relates the oscillation frequency to the inverse of the liquid volume square root. Increasing the interfacial Biot number augments the heat exchange at the interface, accelerating the solidification rate. The faster diminishing

liquid volume taking part in the oscillation induces therefore a larger frequency increase of the height oscillation. Since the oscillation frequencies corresponding to $B_{is} = 0.06$ or 0.02 are respectively too high or too low compared to the experimental values in Figure 37, the effective interfacial Biot number has to be between the two values. This approach that matches measured and simulated droplet oscillations in order to determine B_{is} can be considered as a viable method for determining phenomenologically the heat transfer in the presence of an interface. Contrary to matching techniques including thermocouple measurements (Bennett and Poulikakos 1994, Pasandideh-Fard, et al. 1998, Wang and Matthys 1996), this method is non-intrusive, therefore better suited for experiments involving microdroplets, where a classical thermocouple measurement would have the following two drawbacks. First, it would strongly perturb the event to observe. Second, thermocouple positioning would be a delicate issue, considering the highly transient and local nature of the flow field and convection heat transfer (Chapter 3). However, one should keep in mind that matching techniques such as the one developed here only give a heuristic insight in the physics of interfacial heat transfer, which is typically a microscale phenomenon. According to this lack of understanding, there is no guarantee that the values obtained for the Biot number can be used generally. I expect that this rather poor understanding of interfacial heat transfer will be improved by investigating systematically topics like non-equilibrium solidification, recalescence, as well as the influence of initial temperature difference between splat substrate on the interfacial heat transfer. To this end, it is worth noting the emergence of thermal conductivity studies (Lukes, et al. 2000) using discrete methods like Molecular Dynamics. These discrete methods at the molecular level show promise to produce a physical (not only phenomenological) insight into interfacial heat transfer.

It is interesting to mention that a situation like the baseline case considered here, where the interfacial heat transfer coefficient is larger during the spreading than during the solidification phase, has also been evidenced in the most extensive experimental study on contact resistance to date (Wang and Matthys 1996), where the authors attributed this fact to the following reasons: at first, when the molten material lies upon the colder substrate, one would expect good thermal contact because the fluidity of the melt allows it to 'match' the shape of the substrate (with the exception of small scale roughness and gas-filled gaps). In addition, the high temperature of the melt may result in good mechanical or chemical bond between the melt and the substrate. This good contact would then degrade due to thermal contraction of the splat upon solidification. One should notice the very qualitative, almost aristotelic, nature of the explanations given. This is again a sign that the real physics of the microscale and transient contact resistance phenomenon is beyond reach of continuum modeling and that novel discrete methods need to be applied at the molecular level.

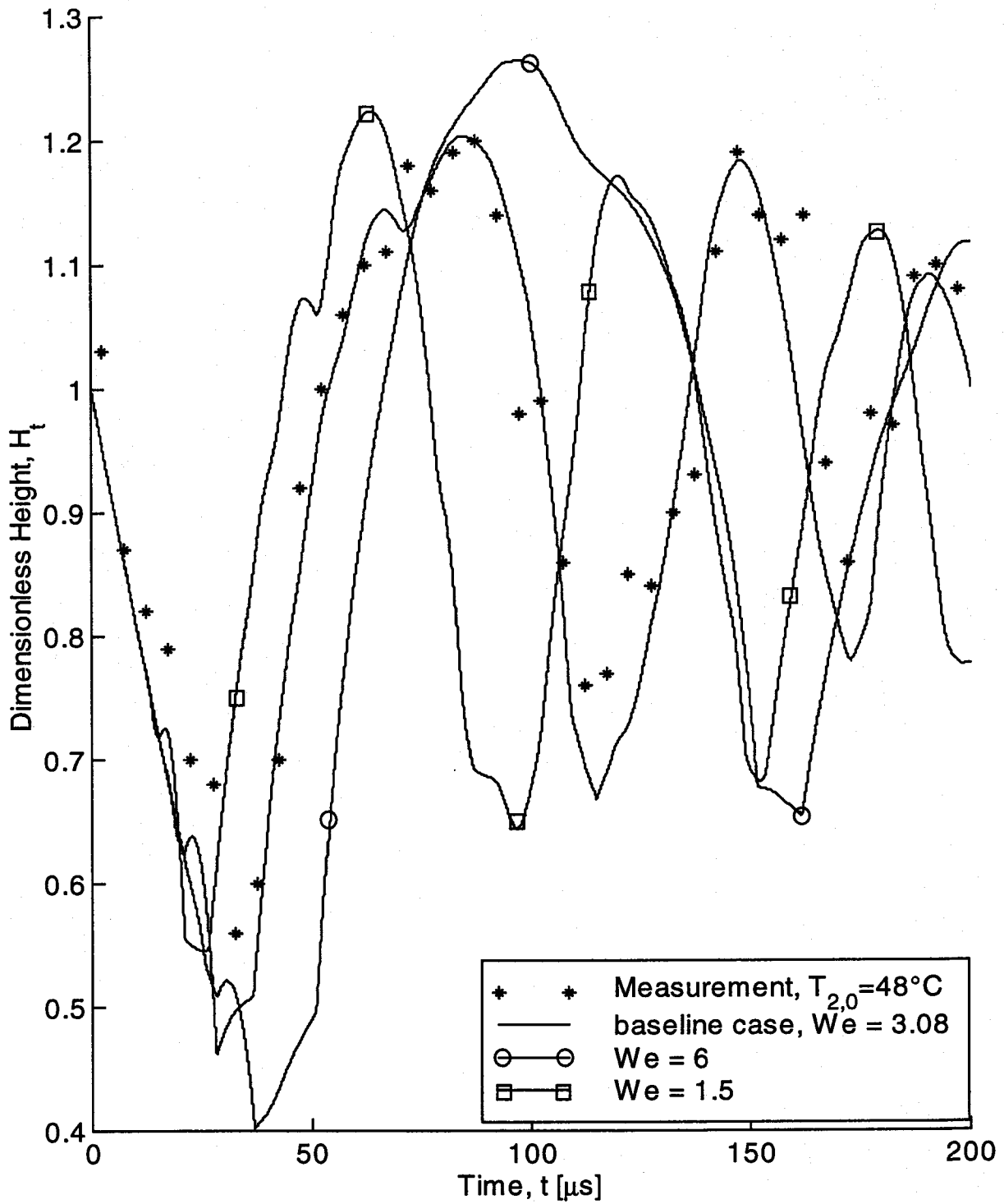


Figure 37: Comparison between measurement and simulations of the droplet height as a function of time, for three values of the Weber number. The substrate initial temperature is 48°C .

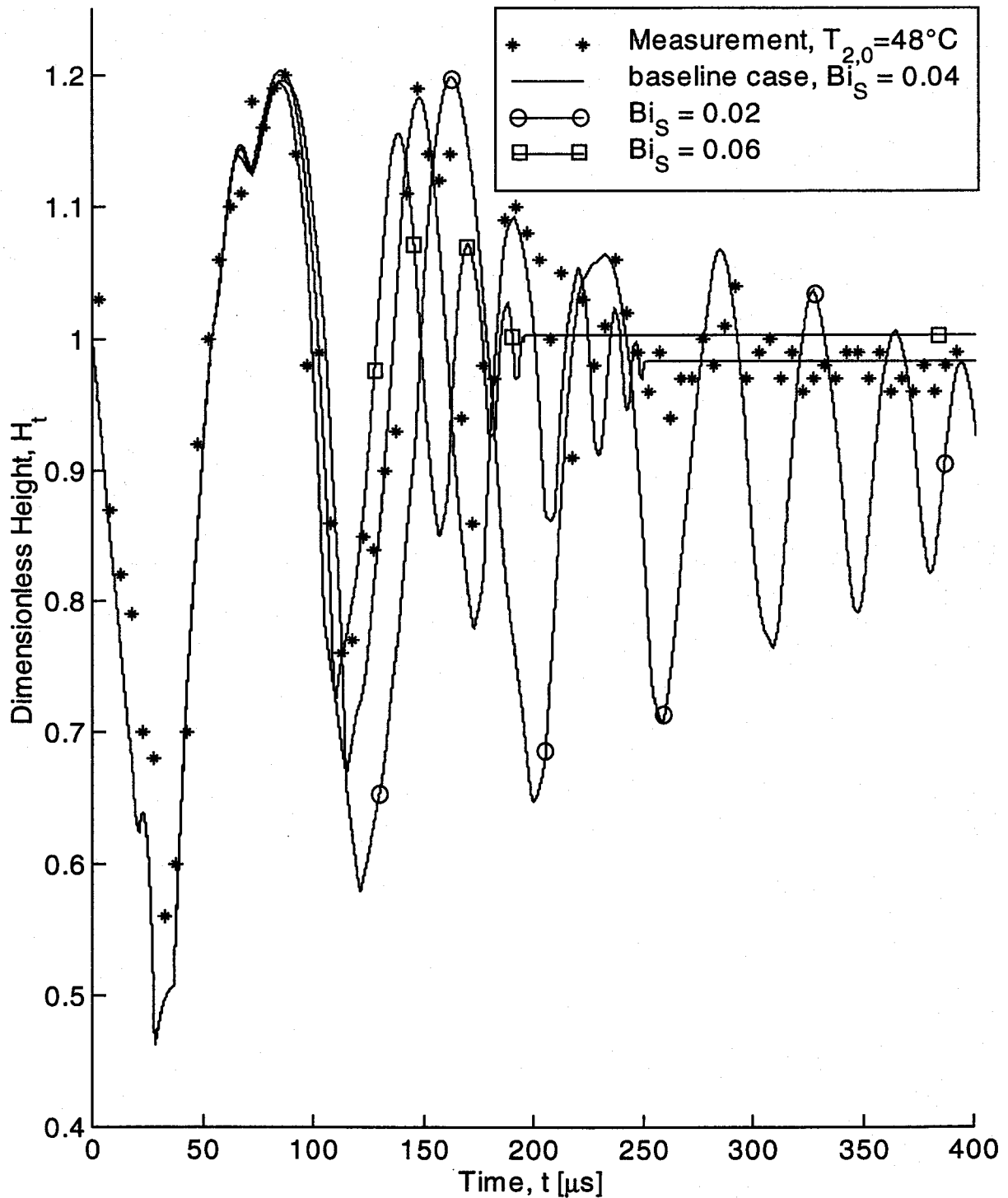


Figure 38: Comparison between measurement and simulations of the droplet height as a function of time, for three values of the interfacial Biot number Bi_S , characterizing the thermal exchange between the substrate and the solidifying splat above it. The substrate initial temperature is 48°C .

Conclusions

Chapter 2 of this thesis presents, to the best of our knowledge, the first experimental results on the transient fluid dynamics, wetting and solidification of molten microdroplets impacting on a substrate, which are directly relevant to the novel solder jetting technology in manufacturing of microelectronics. It was shown that the ripples on the solidified drop surface are due to a strong coupling between solidification and flow oscillations, as was suggested by earlier numerical results pertaining to a comparable parameter range.

In a first series of experiments, the value of the substrate initial temperature was varied in order to study its influence on the spreading and solidification process. Transient measurements of the droplet height above the substrate have been carried out, showing a damped oscillation. These results suggest that the solidification time depends non-monotonically on the substrate temperature. This finding, although appearing counterintuitive, is supported by a simple order of magnitude analysis. Transient measurements of the spread factor showed that the substrate initial temperature significantly affects the spreading for substrate temperatures ranging from 48°C to 98°C ($Ste=0.77$ to 0.48). This indicates that spreading is arrested by solidification at the wetting line. At higher substrate temperatures, the spread factor was practically independent of the substrate temperature.

Measurements of the wetting angle dynamics for different conditions of impact velocities and substrate temperatures have also been carried out. The influence of the initial conditions on the evolution of the apparent wetting angle was analyzed in both regimes and two successive regimes have been distinguished. It was established that the wetting angle dynamics is strongly coupled to the evolution of the droplet free surface. No quantitative agreement with the widely used Hoffman's correlation for wetting was found. This finding corroborates recent publications that showed the need to introduce transient and nonlocal effects in wetting modeling, an approach that could be investigated by hybrid (discrete-continuum) numerical methods.

The main features and results of a numerical investigation of molten microdroplet impact and solidification on a colder flat substrate that can melt are described in Chapter 3. Recent advances in material processing technologies such as thermal spray deposition have evidenced the urgent need for understanding and quantifying the substrate melting phenomenon. In our study, the temporal evolution of the melted volume has been determined and presented for various combinations of thermal and fluid dynamics parameters. A non-monotonic dependence of the solidification time on the superheat parameter has been found, which departs from predictions of 1D conduction models. A strong influence of the impact velocity on the amount of substrate melting underpins the importance of the fluid dynamics on the substrate melting phenomenon. The influence of the interfacial heat transfer between the splat and the substrate has been studied, and the existence of a threshold Biot number for

substrate melting modeling has been demonstrated. Substrate melting maps have been produced, where the amount of substrate melting is expressed as a function of the impact velocity v_0 and the superheat parameter SHP. Significant material mixing between the substrate and splat has been identified and quantified, and implications of this mixing have been discussed. Good agreement between the numerical results and experiments of previous investigators for larger (mm-size) droplets was obtained, and an explanation for the complex shape of the maximum melting depth boundary found in these experiments has been provided for the first time. In all, this numerical study demonstrates that the complex coupling between free surface motion, fluid dynamics, material mixing and multidimensional heat transfer, including convection, is of central importance to the thorough understanding of the physics of substrate melting problems involving droplet sizes in the range $O(100 \text{ microns})$ to $O(1 \text{ mm})$.

Chapter 4 presents a comparison between experimental results with microdroplets (Chapter 2) and results of the numerical modeling presented in this study (Chapter 3). A good agreement of the oscillation process of the droplet maximum height has been obtained between experimental and numerical results, and the sensitivity of the modeling to values of surface energy and interfacial Biot number has been demonstrated. Such an approach that matches experimental and numerical results, by tuning unknown problem parameters whose microscale physics makes them currently difficult to attain, is a viable method for investigating mesoscopic phenomena such as interfacial heat transfer. This method, however, does not provide a deep insight in the physics of interfacial heat transfer. Here, diverse methods at the molecular level appear promising, but are not yet developed to the extent that they could be used reliably in realistic applications.

References

1. **Amon, C. H., K. S. Schmaltz, R. Merz, and F. B. Prinz.** 1996. Numerical and Experimental Investigation of Interface Bonding via Substrate Remelting of an Impinging Molten Metal Droplet. *Journal of Heat Transfer* **118**:164-172.
2. **Anantharaman, T. R., and C. Suryanarayana.** 1971. Review: A decade of Quenching from the Melt. *Journal of Materials Science* **6**:1111-1135.
3. **Arx, M. v.** 1998. Thermal properties of CMOS Thin Films. Ph. D. Thesis. ETH Zurich.
4. **Attinger, D., S. Haferl, Z. Zhao, and D. Poulikakos.** 2000a. Transport Phenomena in the Impact of a Molten Droplet on a Surface: Macroscopic Phenomenology and Microscopic Considerations. Part II: Heat Transfer and Solidification. *In* C. L. Tien (ed.), *Annual Review of Heat Transfer*.
5. **Attinger, D., Z. Zhao, and D. Poulikakos.** 1999. Analytical Estimation of the Maximum Spreading Diameter during Impact of a Drop on a Colder Surface Including Thermocapillary and Gravitational Effects, CD-Rom without pagination, ILASS 1999 Conference, Spray Impact on Wall and Films.
6. **Attinger, D., Z. Zhao, and D. Poulikakos.** 2000b. An Experimental Study of Molten Microdroplet Surface Deposition And Solidification: Transient Behavior and Wetting Angle Dynamics. *Journal of Heat Transfer* **122**(3):544-556.
7. **Bach, P., and O. Hassager.** 1985. An Algorithm for the Use of the Lagrangian Specification in Newtonian Fluid Mechanics and Applications to Free-Surface Flow. *Journal of Fluid Mechanics* **152**:173-190.
8. **Batchelor, G. K.** 1967. *An Introduction to Fluid Dynamics*. University Press, Cambridge, New York.
9. **Bennett, T., and D. Poulikakos.** 1994. Heat Transfer Aspects of Splat-Quench Solidification: Modeling and Experiment. *Journal of Materials Science* **29**:2025-2039.
10. **Bennett, T., and D. Poulikakos.** 1993. Splat-Quench Solidification: Estimating the Maximum Spreading of a Droplet Impacting a Solid Surface. *J. Mat. Sci.* **28**:963-970.
11. **Blake, T. D., M. Bracke, and Y. D. Shikhmurzaev.** 1999. Experimental evidence of nonlocal hydrodynamic influence on the dynamic contact angle. *Phys. Fluids* **11**:1995-2007.
12. **Blake, T. D., and J. M. Haynes.** 1969. Kinetics of Liquid/Liquid Displacement. *J. Coll. Inter. Sci.* **30**:421-423.
13. **Blake, T. D., and K. J. Ruschak.** 1997. Wetting: Static and Dynamic Contact Lines. *In* S. E. Kistler and P. M. Schweizer (ed.), *Liquid Film Coating*, 1 ed. Chapman and Hall, London.

14. **Boer, A. W. J. P. d.** 1996. Marangoni Convection: Numerical Models and Experiments. Ph. D. Thesis. Technische Universiteit Eindhoven, Eindhoven.
15. **Bushko, W., and I. R. Grosse.** 1991. New Finite Element Method for Multi-dimensional Phase Change Heat Transfer Problems. Numerical Heat Transfer B **19**:31-48.
16. **Chandra, S., and C. T. Avedisian.** 1991. On the Collision of a Droplet with a Solid Surface. Proc. R. Soc. Lond. A **432**:13-41.
17. **Che, J., S. Ceccio, and G. Tryggvason.** February 1999. Computations of Structures Formed by the Solidification of Impinging Molten Metal Drops. Presented at the 1999 TMS Annual Meeting, San Diego, California.
18. **Dunlop, J., E. Waterman, and T. Brat.** 1990. Effects of Ti-W Target Processing Methods on Defect Generation During VLSI Device Fabrication. Presented at the 37th Annual Symposium of the American Vacuum Society, Toronto, Canada.
19. **Dussan, E. B.** 1979. On the Spreading of Liquids on Solid Surfaces: Static and Dynamic Contact Lines. Ann. Rev. Fluid Mech. **11**:371-400.
20. **Engel, O. G.** 1955. Waterdrop Collisions with Solid Surfaces. J. Res. Nat. Bur. Stand. **54**(5):281-298.
21. **Fukai, J., Y. Shiba, T. Yamamoto, O. Miyatake, D. Poulikakos, C. M. Megaridis, and Z. Zhao.** 1995. Wetting Effects on the Spreading of a Liquid Droplet Colliding with a Flat Surface: Experiment and Modeling. Physics of Fluids **7**(2):236-247.
22. **Fukai, J., Z. Zhao, D. Poulikakos, C. M. Megaridis, and O. Miyatake.** 1993. Modeling of the Deformation of a Liquid Droplet Impinging upon a Flat Surface. Physics of Fluids A **5**:2588-2599.
23. **Gao, F., and A. Sonin.** 1994. Precise Deposition of Molten Microdrops: The Physics of Digital Microfabrication. Proc. R. Soc. Lond. A **444**: 533-554.
24. **Hadjiconstantinou, N. G.** 1999. Hybrid Atomistic-Continuum Formulations and the Moving Contact-Line Problem. Journal of Computational Physics **154**:245-265.
25. **Haferl, S., V. Butty, D. Poulikakos, J. Giannakouros, K. Boomsma, C. M. Megaridis, and V. Nayagam.** November 2000. Freezing of Molten Solder Droplets Impacting onto Flat Substrates in Microgravity. Presented at the 2000 International Mechanical Engineering Congress and Exhibition, Orlando, Florida.
26. **Haferl, S., Z. Zhao, J. Giannakouros, D. Attinger, and D. Poulikakos.** 2000. Transport Phenomena in the Impact of a Molten Droplet on a Surface: Macroscopic Phenomenology and Microscopic Considerations. Part I: Fluid Dynamics. In C. L. Tien (ed.), Annual Review of Heat Transfer.
27. **Haile, J. M.** 1992. Molecular Dynamics Simulation: Elementary Methods. Wiley-Interscience, New York.

28. **Hayes, D. J., and D. B. Wallace.** 1998. Solder Jet Printing: Wafer Bumping and CSP Applications. *Chip Scale Review* **2**(4):75-80.
29. **Hayes, D. J., D. B. Wallace, and M. T. Boldman.** 1992. Picoliter Solder Droplet Dispension, p. 316-321, ISHM Symposium 92 Proceedings.
30. **Hirt, C. W., and B. D. Nichols.** 1980. Adding Limited Compressibility to Incompressible Hydrocodes. *Journal of Computational Physics* **34**:390-400.
31. **Hoffmann, R. L.** 1975. A Study of the Advancing Interface. I. Interface Shape in Liquid-Gas Systems. *J. Coll. Inter. Sci.* **50**:228-241.
32. **Iida, T., and R. I. L. Guthrie.** 1988. *The Physical Properties of Liquid Metals.* Oxford University Press, Oxford, New York.
33. **Inada, S., Y. Miyasaka, K. Nishida, and G. R. Chandratilleke.** 1983. Transient Temperature Variation of a Hot Wall due to an Impinging Water Drop - Effect of Subcooling of the Water Drop. *Proc. ASME-JSME Thermal Engineering Joint Conf.* **1**:173-182.
34. **Incropera, F. P., and D. P. DeWitt.** 1995. *Fundamentals of Heat and Mass Transfer*, 3rd ed. Wiley.
35. **Jones, H.** 1971. Cooling, Freezing and Substrate Impact of Droplets Formed by Rotary Atomization. *Journal of physics D: Applied physics* **4**:1657-1660.
36. **Jones, H.** 1982. *Rapid Solidification of Metals and Alloys*, vol. 8. Great Britain Institution of Metallurgists, London.
37. **Jones, H.** 1973. Splat Cooling and Metastable Phases. *Report of Progress in Physics* **48**:1425-1497.
38. **Kang, B., J. Waldvogel, and D. Poulikakos.** 1995. Remelting Phenomena in the Process of Splat Solidification. *Journal of Materials Science* **30**:4912-4925.
39. **Kang, B., Z. Zhao, and D. Poulikakos.** 1994. Solidification of Liquid Metal Droplets Impacting Sequentially on a Solid Surface. *Journal of Heat Transfer* **116**:436-445.
40. **Kawahara, M., and H. Hirano.** 1983. A Finite Element Method for High Reynolds Number Viscous Fluid Flow using a Two Step Explicit Scheme. *International Journal for Numerical Methods in Fluids* **3**:137-163.
41. **Kistler, S. F.** 1993. *Hydrodynamics of Wetting.* In J. C. Berg (ed.), *Wettability*, 1st ed. Dekker, New York.
42. **Landau, L. D., and E. M. Lifshitz.** 1959. *Fluid Mechanics, Course of Theoretical Physics*, 1st ed, vol. 6. Pergamon, Oxford.
43. **Lee, Y. C., and W. T. Chen.** 1998. *Manufacturing challenges in electronic packaging*, Chapman & Hall, London.
44. **Levin, Z., and P. V. Hobbs.** 1971. Splashing of Water Drops on Solid and Wetted Surfaces: Hydrodynamics and Charge Separations. *Philos. Trans. R. Soc. London A* **269**:555-585.

45. **Liu, H., E. J. Lavernia, and R. H. Rangel.** 1993. Numerical Simulation of Substrate Impact and Freezing of Droplets in Plasma Spray Processes. *J. Phys. D : Appl. Phys.* **26**:1900-1908.
46. **Lukes, J. R., D. Y. Li, X.-G. Liang, and C. L. Tien.** 2000. Molecular Dynamics Study of Solid Thin-Film Thermal Conductivity. *Journal of Heat Transfer* **122**:536-543.
47. **Madejski, J.** 1983. Droplets on Impact with a Solid Surface. *International Journal of Heat and Mass Transfer* **26**:1095-1098.
48. **Madejski, J.** 1976. Solidification of Droplets on a Cold Surface. *International Journal of Heat and Mass Transfer* **19**:1009-1013.
49. **Mcperson, R.** 1980. On the Formation of Thermally Sprayed Alumina Coatings. *Journal of Materials Science* **15**:3141-3149.
50. **Megaridis, C. M., K. Boomsma, D. Poulikakos, and V. Nayagam.** 2000. Contact Angle Dynamics of Molten Solder Droplets Impacting onto Flat Substrates in Reduced Gravity. Presented at the International Conference of Theoretical and Applied Mechanics, Chicago, Illinois, USA.
51. **Miettinen, J.** 1997. Calculation of Solidification-Related Thermophysical Properties for Steels. *Metallurgical and Materials Transactions B* **28 B**:281-297.
52. **Mundo, C., M. Sommerfeld, and C. Tropea.** 1995. Droplet-Wall Collisions: Experimental Studies of the Deformation and Breakup Process. *Int. J. Multiphase Flow* **21**:151-173.
53. **Murr, L. E.** 1975. *Interfacial Phenomena in Metals and Alloys.* Addison-Wesley, Reading, Massachusetts.
54. **Ohl, C. D., A. Philipp, and W. Lauterborn.** 1995. Cavitation bubble collapse studied at 20 million frames per second. *Annalen-der-Physik (Leipzig)* **4(1)**:26-34.
55. **Orme, M.** 1993. A Novel Technique of Rapid Solidification Net-Form Materials Synthesis. *Journal of Materials Engineering and Performance* **2(3)**:399-405.
56. **Orme, M., C. Huang, and J. Courter.** 1996. Deposition Strategies for Control of Microstructures Microporosity and Surface Roughness in Droplet-Based Solid Freeform Fabrication of Structural Materials, p. 125-143. *In* E. F. Matthys and W. G. Truckner (ed.), *Melt Spinning, Strip Casting and Slab Casting.* The Minerals, Metals and Materials Society, Warrendale Pennsylvania.
57. **Orme, M., Q. Liu, and J. Fischer.** 2000. Mono-disperse Aluminum Droplet Generation and Deposition for Net-Form Manufacturing of Structural Components, p. 200-207, Eighth International Conference on Liquid Atomization and Spray Systems, Pasadena, CA, USA, July 2000.
58. **Orme, M., and R. Smith.** 2000. Enhanced Aluminum Properties with Precise Droplet Deposition. *ASME Journal of Manufacturing Science and Engineering* **122**:484-493.

59. **Pasandideh-Fard, M., R. Bohla, S. Chandra, and J. Mostaghimi.** 1998. Deposition of Tin Droplets on a Steel Plate: Simulations and Experiments. *Int. J. Heat and Mass Transfer* **41**(19):2929-2945.
60. **Pasandideh-Fard, M., and J. Mostaghimi.** 1996. On the Spreading and Solidification of Molten Particles in a Plasma Spray Process: Effect of Thermal Contact Resistance. *Plasma Chemistry and Plasma Processing* **16**:83-98.
61. **Pasandideh-Fard, M., Y. M. Qiao, S. Chandra, and J. Mostaghimi.** 1996. Capillary Effects during Droplet Impact on a Solid Surface. *Phys. Fluids* **8**:650-659.
62. **Pederson, C. O.** 1970. An Experimental Study of the Dynamic Behavior and Heat Transfer Characteristics of Water Droplets Impinging upon a Heated Surface. *Int. J. Heat Mass Transfer* **13**:369-381.
63. **Poulikakos, D.** 1994. *Conduction Heat Transfer*. Prentice-Hall, Englewood Cliffs, New Jersey.
64. **Rangel, R. H., and X. Bian.** 1997. Metal-Droplet Deposition Model Including Liquid Deformation and Substrate Remelting. *International Journal of Heat and Mass Transfer* **40**:2549-2564.
65. **Salcudean, M., and Z. Abdullah.** 1988. On the Numerical Modeling of Heat Transfer during Solidification Processes. *Int. J. Num. Meth. Eng.* **25**:445-473.
66. **Savic, P., and G. T. Boulton.** 1955. *The Fluid Flow Associated with the Impact of Liquid Drops with Solid Surfaces* Rept. no. MT-26. Nat. Res. Council Canada.
67. **Schiaffino, S., and A. A. Sonin.** 1997a. Molten Droplet Deposition and Solidification at Low Weber Numbers. *Phys. Fluids* **9**:3172-3187.
68. **Schiaffino, S., and A. A. Sonin.** 1997b. Motion and Arrest of a Molten Contact Line on a Cold Surface: An Experimental Study. *Phys. Fluids* **9**:2217-2226.
69. **Schiaffino, S., and A. A. Sonin.** 1997c. On the Theory for the Arrest of an Advancing Molten Contact Line on a Cold Solid of the Same Material. *Phys. Fluids* **9**:2227-2233.
70. **Schmaltz, K. S., and C. H. Amon.** 1996. Thermal Issues in Microcasting Shape Deposition Manufacturing, p. 125-143. *In* E. F. Matthys and W. G. Truckner (ed.), *Melt Spinning, Strip Casting and Slab Casting*. The Minerals, Metals and Materials Society, Warrendale Pennsylvania.
71. **Schwabe, D., A. Scharmann, and F. Preisser.** 1982. Studies of Marangoni Convection in Floating Zones. *Acta Astronautica* **9**(3):183-186.
72. **Shyy, W., H. S. Udaykumar, M. M. Raouf, and R. W. Smith.** 1996. *Computational Fluid Dynamics with Moving Boundaries*. Taylor and Francis.
73. **Stow, C. D., and M. G. Hadfield.** 1981. An Experimental Investigation of Fluid Flow Resulting from the Impact of a Water Drop with an Unyielding Dry Surface. *Proc. Roy. Soc. London A* **373**:419-441.
74. **Tanner, L. H.** 1979. The Spreading of Silicone Oil Drops on Horizontal Surfaces. *J. Phys. D: Appl. Phys* **12**:1473-1484.

75. **Toda, S.** 1974. A Study of Mist Cooling (2nd Report: Theory of Mist Cooling and Its Fundamental Experiments). *Heat Transfer Japanese Research* **3**(1):1-44.
76. **Toh, T.** September, 2000. Personal Communication. Nippon Steel Research Laboratories, Futtsu, Japan.
77. **Ueda, T., T. Enomoto, and M. Kanetsuki.** 1979. Heat Transfer Characteristics and Dynamic Behavior of Saturated Droplets Impinging on a Heated Vertical Surface. *Bulletin of the JAME* **22**(167):724-732.
78. **Voinov, O. V.** 1976. Hydrodynamics of Wetting. *Fluid Dynamics* **11**:714-721.
79. **Wachters, L. H., and N. A. J. Westerling.** 1966. The Heat Transfer from a Hot Wall to Impinging Water Drops in the Spherical State. *Chem. Eng. Sci.* **21**:1047-1056.
80. **Waldvogel, J. M., G. Diversiev, D. Poulikakos, C. M. Megaridis, D. Attinger, B. Xiong, and D. B. Wallace.** 1998. Impact and Solidification of Molten-Metal Droplets on Electronic Substrates. *Journal of Heat Transfer* **120**:539.
81. **Waldvogel, J. M., and D. Poulikakos.** 1997. Solidification Phenomena in Picoliter Size Solder Droplet Deposition on a Composite Substrate. *International Journal of Heat and Mass transfer* **40**(2):295-309.
82. **Wang, G. X., and E. F. Matthys.** 1996. Experimental Investigation of Interfacial Thermal Conductance for Molten Metal Solidification on a Substrate. *Journal of Heat Transfer* **118**:157-163.
83. **Wang, G. X., and E. F. Matthys.** 1991. Modeling of Heat Transfer and Solidification during Splat Cooling: Effect of Splat Thickness and Splat/Substrate Thermal Contact. *Int. J. Rapid Solidification* **6**:141-174.
84. **Wang, S.-P., G.-X. Wang, and E. F. Matthys.** 1998. Melting and Resolidification of a Substrate in Contact with a Molten Metal: Operational Maps. *International Journal of Heat and Mass transfer* **41**(10):1177-1188.
85. **Worthington, A. M.** 1877a. On the Forms Assumed by Drops of Liquids Falling Vertically on a Horizontal Plate. *Proc. Roy. Soc. London* **25**:261-271.
86. **Worthington, A. M.** 1877b. A Second Paper on the Forms Assumed by Drops of Liquids Falling Vertically on a Horizontal Plate. *Proc. Roy. Soc. London* **25**:498-503.
87. **Xiong, B., C. M. Megaridis, D. Poulikakos, and H. Hoang.** 1998. An Investigation of Key Factors Affecting Solder Microdroplet Deposition. *Journal of Heat Transfer* **120**(1):259-270.
88. **Yarin, A. L., and D. A. Weiss.** 1995. Impact of Drops on Solid Surfaces: Self-Similar Capillary Waves, and Splashing as a New Type of Kinematic Discontinuity. *J. Fluid Mech.* **283**:141-173.
89. **Zarzalejo, L. J., K. S. Schmaltz, and C. H. Amon.** 1999. Molten Droplet Solidification and Substrate Remelting in Microcasting. Part I: Numerical Modeling and Experimental Verification. *Heat and Mass Transfer* **34**:477-485.

90. **Zhang, X., and O. A. Basaran.** 1997. Dynamic Surface Tension Effects in Impact of a Drop with a Solid Surface. *J. Coll. Inter. Sci.* **187**:166-178.
91. **Zhao, Z., D. Poulikakos, and J. Fukai.** 1996a. Heat Transfer and Fluid Dynamics during the Collision of a Liquid Droplet on a Substrate: I-Modeling. *International Journal Heat Mass transfer* **39**:2771-2789.
92. **Zhao, Z., D. Poulikakos, and J. Fukai.** 1996b. Heat Transfer and Fluid Dynamics during the Collision of a Liquid Droplet on a Substrate: II-Experiments. *International Journal Heat Mass Transfer* **39**:2791-2802.

Appendix A: Analytical Estimation of the Maximum Spreading Diameter during Impact of a Drop on a Colder Surface Including Thermocapillary and Gravitational Effects⁴

A.1. Review of the Literature

Several novel technologies, for example spray casting (Orme 1993) or picoliter size solder droplet dispensing (Hayes and Wallace 1998), rely on an accurate prediction of the final shape of the deposited droplet. Analytical treatments have been reported that estimate the extension and duration of the spreading (Bennett and Poulikakos 1993, Pasandideh-Fard, et al. 1998, Pasandideh-Fard, et al. 1996, Schiaffino and Sonin 1997a), oscillations (Schiaffino and Sonin 1997a) and possible solidification (Madejski 1976, Pasandideh-Fard, et al. 1998, Schiaffino and Sonin 1997a) of a droplet impinging on a colder surface. The maximum spread factor β_{\max} (defined as the ratio of the maximum diameter d_{\max} of the wetted substrate area over the initial droplet diameter d_0) can be used as a first approximation of the final droplet shape (Jones 1971, Madejski 1976). A common starting point of the analytical models for β_{\max} is to balance the initial energy and the energy at the maximum spreading point, accounting for energy dissipated during the transient stages (Bennett and Poulikakos 1993, Pasandideh-Fard, et al. 1996). The main goal of this study is to derive an analytical model for estimating β_{\max} that considers the influence of a temperature-dependent surface tension and gravity.

The influence of surface tension and its dependence on temperature can be explained by considering capillary forces at the interface between the fluid and its surroundings. Forces due to surface tension act in the normal direction to the interface. They cause the drop shape to tend towards sphericity. Stresses due to a surface tension gradient, however, act parallel to the interface, and induce a fluid flow along the interface, from low to high surface tension domains (Schwabe, et al. 1982). This flow is called Marangoni convection (Boer 1996). Such a surface tension gradient can be caused by a temperature gradient, a concentration gradient, or an electrical potential (Boer 1996). In the case of a droplet impinging on a colder surface, a temperature gradient arises along the droplet surface, initiating a surface tension gradient. We do not expect to handle analytically the complex flow and related dissipation induced by Marangoni convection. Our analytical model revisits the energy balance during droplet impact to account for thermocapillary effects on the surface energy.

⁴ Most of the material of this chapter has been published in the following Conference:

Attinger, D., Z. Zhao, and D. Poulikakos. 1999. Analytical Estimation of the Maximum Spreading Diameter during Impact of a Drop on a Colder Surface Including Thermocapillary and Gravitational Effects, CD-Rom without pagination, ILASS 1999 Conference, Spray Impact on Wall and Films.

Since the influence of gravity on the spreading has been neglected in many published analyses (Bennett and Poulikakos 1993, Madejski 1976, Pasandideh-Fard, et al. 1998, Pasandideh-Fard, et al. 1996, Schiaffino and Sonin 1997a), the influence of gravity has also been considered. Both thermocapillary and gravity effects on β_{\max} are addressed quantitatively via operating maps in the Reynolds-Weber plane.

A.2. Analytical Model

A simple analytical model is developed to predict the maximum spreading diameter of a droplet during impact and cooling on a flat surface. This model includes thermocapillary and gravity effects represented by the Marangoni and Froude numbers, respectively. Criteria are given for comparing capillary, gravity, viscous and inertia effects. The model derived here extends the one developed by Pasandideh-Fard et al. (1996).

The first step in the model is to balance the energy before impact (the sum of the kinetic energy E_{K0} , potential energy E_{P0} and surface energy E_{S0}) with the sum of the viscous dissipation during spreading E_{ζ} plus the potential and surface energy (E_{P1} and E_{S1} respectively) when the droplet is at its maximum extension diameter D_{\max} :

$$E_{K0} + E_{P0} + E_{S0} = E_{\zeta} + E_{P_{\max}} + E_{S_{\max}} \quad (53)$$

Figure 39 shows the droplet conditions corresponding to the state before impact (0) and at the maximum extension of the spreading (max). It is assumed that the splat shape at its maximum extension is a cylinder of height h_t and diameter d_{\max} (Pasandideh-Fard, et al. 1996). The temperature distribution in the cylindrical splat is assumed to be independent of the vertical position and to decrease linearly in the radial direction from the center (still at the pre-impact temperature T_0) to the edge of the cylinder (at $T_0 - \Delta T$). This radial decrease of the temperature (although not necessarily linear) is supported by numerical simulations from Zhao et al. (1996a).

Before impact, we can express E_{K0} , E_{P0} and E_{S0} as follows:

$$E_{K0} = \left(\frac{1}{2} \rho v_0^2 \right) \cdot \left(\frac{\pi d_0^3}{6} \right) \quad (54)$$

$$E_{P0} = \left(\frac{1}{2} \rho d_0 g \right) \cdot \left(\frac{\pi d_0^3}{6} \right) \quad (55)$$

$$E_{S0} = \pi d_0^2 \sigma_{LG} \quad (56)$$

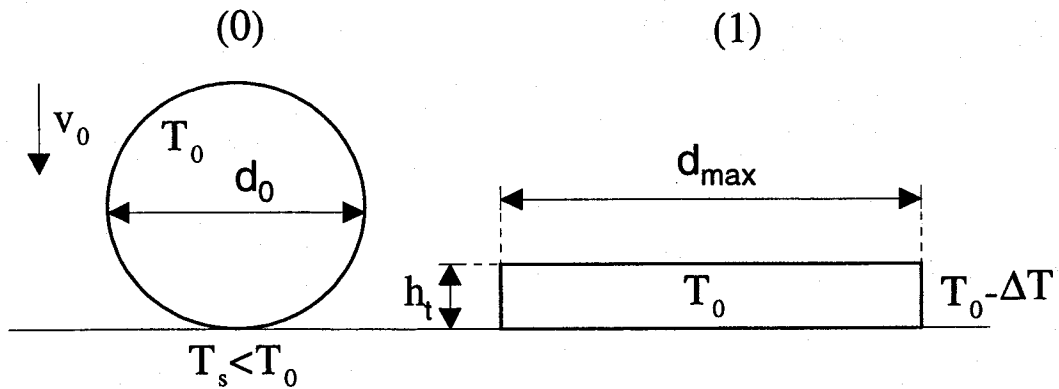


Figure 39. Droplet spreading on a flat and colder surface. It is assumed that the droplet is spherical before impact (0) and cylindrical at the maximum spreading extension (max).

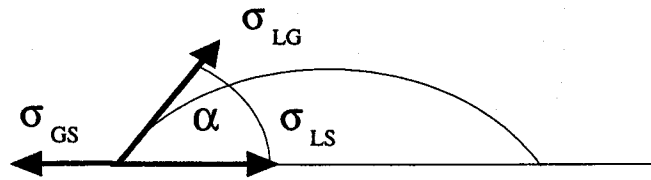


Figure 40: A liquid drop on a solid. Surface tensions at the three-phase line and wetting angle.

At the time of maximum extension diameter, the surface energy $E_{S_{\max}}$ can be calculated as follows. We first assume that surface tension depends linearly on temperature:

$$\sigma_{LG}(T) = \sigma_{LG}(T_0) + a(T - T_0) \quad (57)$$

The subscripts L and G stand for liquid and gas, respectively. The symbol a is the theoretical temperature coefficient of surface tension, and takes values in the range $[-0.47; -0.06]$ for various liquid metals (Iida and Guthrie 1988). If we neglect the gas-solid surface tension σ_{GS} in Young's equation at the wetting line (cf. Figure 40), we obtain a relation between the liquid-gas surface tension σ_{LG} and the liquid-solid surface tension σ_{LS} :

$$\sigma_{LS} = -\sigma_{LG} \cos \alpha_a \quad (58)$$

Like Pasandideh-Fard et al. (1996), we use in the above equation the advancing wetting angle α_A (in the early stages of the spreading), instead of the equilibrium wetting angle. To facilitate the analysis, we neglect the surface energy contribution on

the lateral surface of the cylinder. We obtain then by integration of the surface energy on the top and bottom of the cylinder:

$$E_{S, \max} = \frac{\pi d_{\max}^2}{4} \left(\sigma_{LG} - \frac{2}{3} a \Delta T \right) (1 - \cos \alpha_a) \quad (59)$$

We obtain the potential energy $E_{p, \max}$ by expressing the cylinder height as $h_i = \frac{2d_0^3}{3d_{\max}^2}$, according to (Pasandideh-Fard, et al. 1996):

$$E_{P, \max} = \rho g \frac{\pi d_0^6}{18 d_{\max}^2} \quad (60)$$

The work E_ζ performed in deforming the droplet against viscosity is calculated using a viscous dissipation function Φ in the boundary layer zone Ω (Chandra and Avedisian 1991):

$$E_\zeta = \int_0^{t_{spr}} \int_{\Omega} \Phi d\Omega dt \approx \Phi \Omega t_{spr} \quad (61)$$

The dissipation function and the volume Ω of the boundary layer can be approximated by (Chandra and Avedisian 1991)

$$\Phi = \mu \left[\frac{\partial u}{\partial y} + \frac{\partial v}{\partial x} \right] \frac{\partial u}{\partial y} \approx \mu \left[\frac{v_0}{\delta} \right]^2 \quad (62)$$

$$\Omega = \delta \pi \frac{d_{\max}^2}{4} \quad (63)$$

Assuming $t_{spr} = \frac{8d_0}{3v_0}$ (Pasandideh-Fard, et al. 1996), we finally obtain an estimate for the energy lost by viscous dissipation

$$E_\zeta = \pi \rho v_0^2 d_0 d_{\max}^2 \frac{\zeta}{\sqrt{Re}} \quad (64)$$

where the dissipation factor ζ depends on the assumed value for the boundary layer thickness δ . We assume here δ to be the displacement thickness of the boundary layer on a flat plate, according to the Blasius solution for a flow over a flat plate (Batchelor 1967), at a distance $d_0/2$ ($\delta = 1.22 \frac{d_0}{\sqrt{Re}}$), and obtain $\zeta = 0.547$. Pasan-

dideh-Fard et al. (1996), applying a similarity method for boundary layer on a potential axisymmetric stagnation flow, obtained $\zeta = 1/3$.

Introducing the values of E_{K0} , E_{p0} , E_{S0} , E_{ζ} , E_{Pmax} and E_{Smax} obtained above in the energy balance of Eq. (53) yields the following expression, with nondimensional numbers as defined in the nomenclature:

$$\frac{1}{12} \left(1 + \frac{1}{Fr} \right) + \frac{1}{We} = \frac{1}{\beta_{max}^2} \left(\frac{1}{18Fr} \right) + \beta_{max}^2 (1 - \cos \alpha_a) \left(\frac{1}{4We} + \frac{Ma}{6Re} \right) + \beta_{max}^2 \frac{\zeta}{\sqrt{Re}} \quad (65)$$

The above expression is a quadratic equation for β_{max}^2 .

A.3. Results

Figure 41 shows the values of the maximum spread factor β_{max} in the Re-We plane obtained from Eq. (65), first for increasing values of the Marangoni number, then for decreasing values of the Froude number. For comparison, a solution of Eq. (65) without any thermocapillarity or gravity considerations (dotted line) is plotted. This solution corresponds to the modeling of Pasandideh-Fard et al. (1996), with the only difference that $\zeta = 0.547$ was used in Figure 41, instead of $\zeta = 1/3$. We have not shown values of β_{max} smaller than 1.1, because the validity of the model is questionable for such small spreading values. The value of the advancing wetting angle is 135° . Values of β_{max} for Weber smaller than 1 have not been considered, because our treatment neglects the effect of the uncompensated Young force at the wetting line, which is the dominant spreading force at low Weber numbers (Schiaffino and Sonin 1997a). For the cases where Ma is zero, there are sometimes two solutions, mostly the first with $\beta_{max} > 1$, and the second with $\beta_{max} < 1$. The second has been eliminated, because it does not correspond to a spreading process. For the cases where gravity is negligible ($Fr = 10^5$), there is always one single solution to Eq. (65).

As shown in Figure 41, thermocapillarity and gravity affect in opposite ways the spread factor. An increasing influence of gravity (decreasing Fr) will increase β_{max} . On the other hand, increasing thermocapillarity (increasing Ma) will reduce β_{max} . The former trend can be explained by considering that spreading is a motion of the drop gravity center in direction of the gravity field, thus aided by gravity. The latter trend is due to the fact that cooling increases the value of surface tension. In order to counterbalance the effect of a larger surface tension value in the splat energy, the drop surface and corresponding spread factor are reduced. It is also expected that Marangoni convection will increase the viscous dissipation and further reduce the spread factor, but this needs to be quantified numerically.

Criteria for discriminating the importance of either thermocapillarity or gravity are provided hereafter.

First, the analysis of the importance of thermocapillarity is facilitated by re-writing Eq. (65) for the case where gravity effects play no role. This yields

$$\beta_{\max} = \sqrt{\frac{We+12}{(1-\cos\alpha_a)\left(3+\frac{2MaWe}{Re}\right)+\frac{12\zeta We}{\sqrt{Re}}}} \quad (66)$$

Note that by setting $Ma=0$, and $\zeta=1/3$, the above equation is reduced to the expression of Pasandideh-Fard et al. (1996). The major difference between eqn (14) and the one in (Pasandideh-Fard, et al. 1996) is the appearance of a term $+\frac{2MaWe}{Re}$ in the denominator, which causes a decrease of the spread factor. A comparison between the three terms in the denominator of Eq. (66) yields that we can neglect effects due to the variation of the surface tension if at least one of the two following criteria is respected:

$$Ma \ll \frac{3Re}{2We} \quad (67)$$

or

$$Ma \ll \frac{6\zeta\sqrt{Re}}{(1-\cos\alpha_a)} \quad (68)$$

Second, the relative importance of gravity can be evaluated as follows. The potential energy plays a role in the energy before impact and at the maximum extension of the splat. Since it is expected that spreading will reduce the height of the gravity center of the droplet, the relative importance of gravity in the energy before impact is larger than at the maximum splat extension. Therefore an evaluation of the relative importance of gravity before impact (LHS of Eq. (65)) gives criteria for neglecting the gravity forces: if the potential energy is negligible in the energy before impact, then gravity is negligible for the rest of the spreading. We can therefore neglect the effects due to gravity if at least one of the two following criteria is respected:

$$Fr \gg 1 \quad (69)$$

or

$$Fr \gg We/12 \quad (70)$$

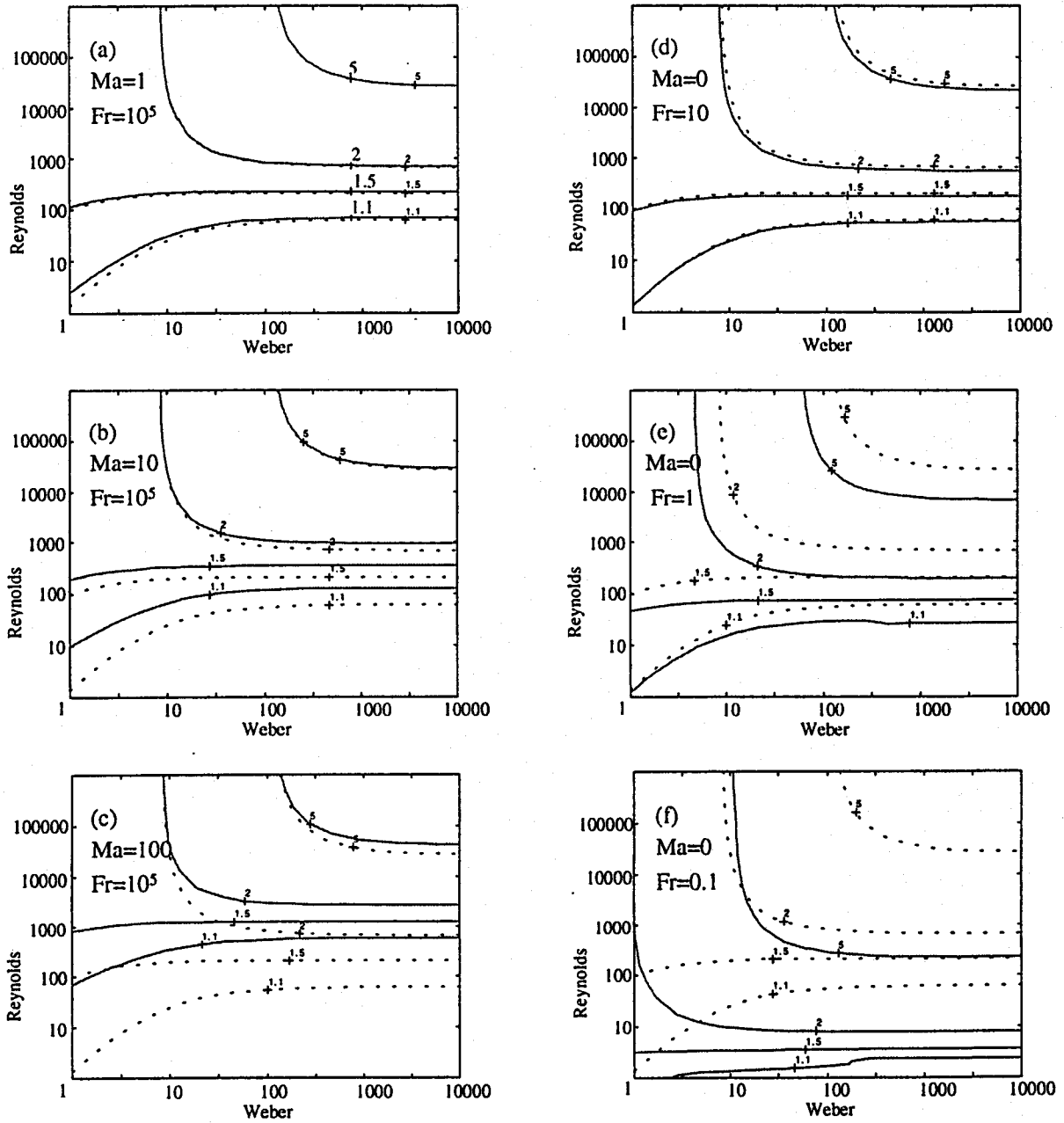


Figure 41: Maximum spread factor in the Re - We plane, with (solid) and without (dotted) consideration of thermocapillary or gravity effects. Calculations are based on Eq. (65) with $\zeta=0.547$ and $\alpha_a=135^\circ$. Plots (a-c) show the effect of an increasing Marangoni number, plots (d-f) show the effect of a decreasing Froude number

Curriculum Vitae of Daniel Attinger

Personal Data

Birth December 11th, 1971, Lausanne, Switzerland
 Citizenship Swiss

Education

1997-2000 Doctoral candidate, Department of Mechanical Engineering, ETH Zurich (Switzerland). Advisor: Prof. D. Poulikakos, Laboratory for Thermodynamics in Emerging Technologies.
 1991 – 1997 Mechanical Engineering studies at EPFL, Lausanne (Switzerland), with emphasis on fluid dynamics and thermal sciences.
 1994 – 1995 Sabbatical at the 'Faculté de Philosophie', Sorbonne University Paris, France.
 1991 Baccalaureate at the College of St-Maurice, Switzerland

Industrial Experience

Sep 1995- Oct 1995 Feasibility study of a solar driven water supply plant, EPS, Zurich, Switzerland
 Jun 1995-Sep 1995 Elaboration of an EXCEL-based database system at Elektrowatt, Zurich, Switzerland
 Jun 1994- Aug 1994 Verification of a cooling concept for a combustion chamber, ABB, Baden, Switzerland

Additional Experience

1999-2000 Supervisor for two Semester projects and for one Diploma project (equivalent to an MS Thesis) at ETH Zurich.
 1999 and 2000 Preparation of two research proposals to the Swiss National Science Foundation.
 1998-1999 Assistant for Basic Thermodynamics and Heat Transfer recitation sessions during two semesters at ETH Zurich.

Publications

1999-2000 Co-author of five peer-reviewed journal publications (one submitted, two in press, two published) and three peer-reviewed conference publications. See bibliography and footnotes of chapter 2, 3 and 4 for detailed listing.

Honors and Activities

1999-2000 President of the academic staff association (AVETH) of ETH Zurich
 1997 Ranked first among 40 candidates for the Diploma in Mechanical Engineering